To the Graduate Council:

I am submitting herewith a thesis written by Matthew Byron Haston entitled "Shear Strength Testing and Fractal Analysis of Rock Discontinuities." I have examined the final copy of this thesis for form and content and recommend that it be accepted in partial fulfillment of the requirements for the degree of Master of Science, with a major in Civil Engineering.

Matthew Mauldon, Major Professor

We have read this thesis
and recommend its acceptance:

Eric C. Drumm

Don W. Byerly

Accepted for the Council:

Associate Vice Chancellor and
Dean of the Graduate School

SHEAR STRENGTH TESTING AND FRACTAL ANALYSIS OF ROCK DISCONTINUITIES

A Thesis
Presented for the
Master of Science
Degree
The University of Tennessee, Knoxville

Matthew Byron Haston
December 1996

ACKNOWLEDGEMENTS

I would like to thank Jim Sheahan at HDR Engineering, Pittsburgh, Pennsylvania for choosing to have the discontinuities from the Foothills Parkway Project tested in our laboratories. Also, Russ Kanith at HDR, for missing a day of work to show me around the Foothills Parkway site. I would also like to thank Mark McKeown at the U.S. Bureau of Reclamation in Denver, Colorado. Mark McKeown donated the digital roughness gage mentioned herein, which made this research possible. I would like to thank my major professor, Dr. Matthew Mauldon, for his support and guidance over the past two years. I also wish to thank Dr. Eric Drumm and Dr. Don Byerly for serving on my thesis committee and for their assistance.

ABSTRACT

The shear strength of rock joints is an important concept in civil engineering and in the geosciences. Shear strength of rock joints is developed by the sliding of two planes of a rock mass over one another. The peak shear strength for any given normal stress has been shown to be related to the base friction angle, the unconfined compressive strength, and the magnitude of roughness of a rock discontinuity.

To help reduce the costs associated with testing, models have been developed to predict the peak shear strength of rock joints. Some of these models have been accepted for use by the International Society for Rock Mechanics for use by practicing engineers. While the models have been used successfully, questions have arisen over the procedure for estimating rock joint roughness. The procedure which has been used to estimate rock joint roughness required the visual matching of standard roughness profiles with those for which shear strength is to be determined.

The relatively new science of fractal geometry has been used to quantify rock joint roughness. The research in this area has been primarily conducted along purely academic lines merely for the purpose of classifying variations of roughness. In this study an attempt was made to correlate various fractal parameters to rock joint shear strength. Several fractal methods were used to analyze roughness profiles for rock joints taken from the Foothills Parkway project and the US Highway 19E project, both located in Eastern Tennessee. Included in these fractal methods was a new procedure termed the Window Average Microangle method (*WAM*) developed for this study. All fractal methods were then verified

using computer generated fractional Brownian motion profiles.

A series of laboratory tests have been performed so that Joint Roughness Coefficients could be determined for the rock discontinuities. These tests included, shear tests, point load tests, and base friction angle tests. Two fractal parameters, the normalized fractal dimension, D_n and the normalized fractal intercept, b_n were then correlated with the Joint Roughness Coefficients.

The results of this study showed the normalized fractal intercepts, b_n obtained from the variogram and *WAM* methods were positively correlated with the Joint Roughness Coefficients from laboratory tested samples and the standard profiles. Equations relating the variogram intercepts to the Joint Roughness Coefficients were developed which showed a logarithmic trend. The equations relating *WAM* intercepts and Joint Roughness Coefficients were of linear form. These equations can be used to quantify the JRC value used in the prediction of peak shear strength. The equations and procedures developed within are thought to provide a foundation for further study.

TABLE OF CONTENTS

LIST OF TABLES

LIST OF FIGURES

LIST OF SYMBOLS

JRC	=	joint roughness coefficient
Z_2	=	*Z* squared parameter
Z_3	=	*Z* cubed parameter
SF	=	structure function
R_p	=	roughness profile index
I	=	effective roughness angle
τ	=	shear stress
σ_n	=	normal stress
ϕ_b	=	base friction angle
c	=	apparent cohesion
R	=	resultant of shear and normal forces
S	=	shear force
N	=	normal force
d_n	=	peak dilation angle
S_n	=	angular expression of the failure of intact asperities
σ_c	=	unconfined compressive strength
JCS	=	joint compressive strength
L	=	length
y	=	divider separation distance
N	=	number of divider steps

D	=	fractal dimension
J	=	number of divider step sizes
x	=	horizontal coordinate
z	=	vertical coordinate
n_w	=	number of windows
m_i	=	number of point within a window
z_j	=	residual for each point
w_i	=	ith window
β	=	slope of power law fractal plot
h	=	window width
RMS	=	root mean square fractal method
$\gamma(h)$	=	one-dimensional variogram function
WAM	=	window average microangle method
H	=	Hurst exponent
ψ	=	dip of discontinuity
A'	=	area of shear plane
d	=	diameter of rock core
σ_{nf}	=	normal piston fluid pressure
$I_{S(50)}$	=	point load index
P	=	gage pressure at failure
D_e^2	=	equivalent core diameter
I_S	=	uncorrected point load index

F	=	size correction factor
D_n	=	normalized fractal dimension
D_j	=	fractal dimension of the jth profile
L_j	=	length of the jth profile
b_{nlog}	=	normalized log fractal intercept
b_{jlog}	=	log fractal intercept of the jth profile
b_n	=	normalized fractal intercept
α	=	mean roughness angle
Δz	=	elevation difference for variogram method
θ	=	intermediate profile angle for *WAM* method
ψ	=	angle of dip

CHAPTER 1: BACKGROUND AND PURPOSE

The shear strength of rock joints plays a key role in the field of civil engineering. Civil engineers are faced with problems related to shear strength when dealing with slopes, mines, dams, structures, and many other works. Early work dealing with the prediction of shear strength came mainly from Patton (1966) and Barton (1973). These researchers' contributions were combined in the development of the first empirical peak shear strength criterion.

The peak shear strength of a rock joint is closely related to the surface roughness of the discontinuity. The first peak shear strength criterion developed by Barton used a term called the Joint Roughness Coefficient (JRC) to express the roughness of the joint. JRCs were to be estimated by visually matching a set of standard profiles with the joint in question. In recent times however, the subjective nature of visually estimating Joint Roughness Coefficients has been questioned (Miller et al., 1989, Hsiung et al., 1990, Wakabayashi and Fukushige, 1992). Many researchers have turned to various statistical methods to quantify the roughness characteristics of rock discontinuities.

One of the first attempts to statistically evaluate joint surface roughness resulted in the parameter Z_2 (Tse and Cruden, 1979). Z_2 was a parameter developed to express the Root Mean Square (RMS) of the first derivative of the surface profile. Other parameters have also been developed to characterize roughness profiles for rock joints. Among these were: Z_3, the RMS of the second derivative (Dight and Chiu, 1981); structure function (SF) (Maerz et. al, 1990); centerline average value, root mean square value (Wu and Ali, 1978); and the roughness profile index (R_p) (Reeves, 1990).

Among these parameters, the Z_2 has proven to be the most widely accepted. McWilliams *et al.* (1993) found Z_2 was closely correlated to a sliding roughness scale such as the JRC scale. Tse and Cruden (1979) also found correlations between Z_2 and the JRC scale. While many researchers have found correlations between Z_2 and the JRC, no firm evidence has been presented which has convinced the International Society for Rock Mechanics to adopt the Z_2 or any other geostatistical measure over the JRC coefficient.

In this study, the relatively new discipline of fractal geometry is used in an effort to quantify the roughness of natural rock joints. The use of fractal geometry to describe the surface roughness of a rock joint is not a new idea. However, only one study has been undertaken to correlate the JRC value as calculated from shear tests with any fractal parameters (Hsiung et al., 1993). In the 1993 study, the self-similar methods used to calculate the fractal dimensions were not appropriate for the self-affine joint profiles. Also, the intercept of the fractal power law plot was ignored.

Here a rational method was developed to quantify JRC values. The method involved quantifying all other parameters in Barton's peak shear strength criterion and solving for the JRC value. The method is demonstrated for rock joint samples obtained from the Foothills Parkway project and the US Highway 19E project. The JRC values obtained from the laboratory analysis will then be correlated with both the intercept and slope of the fractal power law plot. The fractal methods used in the study will be validated using the theory of fractional Brownian motion.

CHAPTER 2: PEAK SHEAR STRENGTH MODEL

Introduction

The most widely accepted criterion for the shear strength of rock joints was developed by Barton and Choubey (1977). The model was later accepted for use by the International Society for Rock Mechanics. In Barton's model the base friction angle of the rock, unconfined compressive strength, joint roughness parameter (JRC), and the level of normal stress at which the shear test was conducted were used to predict shear strength.

Peak Shear Strength Model

The first part of the development of the model was to understand the components that affect shear strength, and how they interact. The first revelation concerning the behavior of non-planar joints came from Patton (1966), who showed the dilatant behavior of rock joints by using the model shown in figure 1. The joint surface is idealized as a perfectly matched series of saw teeth. When the joint in figure 1 is subjected to normal and shear loadings as

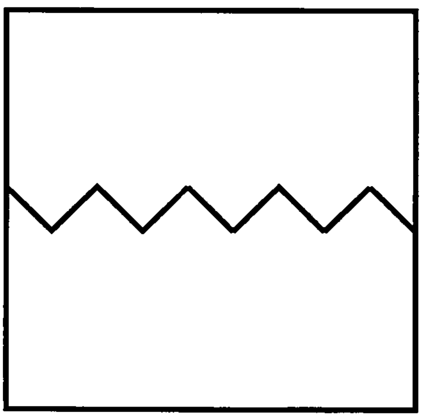

Figure 1- Patton's basic model.

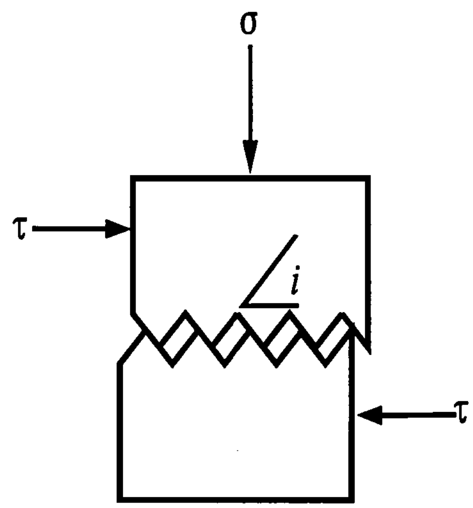

Figure 2 Dilation due to overriding.

shown in figure 2, several things happen. At low levels of normal stress the asperities must be overridden, resulting in dilation. Dilation is an increase in volume of the specimen due to the overriding of asperities. This involves frictional sliding along the asperity surfaces also shown in figure 2. The sliding does not occur in the plane of the applied shear stress but occurs in a plane at an angle *i* to the shear plane. Therefore, the shear and normal stresses acting on the specimen must be resolved with respect to the angle *i.* After this has been accomplished, we are left with the expression for frictional sliding along rock discontinuities at low levels of normal stress (Patton, 1966).

$$\tau = \sigma_n(\phi_b + i) \tag{1}$$

Equation (1) shows that the shear strength along a joint is a function of the applied normal stress (σ_n), the base friction angle of the material on which sliding occurs (ϕ_b), and the effective roughness angle (i). With increasing normal stress, dilation is inhibited. At a sufficiently large value of normal stress, asperities must be sheared in order for shear displacement to occur. For this condition it is assumed that the Coulomb relationship (eqn. (2)) is valid, where c is an apparent cohesion generated by the shearing of asperities.

$$\tau = c + \sigma_n (\tan \phi_b) \qquad \textbf{(2)}$$

The two models presented above are only valid at the extremes of low and high normal stresses since the transition between overriding and shearing is not clear. Furthermore, it would be impossible to predict shear strength with Patton's model since the i value and the c value are not quantifiable without conducting shear tests. There is however a simple relationship that can be derived from these models.

Figure 3a shows a simplified version of a shear test on a planar joint that can be dealt with using Patton's model. Note that the discontinuity is inclined at an angle i to the horizontal. Sliding occurs just when the resultant, **R** is inclined at an angle of ϕ_b plus i from the vertical. Thus the ratio of the shear force to the normal force is

$$\left(\frac{S}{N}\right)_f = \tan(\phi_b + i). \qquad \textbf{(3)}$$

In figure 3a the value of i could have been directly measured, but that approach would not have been practical for the highly irregular surfaces of real rock joints.

To deal with the highly complex nature of real rock joints, two new terms must first be introduced. The peak dilation angle, d_n, is the instantaneous inclination of the shearing

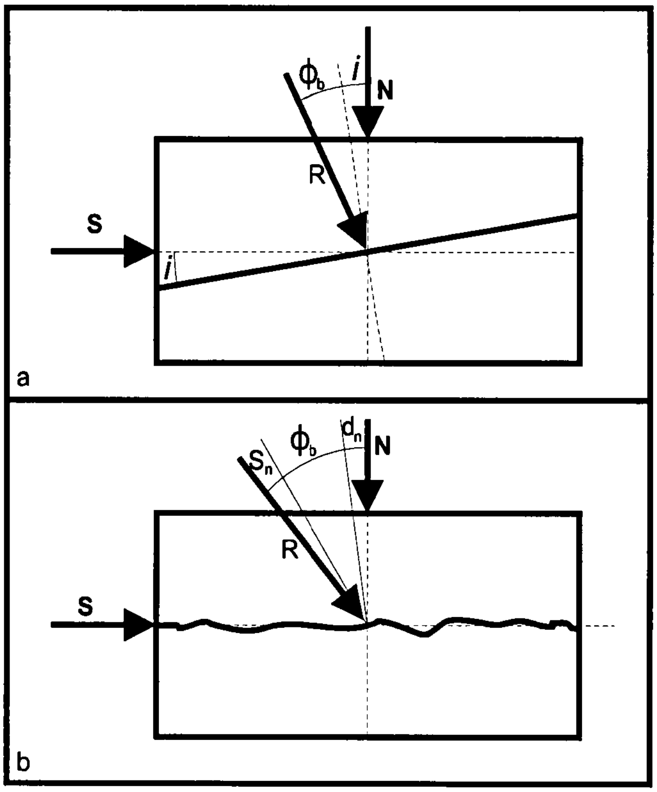

Figure 3 - Inclination of resultant due to roughness.

path at peak shear strength relative to the normal direction. This is a very important concept, since for a given normal stress the peak dilation angle represents the minimum energy path between sliding over and shearing through asperities (Barton, 1973). Another important aspect of the peak dilation angle is that it occurs just at the instant the peak shear strength has been generated. This unique value is representative of a rock joint at peak shear strength. Other researchers have also shown this through laboratory experiments (Goodman, 1989). The angle S_n represents the failure of intact asperities.

Figure 3b and equation 4 (Barton, 1973) show how the new terms, d_n and S_n, and the base friction angle combine to effect the inclination of the resultant, **R**, at limiting equilibrium. With these tools we are no longer limited to working with either low normal

$$\left(\frac{S}{N}\right)_f = \tan(\phi_b + d_n + S_n) \tag{4}$$

stresses where no shearing occurs or high normal stresses where no dilation occurs. As the normal stress level rises, the angular component of dilation (d_n) decreases while the component due to shearing, S_n, increases.

Barton realized the powerful consequences of relating the peak dilation angle to the ratio of shear to normal stress at failure and began a series of tests to correlate the two. Standard shear tests were conducted on model tension joints and data relating to peak shear stress, peak dilation angle, and levels of normal stress were collected. To represent the data, peak dilation angles were plotted versus the arc tangent of the ratio of shear to normal stress at failure (Barton, 1973). From these tests the following relationship was obtained:

$$\tau/\sigma_n = \tan(2d_n + \phi_b). \tag{5}$$

A similar result was obtained when the peak dilation angle was plotted against the ratio of normal stress to unconfined compressive strength (σ_c) of the model material. The equation generated by that correlation is

$$d_n = (10)\log_{10}(\sigma_c/\sigma_n) \tag{6}$$

(Barton, 1973). The above equation shows that at very low normal stresses there would be a great deal of dilation, while at normal stresses equal to the unconfined compressive strength, dilation would be completely suppressed. By combining the two empirical equations above, the first peak shear strength model was obtained:

$$\tau/\sigma_n = \tan[(20)\log(\sigma_c/\sigma_n) + \phi_b] \quad \textbf{(7)}$$

(Barton, 1977).

As stated earlier, the tests performed by Barton to correlate the data were conducted on model tension joints. Joints formed by tension breaks in non-foliated rocks have very rough surface profiles which are not representative of all discontinuities. In fact a range of surface roughness is exhibited when dealing with rock joints. Very smooth planar surfaces are typically found in foliation joints, while bedding joints would typically represent an intermediate range. When sheared, smoother joints would have a smaller peak dilation angle (d_n) and little shearing of asperities (S_n). The component of shearing resistance provided by rock on rock sliding ($\tan \phi_b$) would, however, remain unchanged.

In order to quantify the effects of joint roughness on shear strength, several sets of model discontinuities were tested (Barton and Choubey, 1977). The results revealed that the constant of twenty found in the original relationship (equation 7) represented the upper boundary for rough tension joints while a value of ten represented the intermediate range and a value of five modeled the behavior of planar foliation joints. The value of zero represents a perfectly planar surface and equation 7 reduces to:

$$\tau/\sigma_n = \tan(\phi_b) \quad \textbf{(8)}$$

which is for perfect rock to rock contact with no roughness-induced dilation or shearing of asperities. Tests were conducted until a range of ten coefficients matching a set of ten profiles were developed. The constant twenty in Barton's original equation was replaced by the term Joint Roughness Coefficient (JRC). The modified equation is

$$\tau/\sigma_n = \tan[(JRC)\log(\sigma_c/\sigma_n) + \phi_b] \tag{9}$$

(Barton and Choubey, 1977). Joint Roughness Coefficients are meant to be chosen by matching the standard profiles, reproduced from a copy of the original in figure 4, with the profile from the surface for which shear strength is to be estimated.

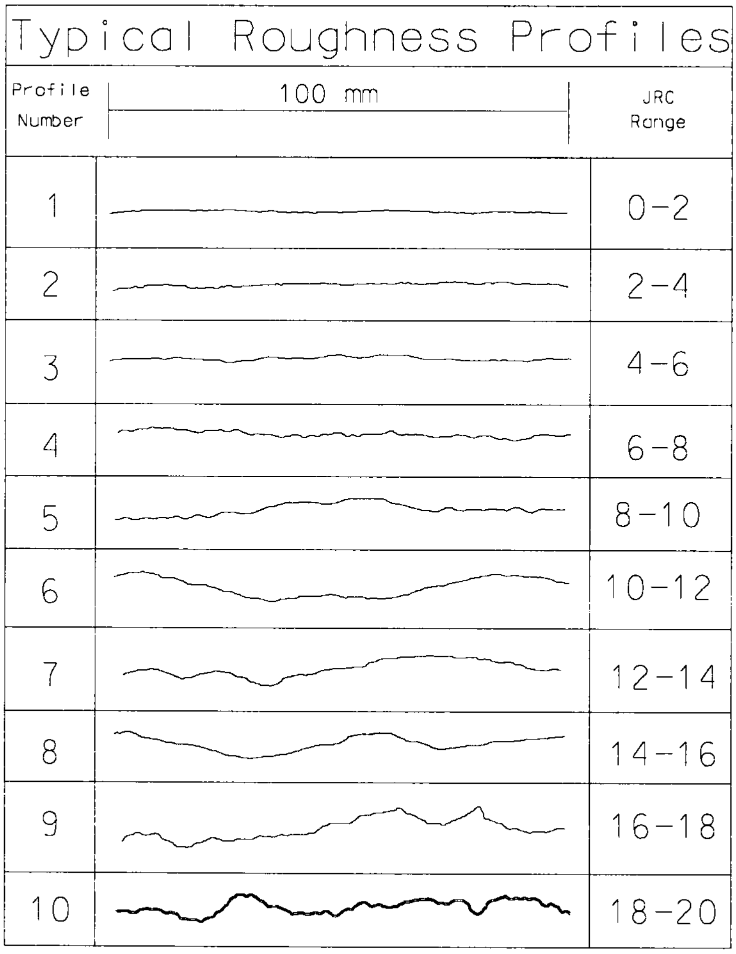

Figure 4 - Reproduction of standard roughness profiles; after Barton and Choubey (1977).

Effects of Weathering

The peak shear strength criteria developed by Barton and Choubey would apply to weathered joints as well. Shear strength for a weathered joint should be less than that for an unweathered joint with identical roughness profiles. This occurs because the unconfined compressive strength of the joint is reduced by weathering. A serious problem in quantifying the compressive strength is encountered since only the rock in the immediate vicinity of the joint is affected.

The unconfined compressive strength can be determined by several methods. Either direct unconfined compression tests, or more popularly, point load tests can be run to yield a point load strength index which is correlated with unconfined compressive strength. The problem arises when only the rock in the immediate vicinity of the joint is altered by weathering. While tests conducted on samples around the joint may provide information on the unconfined compressive strength of the unweathered rock, they are not representative of the joint. Furthermore, unless a massive coring operation is undertaken (hundreds of samples from the same joint) it would be nearly impossible to determine σ_c for the joint. No reliable method has been developed for determining the unconfined compressive strength of a weathered joint.

In light of this problem, Barton developed the term JCS or Joint Compressive Strength to replace the unconfined compressive strength term in the peak shear strength criteria (equation 9). The modified equation is

$$\tau/\sigma_n = \tan[(JRC)\log(\frac{JCS}{\sigma_n}) + \phi_b] \tag{10}$$

(Barton, 1973). For an unweathered joint the JCS is equal to the unconfined compressive strength. In weathered joints the JCS is whatever value of compressive strength deemed appropriate for the joint surface. Test were conducted by Barton to determine a ratio of JCS/σ_c that could be used in making an estimate of shear strength when no direct test data was available. The results of these tests indicate that a ratio of JCS/σ_c of 1/4 would provide a safe estimate (Barton, 1973) when no direct test data is available.

When a sufficient number of samples are available, the JCS can be evaluated with Schmidt hammer tests. The Schmidt hammer test was originally developed to test the compressive strength of concrete. The test is conducted by applying an impact loading to the material to be tested by means of a metal cylinder. The amount of rebound of the cylinder is then read from a graduated scale on the Schmidt hammer. For rock joints, the JCS has been shown to be related to the Schmidt hammer rebound number, R_e, by:

$$\log(JCS) = 0.00088\gamma(R_e) + 1.01 \tag{11}$$

where γ is the unit weight of the rock (Hsiung *et al.*, 1993).

CHAPTER 3: FRACTAL GEOMETRY

Introduction to Fractal Geometry

Euclidean geometry is the branch of mathematics that deals with the measurement and properties of points, lines, planes and volumes. Geometry also represents the arrangement of objects made up of points, lines, planes and volumes which, when combined, form a specific shape or figure. Shapes found in nature such as mountains, coastlines, river systems, clouds, trees, and an infinite number of other objects are not easily described by traditional Euclidean geometry. In his essay, *The Fractal Geometry of Nature*, Benoit Mandelbrot collected together many previously developed ideas regarding irregular natural shapes in one place and with the aid of spectacular graphics firmly entrenched the term "fractal" in the modern vocabulary (Mandelbrot, 1983).

Fractals occupy the borderline between Euclidean geometry and complete randomness. Mandelbrot's theory sheds new light into mathematical problems concerning natural objects whose shapes form functions with disturbing properties. These natural shape functions are continuous everywhere yet nowhere differentiable and of infinite length and null area. Fractals allow scientists from a wide range of fields to quantify shapes that had been described with terms such as "*in between, pimply, pocky, ramified, tortuous, wiggly, wispy, wrinkled*" (Mandelbrot, 1983). Elevation profiles of joint surfaces belong to the class of functions that had heretofore been described by terms such as those listed above.

Fractals quantify natural objects based upon their irregularity. This concept will be illustrated using the image of Great Britain shown in figure 5. The length of the coastline can

Figure 5 - Mainland Great Britain.

be approximated by using a pair of dividers. The divider endpoints are separated a distance y and walked around the coastline. The number of steps necessary to complete the walk are then recorded as N. The length of the coastline, L, can be approximated by

$$L = Ny. \quad \textbf{(12)}$$

The separation distance between the divider endpoints is then reduced and the walk repeated recording y and N. When the new values of y and N are substituted into equation 12 the total measured length of the coastline would have increased. If the separation distance between the divider endpoints is steadily decreased and allowed to converge to zero then the length of the coastline is found to increase without bound (Mandelbrot, 1983). This is not readily evident at the map scale but if the true coastline of Great Britain were measured, features such as peninsulas would be important at large divider separation distances, while boulders along the shore would play an important role as the separation distance is steadily reduced. Finally, the subatomic structure of the minerals composing the soil would become relevant at some infinitesimal separation distance.

Had the coastline in the previous example been a Euclidean shape, a square, then perimeter length would have been a constant for all separation distances, y. Since the perimeter length in the coastline example was not a constant, it could not be used for descriptive purposes. Early work by Hausdorff and Besicovitch did show, however, that a constant relationship could be developed from equation 12. They found that if the logarithms of the number of steps, N, necessary to traverse the coastline were plotted versus the logarithms of the corresponding divider separation distances, y, a constant slope was obtained. Figure 6 shows an example of such a plot where the slope is shown as D. Despite

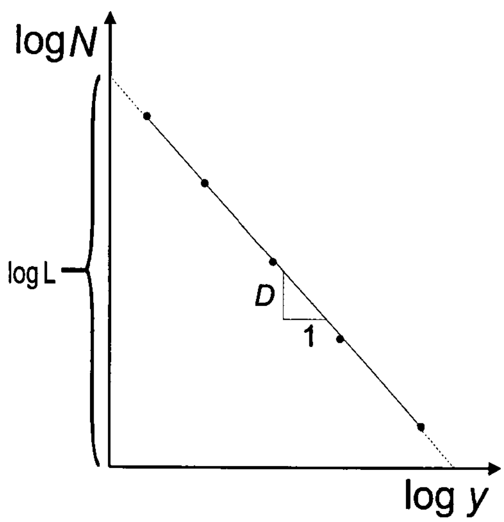

Figure 6 - Graph of log N versus log y which yields the constant slope, D, used for descriptive purposes.

the unbounded increase in L, the plot would yield a constant slope, D, which could be used for descriptive purposes. The descriptive parameter, D, became known as the Hausdorff-Besicovitch dimension (Mandelbrot, 1983).

The constant relationship between N and y developed from Hausdorff's and Besicovitch's plots is shown as equation 13,

$$N = Ly^{-D} \tag{13}$$

or

$$\log N = \log L - D \log y \tag{14}$$

where equation 14 is of the form developed from a plot such, as figure 6. To gain a clearer understanding of the effect of the Hausdorff-Besicovitch dimension, we can rearrange equation 13 as:

$$L = Ny^{D}. \tag{15}$$

For the example of a square mentioned earlier, the Hausdorff-Besicovitch dimension would equal one and equation 15 would reduce to equation 12. For any natural shape, such as the coastline of mainland Great Britain, D would range from just greater than one to two. Thus, using the value of D obtained from a plot, such as the one shown in figure 6, a more reasonable estimation of perimeter length, L, could be obtained from equation 15 than from equation 12. Any shape for which the Hausdorff-Besicovitch dimension exceeds its topological (Euclidean) dimension is a fractal. The Hausdorff-Besicovitch dimension was renamed the fractal (from the Latin *fractus* meaning to break or separate into fractions) dimension by Mandelbrot (Mandelbrot, 1983).

Self-similarity and Self-affinity

Self-similarity and self-affinity are terms related to scaling. A self-similar joint profile would be one for which an isotropically enlarged portion of the profile would appear statistically similar to the entire profile (Power and Tullis, 1991). Figure 7a shows the result of an isotropic enlargement on an artificial self-similar joint profile. Mathematically, the individual points composing the profile would be transformed according to:

$$x = (x_1, x_2 \ldots, x_n) \rightarrow r(x) = (x_1 r, x_2 r, \ldots, x_n r) \quad \textbf{(16)}$$

which transforms the set, S into r(S) in which the same statistical moments are retained (Mandelbrot 1983). Statistical moments are measures that relate the degree of similarity between two shapes. In less technical terms, the points of the profile could be transformed

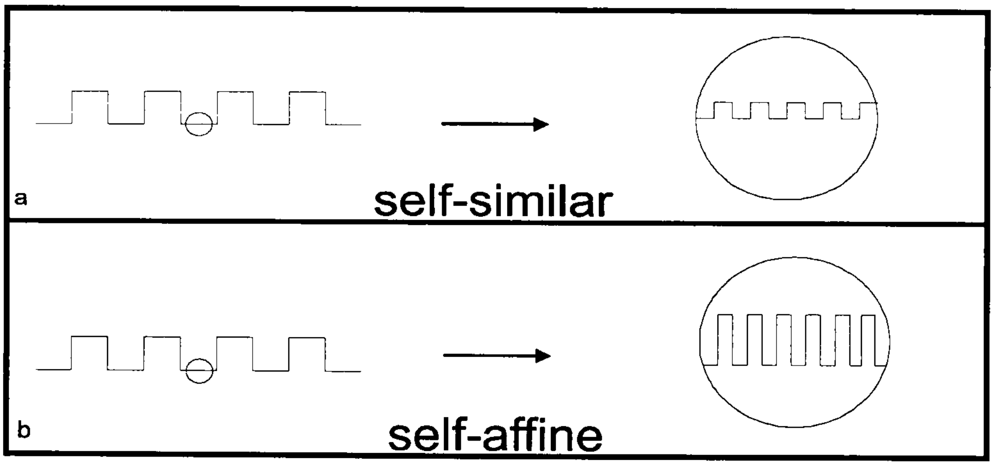

Figure 7 - Artificial self-similar and self-affine joint profiles. (a) Isotropic magnification of a self-similar profile shown within the circle; (b) isotropic magnification of a self-affine profile shown within the circle.

by the same scaling factor in all directions.

An enlarged section of a self-affine joint profile would appear statistically similar only if different magnification factors were applied in the x and z directions (Power and Tullis, 1991). Figure 7b shows the effect of an isotropic enlagrement on an artificial self-affine joint profile.The individual points composing the profile are transformed according to:

$$x = (x_1, x_2, \ldots, x_n) \rightarrow r(x) = (x_1 r_1, x_2 r_2, \ldots x_n r_n) \qquad \textbf{(17)}$$

which transforms the set S into r(S), retaining the same statistical moments. (Mandelbrot, 1983). Different scaling factors must be used in the x and z directions for a self-affine transformed section to retain the same statistical moments.

Self-similarity and self-affinity are important concepts in the calculation of the fractal dimension. The example regarding the coastline of Great Britain demonstrated the calculation of a fractal dimension using a self-similar method. The self-similar divider method could only be correctly used for a self-similar object. In the example, the object (coastline of Great Britain) was formed by a zeroset, where the zeroset was created by the sea and the island represented a section that rose above the zeroset (Russ, 1994). Since all of the elevation values are constant for a zeroset, the same scaling factor could be used in the x and y directions. Thus, the coastline of mainland Great Britain is a self-similar object and the divider method could be used correctly.

Problems are encountered when self-similar methods are used in the calculation of fractal dimensions for self-affine objects. When a method such as the divider method is used to estimate the fractal dimension of a self-affine object, all features smaller that the divider step size are lost. Only at very small divider step sizes do the statistical moments of a self-affine fractal object approximate those of the self-similar fractal. The divider size where the moments are equal is referred to as the crossover length. When divider sizes larger than the crossover length are used, the topological, rather than the fractal dimension of the object is recorded. This would result in a "fractal" dimension very close to one for a profilometer trace of a rock joint.

In the case of a profile formed by a profilometer trace of a rock discontinuity, controversy has existed over self-similarity and self-affinity. Russ (1994) has asserted that a section taken at any orientation other than parallel to the mean surface orientation would result in a self-affine object.This is related to the fact that all elevation values are constant for sections parallel to the mean surface orientation, i.e., the coastline of mainland Great Britain. Thus, a horizontal section profile could be reproduced with a constant scaling factor in both the x and y directions. The vertical section generated by a profilometer trace would not conform to the requirement because a different scaling factor would have to be applied in the vertical direction. Figure 8 shows an example of a vertical and horizontal section taken from an island. The horizontal section, taken in the x-y plane, corresponds to an elevation contour and is self-similar. Note that elevation contours define planes parallel to the mean surface orientation. The vertical section, taken in the x-z plane, is from an orientation normal to the elevation contours and is self-affine. The self-affine nature of rock joints is developed by the processes weathering and geologic deposition. These processes lead to anisotropy of the topography in the vertical direction. Other researchers have also regarded joint profiles

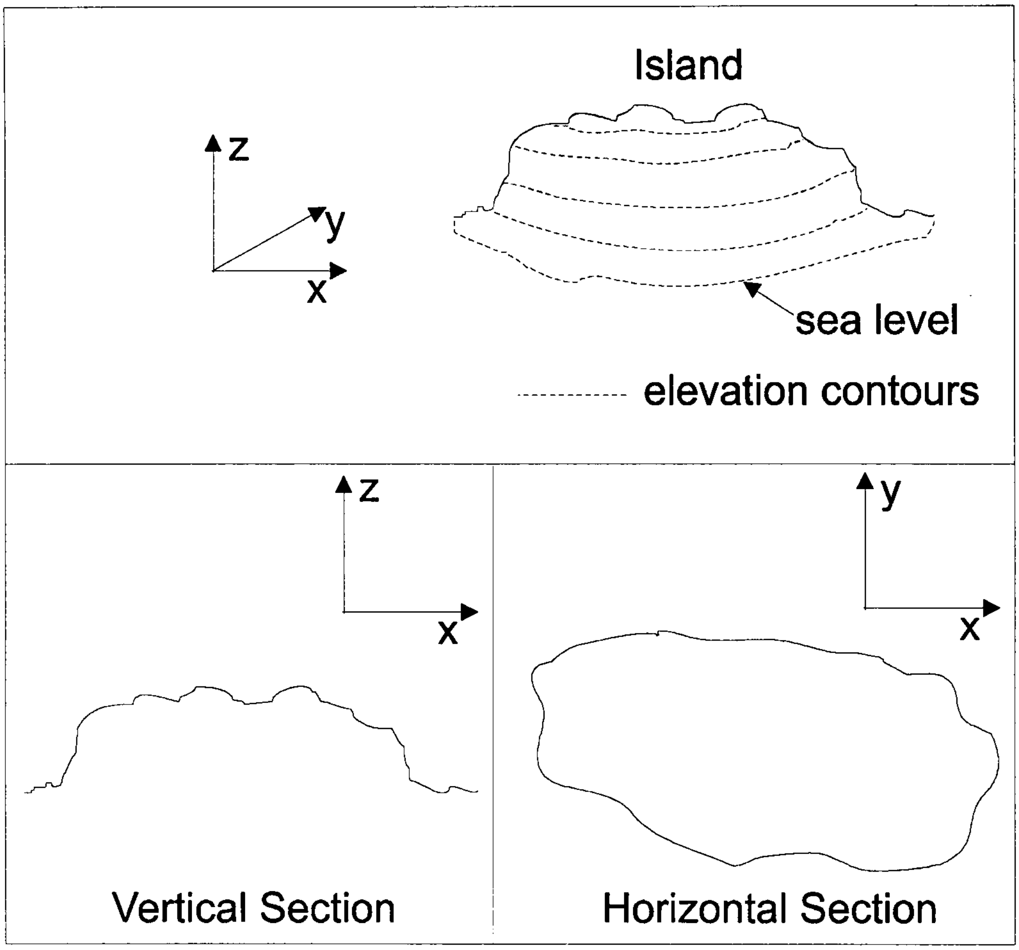

Figure 8 - Examples of vertical and horizontal sectioning. A self-affine vertical section taken normal to the mean surface orientation and a self-similar horizontal section taken parallel to the mean surface orientation from the island shown in the upper box.

as self-affine objects (Brown, 1992, Hsiung *et al.*, 1995, and Kulatilake *et al.*, 1995).

In a 1991 study, Power and Tullis used spectral analysis to investigate the application of self-similar and self-affine fractal models to profiles from discontinuities. They concluded that most natural joint surfaces were approximately self-similar (Power and Tullis, 1991). Many other researchers have used self-similar methods in the calculation of the fractal dimension (Carr and Warriner, 1989, Lee *et al.*, 1990, Wakabayashi and Fukushige, 1992).

CHAPTER 4: FRACTAL METHODS

Introduction

There are numerous methods with which the fractal dimension of a rock discontinuity could be calculated. In this section self-similar and self-affine methods will be presented. The self-similar model will be verified using a correlation with a published study. The self-affine methods will be verified using fractional Brownian motion functions of known fractal dimensions.

Modified Divider Method

The first method to be examined for calculating the fractal dimension of rock joint profiles is a self-similar method developed by James Carr (1990). The method is based upon the divider method described in the example presented earlier. A FORTRAN computer program to facilitate the calculation was received from Carr in an e-mail message (Carr, 1996). The program operates by first reading the input file which contains the number of divider step sizes (J) to be used as input line 1, the length of the individual divider steps as input line 2, and the distance and elevation points (x, z) composing the profile as the remaining input lines. The computer algorithm (shown in appendix A) then calculates the number of steps (N) necessary to transverse the profile with a set of circles of radius y as shown in figure 9. The next value of y is then used to create the circles and a new value of N is obtained. When the algorithm has computed N values for all circle diameters the results are then transferred into a linear regression subroutine which computes the fractal dimension,

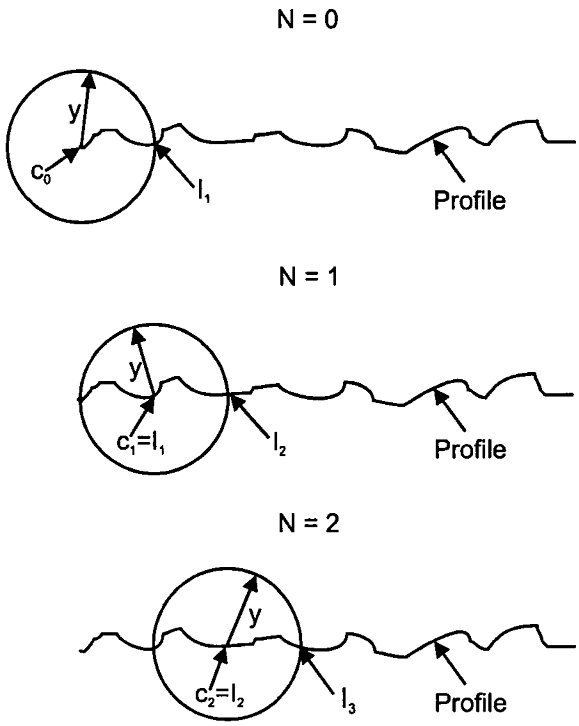

Figure 9 - Graphical illustration of the computer algorithm. In each step, the circle center (c_i) is located at I_{i-1}, the intersection of the profile with the preceding circle.

D, according to:

$$D = -\frac{\Sigma(Log_{10}(N)Log_{10}(y)) - (\Sigma Log_{10}(N)\Sigma Log_{10}(y))/J}{\Sigma(Log_{10}(y))^2 - (\Sigma Log_{10}(y))^2/J} \tag{18}$$

where J is the number of divider step sizes. The output from the program consists of the input divider lengths (y) and the number of steps (N) necessary to traverse the profile and the fractal dimension.

In order to verify the method, the reproduced set of ten standard JRC roughness profiles presented earlier in figure 4 were digitized from a scale copy of the original using Intergraph's *Microstation version 5.0.* The pairs (x, z) of coordinates were taken at intervals of 0.77 millimeters along the horizontal direction (x) of the profile with a vertical resolution of 0.10 millimeters. Each of the ten profiles was then input into the program with four divider step sizes of 0.85, 2.75, 5.65 and 8.50 millimeters. The fractal dimensions calculated were then compared to those obtained by Carr (1990), in Table 1 below. The results were then correlated using *Microsoft Excel version 7.0* and a multiple R of 0.9946 with a standard error of estimate of 0.0004 was obtained. This showed that the implementation of the method

Table 1 - Comparison of fractal dimensions for the divider method.

Roughness Profile	Fractal Dimension (Carr)	Fractal Dimension (Haston)
1	1.00060	1.00000
2	1.00120	1.00042
3	1.00229	1.00054
4	1.00312	1.00178
5	1.00382	1.00191
6	1.00469	1.00269
7	1.00560	1.00377
8	1.00620	1.00431
9	1.00965	1.00770
10	1.01245	1.00974

was correct. However, the values obtained were so close to one that it would have been impossible for them to be used in a correlation with shear strength. The low values obtained from the self-similar divider method showed that self-affine models should be pursued.

Root Mean Square Method

The next method to be examined is the Root Mean Square (RMS) versus window length method proposed by Malinverno (Russ, 1994). In this method, the standard deviation of the elevation values are calculated for a series of widths (windows) along the profile. For every window a regression is used to detrend the data points within. The differences in elevation of the data points to this line (residuals) are then calculated and used to evaluate the *RMS* value for all the windows of a particular length according to:

$$\Delta_i = \frac{1}{m_i - 2} \sum_{j \in w_i} (z_j - z)^2 \tag{19}$$

and

$$RMS(w) = \frac{1}{n_W} \sum_{i=1}^{n_w} \sqrt{\Delta_i} \tag{20}$$

where m_i is the number of points in window w_i , z_j are the residuals from the line, z is the mean residual in the *i*th window w_i, and n_w is the total number of windows of length w. The value of m_i is reduced by two to correct for the two degrees of freedom used to generate the slope and intercept of the detrending line. The value of z would be zero for a linear regression but must be considered if a simple endpoint regression where used to generate the detrending line in w_i.

For this study, a spreadsheet was developed in *Microsoft Excel version 7.0* to perform the necessary calculations. A linear regression was used to calculate the slope and intercept of the detrending line which meant the mean residuals for any window width, z, were equal to zero. The number of windows generated for each window size was large since the w_{i+1}

window begins at the $i + 1$ point along the profile. The fractal dimension is calculated for the RMS method by plotting the log RMS value obtained from equation 20 versus the log window size for a number of window sizes. The slope, β, of the resulting linear plot is related to the fractal dimension by:

$$D = 2 - \beta \tag{21}$$

where D is the fractal dimension.

Example of the *RMS* Method

To demonstrate the *RMS* method, an example has been developed using JRC profile number 10. In order to simplify the example, only three window sizes will be examined. For the first window size, the calculations within one window will be described. In actuality, several window sizes would be used for the calculation of the fractal parameters. Since the number of windows necessary to calculate the fractal parameters is large, spreadsheet templates were developed to automate the process. With the spreadsheet templates, one would simply copy the coordinates composing the profile into the correct columns of the template and the calculations would be performed automatically. The formulae used in the *RMS* spreadsheet template are shown, in spreadsheet form, as appendix C.

1. The first step in the calculation of the fractal parameters is to subdivide the profile using the first window size. For this example, JRC profile ten is subdivided by windows of 2.31 mm width as shown in figure 10. The values chosen for window widths are functions of the horizontal spacing of the data points composing the profile. JRC

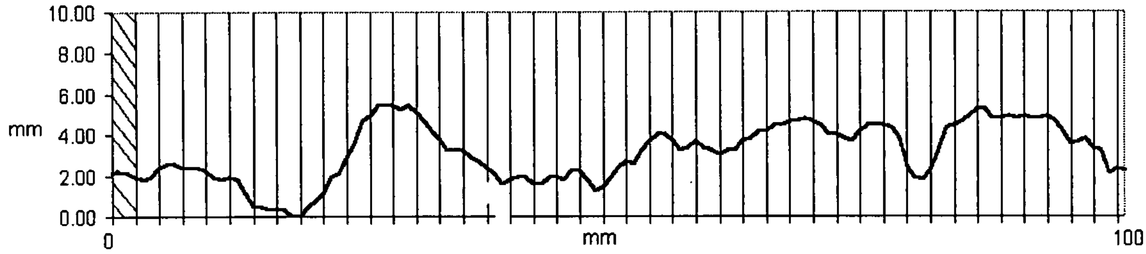

Figure 10 - JRC standard profile number ten subdivided by windows of 2.31 mm width. Note the first window, as indicated by the cross-hatching, is used for the example. This figure has a vertical exaggeration of 2:1.

profile number 10 was digitized at a horizontal resolution of 0.77 mm. Therefore, all window widths are multiples of the 0.77 mm horizontal resolution.

2. The *RMS* value is then calculated for all the windows of 2.31 mm width. For this example, the first window, denoted by the cross-hatching in figure 10, will be examined. In every window of 2.31 mm width, there are four data points; one for every digitized point on the profile. A linear regression is then performed to fit a line to the four data points composing the profile in the first window. This regression is performed in the spreadsheet using the commands: *INTERCEPT*(B3..B6, A3..A6) and *SLOPE(B3:B6, A3:A6)* in cells *C3..C6* and *D3..D6*, respectively. These commands calculate the intercept and slope of the regression line formed from the digitized *x (A3..A6)* and *z (B3..B6)* coordinates in the first window. The line resulting from this regression is shown in figure 11.

3. In order to calculate the quantity, Δ_i (eqn. 19), the residuals, z_j, of the data points to the regression line must be determined. Here, the residuals are defined as the differences in elevation, of the data points, relative to the line. These relative differences in elevation to the line are shown in figure 11. Each residual for this example, by

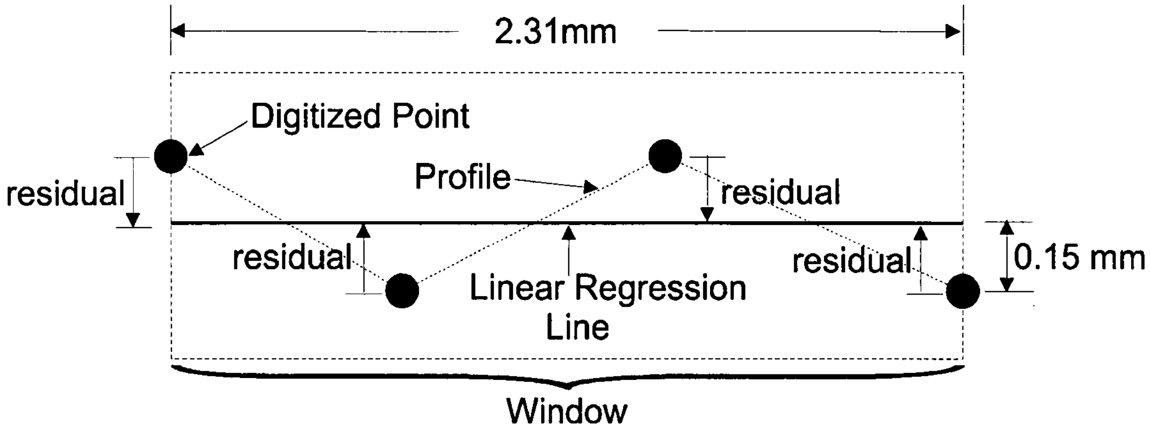

Figure 11 - Figure illustrating the calculation of residuals for one window of the *RMS* method. In the figure the residuals are measured vertically from the line formed by the linear regression of the four data points. All of the residuals in this example are equal to 0.15 mm.

coincidence, was equal to 0.15 mm. This is done in cells *M3..M6* of the spreadsheet. For example, in cell *M3*, the residual z_j, is given by *B3 - D3*A3 + C3*, where *B3* is the *z* coordinate of the point on the profile, and *D3*A3 + C3* is the *z* coordinate of the corresponding point on the regression line (cf. mx + b).

4. The next step is to determine the quantity $(z_j - z)^2$. z is the sum of the residuals in the window. Since we are using a linear regression, z, by definition, equals zero. Therefore, $(z_j - z)^2$ equals z_j^2. This step is performed by squaring the quantity, *B3 - D3*A3 + C3,* in example spreadsheet cell, *M3.*

5. The next step is to determine the quantity $m_i - 2$. m_i is the number of digitized points per window, in this case 4. Therefore, $m_i - 2$ equals 2.This step is performed manually in example spreadsheet cell, *M3*, as $((B3 - D3*A3 + C3)^2)/2$.

6. With the information from steps 3 through 5, the calculation of Δ_i for the first point of the first window is complete. The square root of the Δ_i term is then taken so the summation of the $(\Delta_i)^{0.5}$ values can be determined according to equation 20. This

step is also completed in example spreadsheet cell *M3* as *(((B3 - D3*A3 + C3)²)/2)⁰·⁵*. We are then left with the value of $(\Delta_i)^{0.5}$ for the first point of the first window in spreadsheet cell *M3*.

7. With the information from step 6, the *RMS* value for the 2.31 mm window width can then be calculated according to equation 20. The *RMS* value for the 2.31 mm window width was 0.023 mm. The sum of all $(\Delta_i)^{0.5}$ values is calculated by using the command *SUM(M3:M1029)* in spreadsheet cell *M1031*. The total number of windows, n_w, is calculated, in spreadsheet cell *N1035,* as 43. The *RMS* value of 0.023 mm is then calculated in cell *N1037* by dividing cell *M1031* (sum of $(\Delta_i)^{0.5}$ values) by cell *N1035* (total number of windows).
8. The next step is to choose a new window size. For this example the new window size is chosen as 3.85 mm. The profile is then subdivided into sections of 3.85 mm width as shown in figure 12.

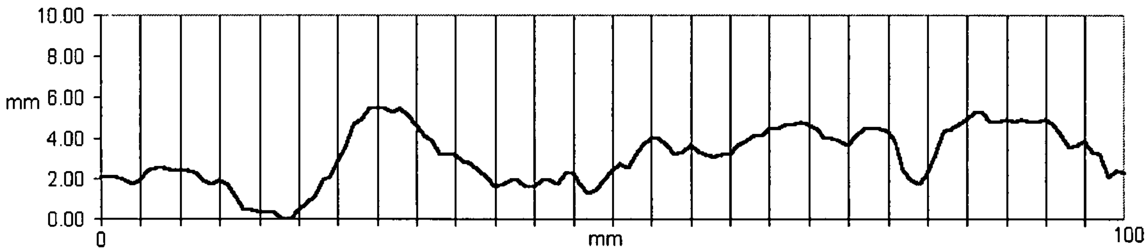

Figure 12 - JRC standard profile number ten subdivided by windows of 3.85 mm width. Note, this figure has a vertical exaggeration of 2;1.

9. Steps 2 through 4 are then repeated with the new window width. The slope and intercept for the first window are calculated in cells *D3..D8* and *C3..D8* of the spreadsheet, respectively. The residual values are calculated in column *Q* of the spreadsheet, using the same procedure as for the 2.31 mm window size. For the 3.85

mm window width, there are 26 total windows with 6 points per window. The number of windows is calculated as cell *Q1033* of the spreadsheet.

10. Equation 19 is then entered with the information from step 7, and the *RMS* value of 0.033 mm returned for the 3.85 mm window size. This is accomplished by dividing the sum of the $(\Delta_i)^{0.5}$ values, calculated in *Q1031,* by the number of windows, calculated in *Q 1033,* as shown in cell *Q1035.*

11. Steps 2 through 5 are again repeated for the next window size. For this example the new window size is chosen as 5.39 mm. The profile is then subdivided into sections of 5.39 mm width as shown in figure 13.

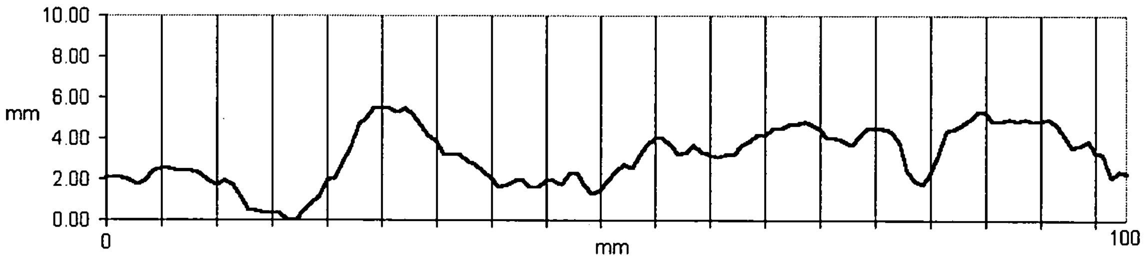

Figure 13 - JRC standard profile number ten subdivided by windows of 5.39 mm width. Note, this figure has a vertical exaggeration of 2:1.

12. Steps 2 through 4 are again performed to determine the parameters for use in equation 19. For the 5.39 mm window width, there are 18 total windows with 8 points per window. For the first 5.39 mm window, the slope and intercept of the detrending line are calculated as cells *C3..C10* and *D3..D10* and the residuals to the line in *U3..U10.* The sum of the $(\Delta_i)^{0.5}$ values is calculated in *cell U1031* and the number of windows in *U1033.*

13. Equation 20 is entered with the information from step 10 and the *RMS* value of 0.039 returned for the 5.39 mm window size. The *RMS* value for the 5.39 mm

window width is calculated as cell *U1035*.

14. To determine the fractal parameters, the logarithms of the *RMS* values (0.023, 0.033 and 0.039 mm) are plotted versus the logarithms of the corresponding window widths (2.31, 3.85 and 5.39 mm). A linear regression is then performed on the corresponding data points. The slope of the line is used to estimate the fractal dimension according to equation 21. The intercept of the line is also recorded. For this example the line formed by the regression of the three data points had a slope, β, of 0.64 and an intercept of -1.87. Using equation 21, the fractal dimension determined from this simple example for JRC profile number ten was 1.36. The log-log plot and resulting linear regression is shown as figure 14.

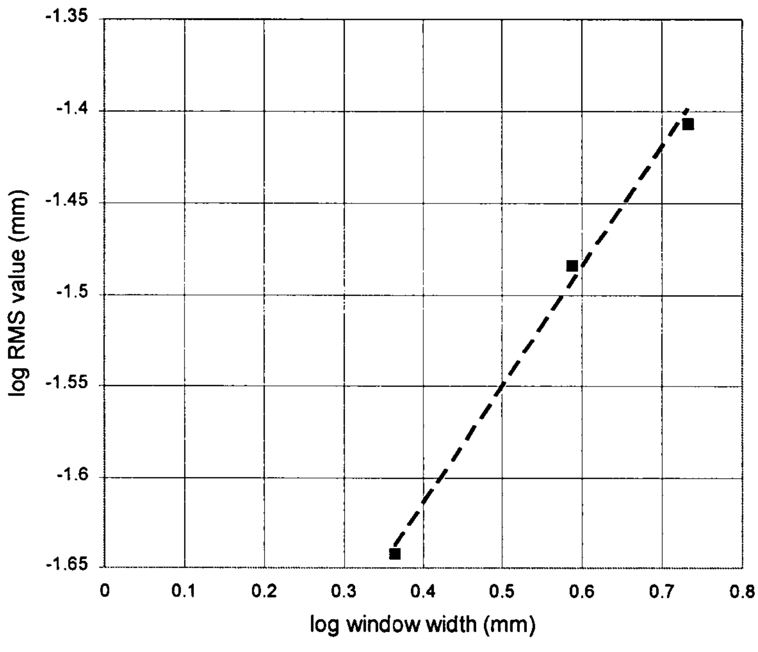

Figure 14 - Plot of log *RMS* values versus log window widths. The line in the figure, which has a slope of 0.64 and an intercept of -1.87, is from the regression of the three data points used in the *RMS* method example.

Since the method involves the horizontal sectioning of the vertical section plane (profile) it is applicable to self-affine objects. The method is however limited by the accuracy of the equipment used to digitize the discontinuity surface, since the horizontal spacing of the points comprising the profile defines the smallest window size that could be used. The actual profile has an infinite number of horizontal intercepts but the intercepts smaller than the horizontal resolution of the profilometer are lost. The number of horizontal intercepts lost is a function of the horizontal resolution of the profilometer. At the opposite end of the spectrum, the larger features of the section are lost by the imposition of the finite length profile. Since the longer chords are not present, only small window sizes obey the power law (log-log) necessary for the fractal dimension calculation (Russ, 1994). This explains the break from the linear slope seen at longer step sizes (window lengths) in all fractal dimensioning methods for rock discontinuities. Figure 15 demonstrates the break from the initial linear slope for data obtained by the *RMS* method using Joint Roughness Coefficient standard profile number seven

Variogram Method

The next method to be forwarded is the variogram or semi-variogram method developed by Mark and Aronson (Russ, 1994). The variogram method is similar to the RMS method in that windows of varying width are positioned along the horizontal axis. In the variogram method however, the average sum of the squares of the differences in height between the points of the profile are calculated for a given window width. Figure 16 shows the use of windowing to evaluate differences in elevations ($\Delta z = z(x_i)-z(x_i + h)$) for two

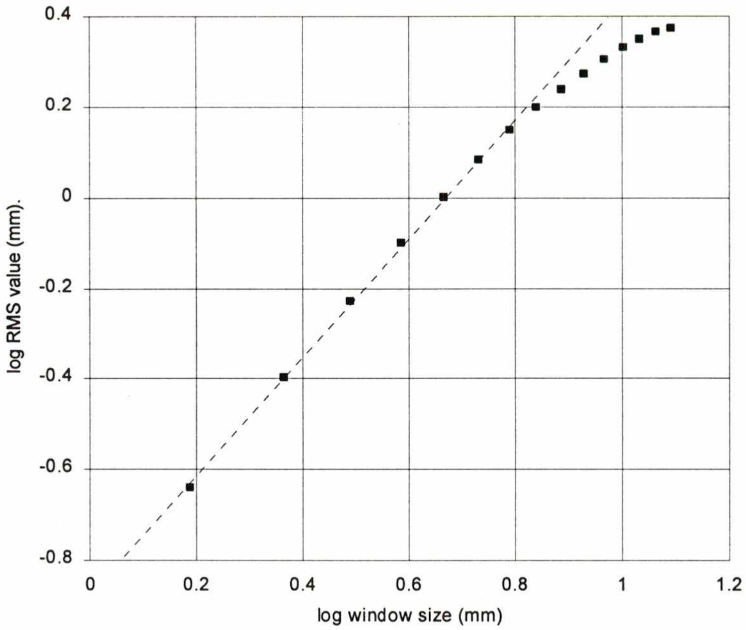

Figure 15 - Graph of log *RMS* value versus log window size showing the break from a linear slope at larger window sizes for JRC profile number seven.

window sizes, h, (figure 16a) and $2h$ (figure 16b). The one-dimensional variogram function, $\gamma(h)$ can be expressed in discrete form as:

$$\gamma(h) = \frac{1}{2N} \sum_{i=1}^{N} [z(x_i) - z(x_i + h)]^2 \qquad \textbf{(22)}$$

where N is the total number of pairs of roughness profile heights with elevations of $z(x_i)$ and $z(x_i + h)$ spaced at the lag (window) width h. Several values of h are selected for which the respective values of $\gamma(h)$ are calculated. Log $\gamma(h)$ values are then plotted versus the log window widths (h) and the fractal dimension is related to the slope, β, of the resulting line according to:

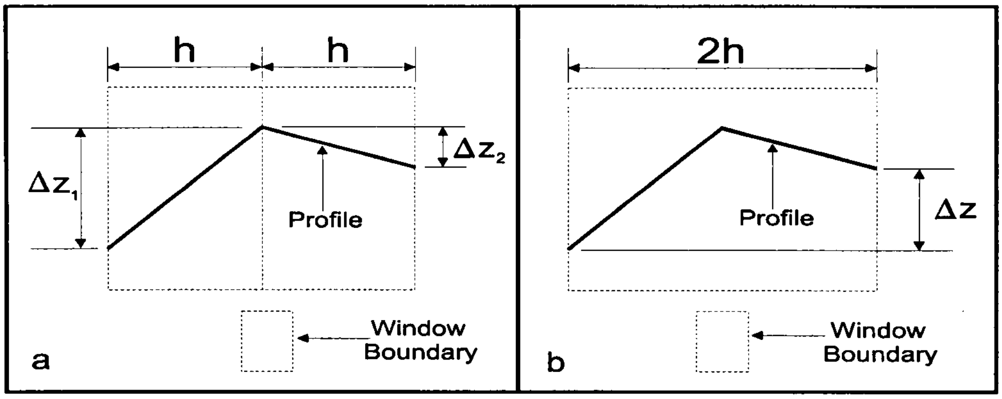

Figure 16 - A diagram showing how windows of varying width, h, are used in the calculation of Δz for the variogram method.

$$D = 2 - \frac{\beta}{2} \tag{23}$$

where D is the fractal dimension.

The necessary calculations were performed in a spreadsheet developed in *Microsoft Excel version 7.0.* The variogram method can be used for the calculation of fractal dimensions for self-affine objects due to the imposed horizontal sectioning (windowing). The variogram method also suffers from the two limitations of horizontal resolution and finite profile length as did the RMS method.

Example of the Variogram Method

To demonstrate the variogram method, an example has been developed using JRC profile number 10. In order to simplify the example, only three window sizes will be examined. For the first window size, the calculations within one window will be described.

In actuality, several window sizes are used for the calculation of the fractal parameters. Since the number of windows necessary to calculate the fractal parameters is large; spreadsheet templates were developed to automate the process. With the spreadsheet templates, one would simply copy the coordinates composing the profile into the correct columns of the template and the calculations would be performed automatically. The formulae used in the variogram spreadsheet template are shown, in spreadsheet form, as appendix D.

1. The first step in the calculation of the fractal parameters is to subdivide the profile using the first window size. For this example, JRC profile ten is subdivided by windows of 2.31 mm width as shown in figure 10. The values chosen for window widths are functions of the horizontal spacing of the digitized points composing the profile. JRC profile number 10 was digitized at a horizontal resolution of 0.77 mm. Therefore, all window widths are multiples of the 0.77 mm horizontal resolution.
2. The variogram value is then calculated for all the windows of 2.31 mm width. For this example, the first window, denoted by the cross-hatching in figure 10, will be examined. First, the difference in height, Δz, between the intersections of the profile with the two endpoints of the window is calculated. For the first window, Δz is equal to 0.30 mm as shown in figure 17. For the variogram spreadsheet shown in appendix D, this calculation is made in cell *E4*. The calculation in cell *E4* is made by subtracting the *z* coordinate corresponding to the right side of the window in cell *B4,* from the *z* coordinate corresponding to the left side of the window in cell *B2*. The quantity *(B4-B2)* is then squared ($(B4-B2)^2$).

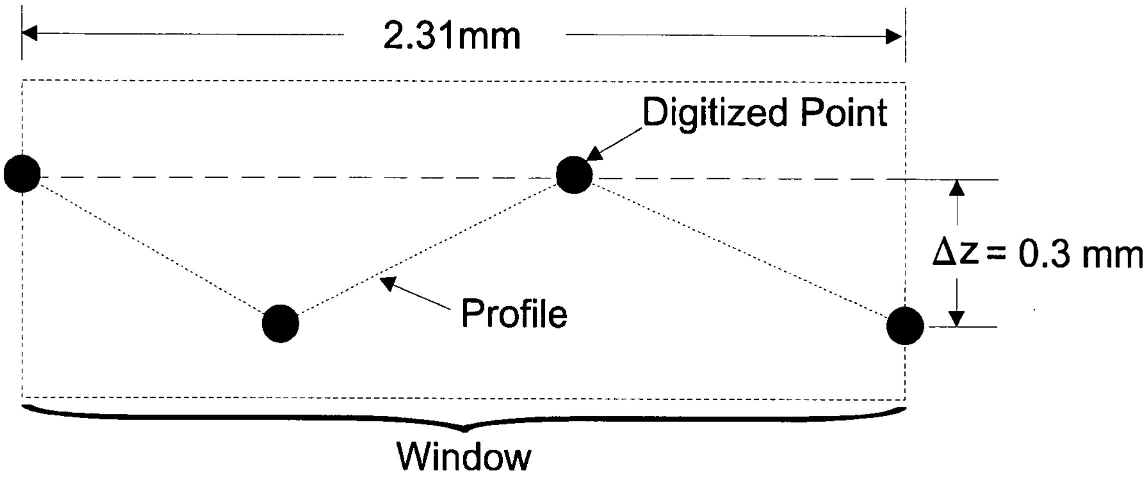

Figure 17 - Diagram showing the calculation of the Δz value for one window of the variogram method. The difference in height, Δz, is measured from the intersection of the window boundaries with the joint profile. In this case the difference in height, Δz, was 0.30 mm.

3. Next, the remaining windows are examined as described for the first window in step number 2. These calculations are shown in column *E* of the variogram spreadsheet. The height difference values for all windows are then squared and summed. In the case of the 2.31 mm window size, this step yielded a value of 34.4 mm. The summation of the squared elevation difference values is shown as cell *E10* in the spreadsheet. This is done using the command *SUM(E3:E8)*, in cell *E10.*
4. The value determined in step 3 is then divided by two times the total number of windows. For the 2.31 mm window size there are 43 windows. The number of windows is calculated using the logical operators shown in column *C*. The sum of the number of windows is determined using the command *SUM(C3:C8),* in cell *C10.* The variogram function value for the 2.31 mm window size, as calculated from equation 22, is 0.40 mm. This step is accomplished by dividing the sum of the squared elevation difference values (cell *E10*) by two time the number of windows (2**C10*) in cell *D14.*

5. The next step is to choose a new window size. For this example, the new window size is 3.85 mm. The profile is then subdivided into sections of 3.85 mm width as shown in figure 12.
6. Steps 2 through 4 are repeated using the new window size. The calculations of the elevation differences for the 3.85 mm window size are shown in column *F* of the spreadsheet. For the 3.85 mm window size, the sum of the differences in height between the intersections of the profile with the window boundaries is 41.6 mm. The sum of the differences is calculated in cell *F10* of the spreadsheet. The total number of windows is 26. The variogram function (Eqn. 22) value is then calculated as 0.80 mm in cell *D15*.
7. The next step is to choose a new window size. For this example, the new window size is 5.39 mm. The profile is then be subdivided into sections of 5.39 mm width as shown in figure 13.
8. Steps 2 through 4 are repeated using the new window size. The differences in height between the intersections of the profile with the windows are calculated in column *H* of the spreadsheet. For the 5.39 mm window size, the sum of the differences in height between the intersections of the profile with the window boundaries is 43.6 mm. The differences in height are summed in cell *H10*. The total number of windows for the 5.39 mm window size is 18. The variogram function (Eqn. 22) value is then calculated as 1.21 mm in cell *D17*.
9. To determine the fractal parameters, the logarithms of the variogram function values (0.40, 0.80 and 1.21 mm) are plotted versus the logarithms of the corresponding window

widths (2.31, 3.85 and 5.39 mm). A linear regression is then performed on the corresponding data points. The slope of the line is used to estimate the fractal dimension according to equation 23. The intercept of the linear regression is also recorded. For this example, the line formed by the regression of the three data points had a slope, β, of 1.31 and an intercept of -0.87. Using equation 23, the fractal dimension determined from this simple example for JRC profile number ten was 1.34. The log-log plot and resulting linear regression is shown as figure 18.

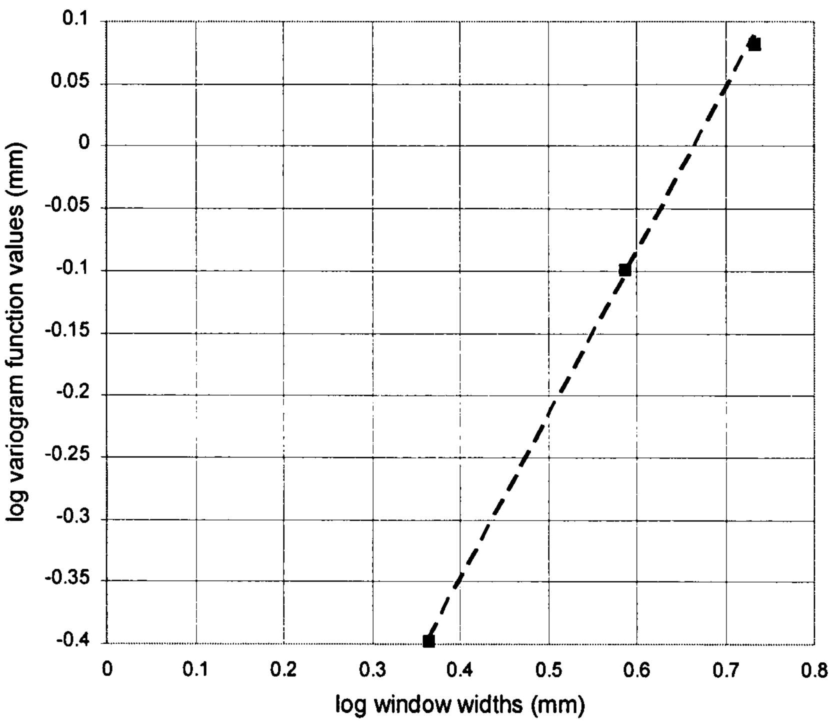

Figure 18 - Plot of log variogram function values versus log window widths. The line in the figure , which had a slope of 1.31 and an intercept of -0.87, is from the regression of the three data points used in the variogram method example.

Window Average Microangle Method

The Window Average Microangle (*WAM*) method was developed as a result of this study. The *WAM* method was developed based upon a discussion of Rengers' analysis of roughness found in Goodman's *Introduction to Rock Mechanics* (1989). Rengers' analysis can be described by the two figures 19 and 20. In figure 19 a profile of a rock joint is subdivided into sections having a unit width, *h*. According to Goodman (1989), any two points separated by a distance *h* define a line inclined at an angle α with the mean plane through the joint profile.

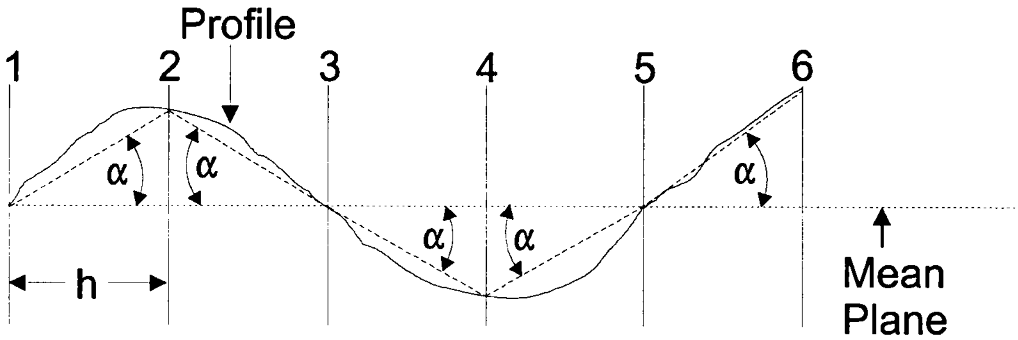

Figure 19 - Rengers' profile sectioning showing the calculation of α; after Goodman (1989).

If the sections are moved along the profile and the section widths varied, a series of angles for each section width would be measured. Figure 20 shows a plot of the measured angles versus the section width, *h*. Envelopes to the measured angles have been constructed which show how the measured angles decrease proportionally with increasing section width.

As with the *RMS* and variogram methods, horizontal windows of increasing width were used to subdivide the profile into sections over which some value was calculated. The windowing method for two window widths is shown in figure 21. In the *WAM* method the absolute value of the angle, from the horizontal, formed by the intersection of the profile with the sides of the window was calculated. The concept is illustrated for two window sizes in figure 22 and is shown in equation form in equation 24. The absolute values of the angles

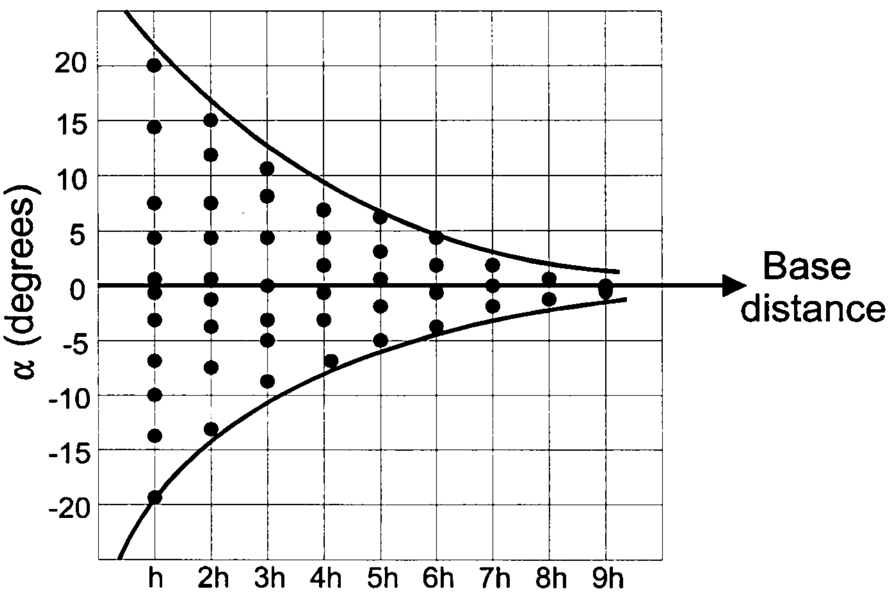

Figure 20 - Rengers' angle envelope; after Goodman (1989).

$$\theta_i = \tan^{-1}\left(\frac{z(x_i+h) - z(x_i)}{(x_i+h) - (x_i)}\right) \tag{24}$$

for each series of windows were then summed and averaged to obtain the *WAM(h)* value for each window size, *h* according to:

$$WAM(h) = \frac{1}{n_w}\sum_{i=1}^{n_w} ABS(\theta_i). \tag{25}$$

In equations 24 and 25, n_w is the number of windows of width *h* having elevations of $z(x_i)$ at x_i, and $z(x_i + h)$ at $(x_i + h)$. Several values of *h* are selected and the corresponding values of *WAM(h)* calculated. The values of *WAM(h)* are then plotted versus the respective *h* widths

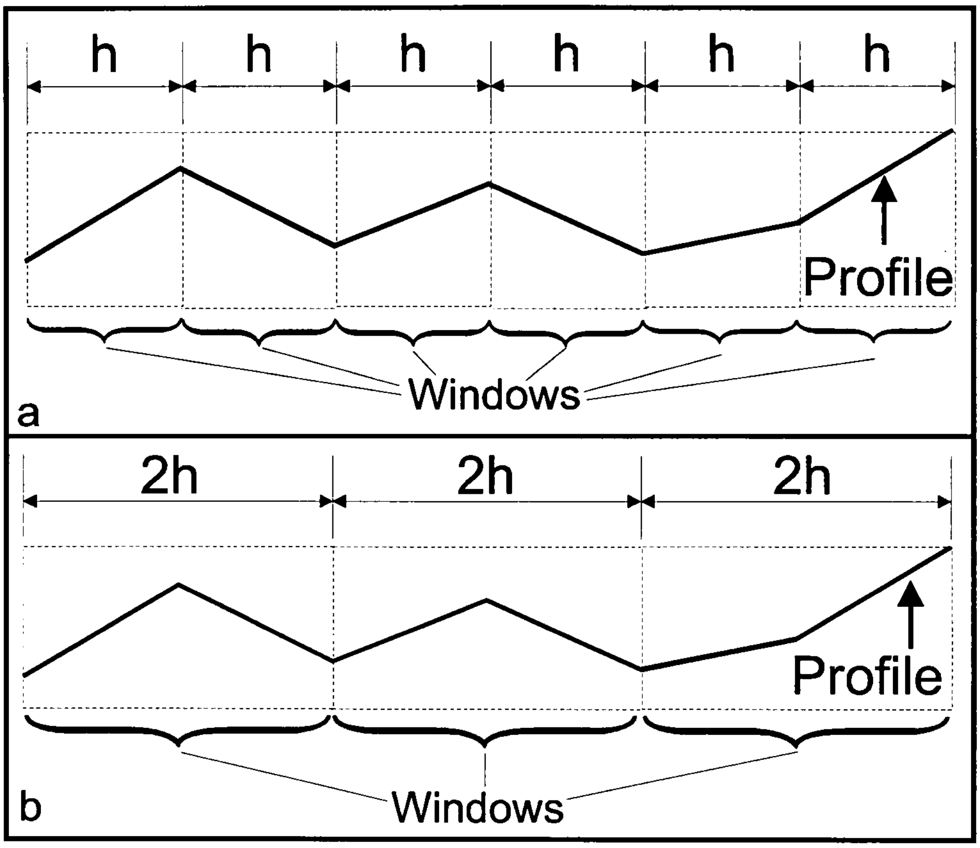

Figure 21- Diagram showing the windowing procedure for the *WAM* method. (a) Window widths h and (b) window widths $2h$.

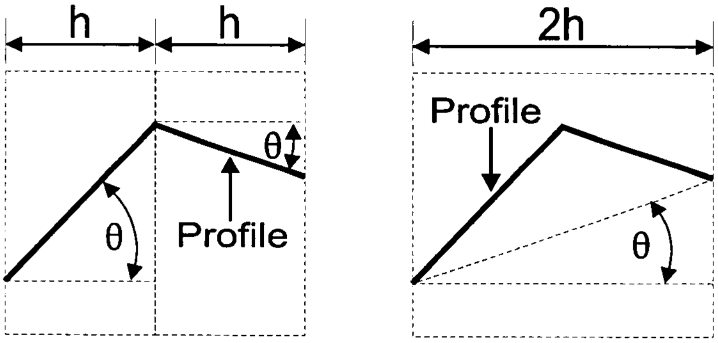

Figure 22 - A diagram showing how windows are used in the calculation of θ for the *WAM* method.

and the fractal dimension calculated from the slope, β, of the resulting line by:

$$D = 1 - \beta \tag{26}$$

where D is the fractal dimension.

The calculations necessary to determine the various parameters were completed in a *Microsoft Excel version 7.0* spreadsheet. The use of horizontal sectioning (windowing) in the *WAM* method, like the other methods discussed this far, ensures its applicability to the calculation of fractal dimensions for self-affine objects. The method is also vulnerable to the pitfalls of dependance on the maximum horizontal resolution of the profile generating equipment and loss of long roughness wavelengths due to finite sample sizes.

Example of the *WAM* Method

To demonstrate the *WAM* method, an example has been developed using JRC profile number 10. In order to simplify the example, only three window sizes will be examined. For the first window size, the calculations within one window will be described. In actuality, several window sizes would be used for the calculation of the fractal parameters. Since the number of windows necessary to calculate the fractal parameters is large; spreadsheet templates were developed to automate the process. With the spreadsheet templates, one would simply copy the coordinates composing the profile into the correct columns of the template and the calculations would be performed automatically. The formulae used in the *WAM* spreadsheet template are shown, in spreadsheet form, as Appendix E.

1. The first step in the calculation of the fractal parameters is to subdivide the profile

using the first window size. For this example, JRC profile ten is subdivided by windows of 2.31 mm width as shown in figure 10. The values chosen for window widths are functions of the horizontal spacing of the data points composing the profile. JRC profile number 10 was digitized at a horizontal resolution of 0.77 mm. Therefore, all window widths are multiples of the 0.77 mm horizontal resolution.

2. The angle, θ_i (eqn. 24), is then calculated for all the windows of 2.31 mm width. For this example, the first window, denoted by the cross-hatching in figure 10, will be examined. θ_i is the angle, measured from the horizontal, formed by the intersection of the profile with the sides of the window. As shown in equation 24, determining θ_i involved estimating the difference in height between the two intersection points of the profile with the window boundaries. For the first window of 2.31 mm width, this equaled 0.30 mm. The angle, θ_i, is then determined by taking the arc tangent of the height difference (0.30 mm) divided by the window width (2.31 mm). For the first window, this value was -7.40 degrees as shown in figure 23. The previous step is completed in cell *E4* of the *WAM* spreadsheet shown in appendix E. In cell *E4*, the elevation difference between the two sides of the windows is calculated as *B4-B2*, where *B4* is the *z* coordinate of the digitized point at the right window intercept and *B2* is the *z* coordinate of the digitized point at the left window intercept. The quantity *(B4-B2)* is then divided by the window width calculated as *(A4-A2)*. The next step in cell *E4* is to take the arc tangent of the quantity *(B4-B2)/(A4-A2)*. We now have the θ_i value of -7.40 degrees in cell *E4*.

3. Next, the remaining windows are examined as described for the first window in step

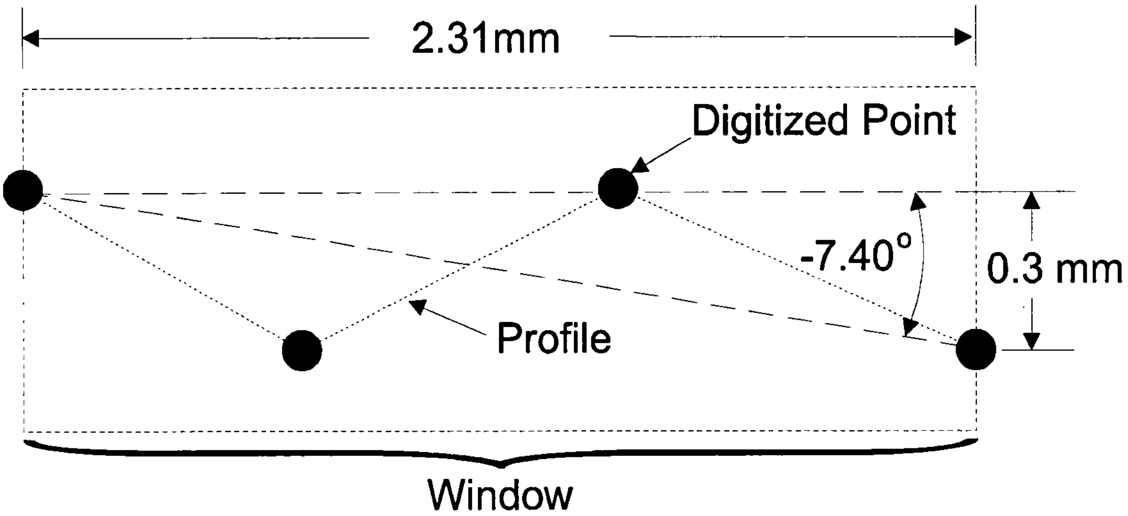

Figure 23 - Diagram showing the method used to calculate the angle for one window of the *WAM* method. First, the difference in height (0.3 mm), between the intersections of the window with the profile, is calculated. The angle (-7.40 degrees) is then calculated by taking the arc tangent of the height difference divided by the window width (2.31 mm).

number 2. The angles for the remaining windows are calculated in column *E* of the spreadsheet. The absolute values of the angles are then summed and divided by the total number of windows (43). The absolute values of the angles are determined by using the command *ABS* on the θ_i values from step 2. The *ABS*(θ_i) values from column *E* are then summed using the command *SUM(E4..E14)* in cell *E15*. The number of windows are then calculated using the logical operator (cell *C4*) summed in cell *C15*. The *WAM* value is then calculated by dividing the sum of the *ABS*(θ_i) values (cell *E15*) by the number of windows (cell *C15*) in cell *D19*. For the 2.31 mm window width this yielded a *WAM* value of 15.2 degrees.

4. The next step is to choose a new window size. For this example, the new window size is 3.85 mm. The profile was then subdivided into sections of 3.85 mm width, as shown in figure 12.

5. Steps 2 and 3 are then repeated using the new window size. For the 3.85 mm window size, the *WAM* value was 13.2 degrees. The angles for all windows of 3.85 mm width are calculated in column *F* of the spreadsheet. The sum of the absolute values of the angles is calculated in cell *F15* of the spreadsheet. The sum of the angles is then divided by the number of windows in cell *D20*, which yielded the value of 13.2 degrees.
6. The next step is to choose a new window size. For this example, the new window size is 5.39 mm. The profile is then subdivided into sections of 5.39 mm width as shown in figure 13.
7. Steps 2 and 3 are repeated using the new window size. For the 5.39 mm window size the *WAM* value is 12.1 degrees. The absolute values of the angles for each of the windows are calculated in column *G* of the spreadsheet. The absolute values of the angles are then summed in cell *G15*. The *WAM* value of 12.1 degrees is calculated in cell *D21*.
8. To determine the fractal parameters, the logarithms of the *WAM* values (15.2, 13.2 and 12.1 degrees) are plotted versus the logarithms of the corresponding window widths (2.31, 3.85 and 5.39 mm). A linear regression is then performed on the corresponding data points. The slope of the line is used to estimate the fractal dimension according to equation 26. The intercept of the linear regression is also be recorded. For this example the line formed by the regression of the three data points had a slope, β, of -0.27 and an intercept of 1.28. Using equation 26, the fractal dimension determined from this simple example for JRC profile number ten was

1.27. The log-log plot and resulting linear regression is shown as figure 24.

Verification of Self-Affine Fractal Methods

In order to ensure the methods presented for calculating the fractal dimension were being implemented correctly, a procedure was developed to test the methods with self-affine functions of known fractal dimensions. The method chosen to create the curves of known fractal dimensions was a fractional Brownian motion (fBm) computer program packaged with Russ's *Fractal Surfaces* (1994). Quoting Mandelbrot, "I coined the term fractal from the Latin *fractus*, which describes the appearance of a broken stone: irregular and

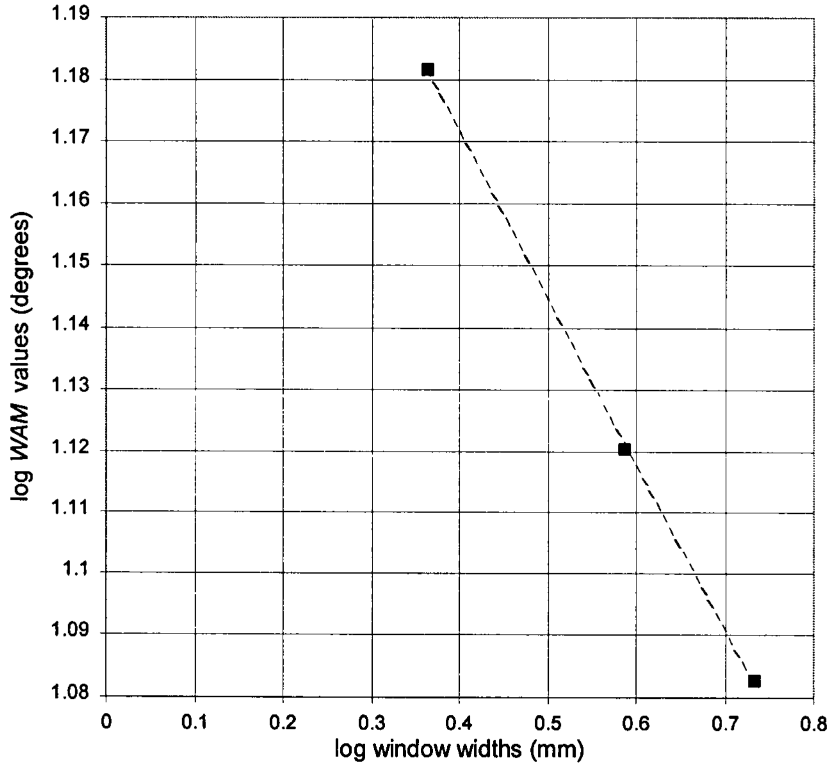

Figure 24 - Plot of log *WAM* values versus log window widths. The line in the figure, which has a slope of -0.27 and an intercept of 1.28, is from the regression of the three data points used in the example.

fragmented. Etymology cannot force an actual stone's surface to be fractal, but it is surely not a standard surface, and it should be fractal if it is scaling. The science of wear and of friction ...supports the belief that *fractional* Brown surfaces provide first approximation representations ...for many natural surfaces" (Mandelbrot 1983). The fBm function was selected due to its unique ability to model natural profiles such as rock joints. This should verify the ability of the aforementioned methods' ability to calculate a fractal dimension related to natural shapes.

The fBm generator uses successive random additions with a Gaussian random number generator to construct the profiles. The fractal dimension of fBm profiles are related to the fractal dimension by:

$$D = 2 - H \tag{27}$$

where D is the fractal dimension and H is known as the Hurst exponent. The Hurst exponent is a spatial/temporal correlation factor. It was developed from studies of the year to year water level fluctuations of the Nile River. The Hurst exponent for natural phenomena ranges from between one-half and one. This is related to the fact that natural surfaces show some spatial correlation between one point and the next. Alternatively, Hurst exponents greater than one-half would be used for modeling systems which show no spatial correlation (Mandelbrot 1983). Odling (1994) has also shown that rock discontinuities can be modeled by Hurst exponents between one-half and one. Therefore, fBm functions were generated for Hurst exponents between one-half and one. The generated profiles were then input into the previously mentioned spreadsheets and the fractal dimensions calculated. The results for the

RMS and variogram methods are shown in figure 25. The results were then analyzed in the spreadsheet resulting in a multiple R of 0.9844 and a standard error of 0.0307 for the variogram method and a multiple R of 0.9222 with a standard error of 0.0676 for the *RMS* method. A multiple R of 1.0 and a standard error of 0 would have meant that the methods predicted the theoretical fractal dimensions perfectly.

The same procedure was used to evaluate the *WAM* method, only a larger number of fBm "profiles" were used to generate a more meaningful statistical sample. Five fBm functions were generated for each of the Hurst exponents ranging from 0.5 to 1.0 in increments of 0.05. The results are shown graphically in figure 26. The resulting statistical analysis yielded a multiple R of 0.9814 with a standard error of 0.0309. Since a larger

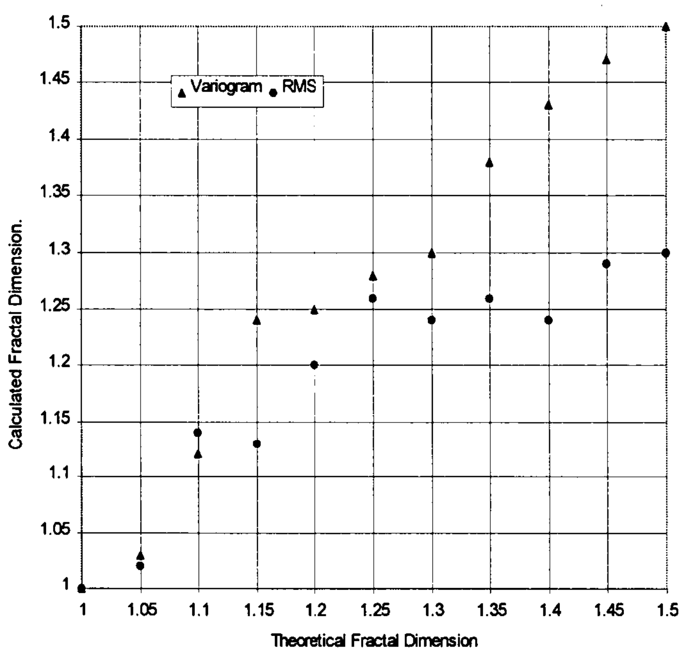

Figure 25 - A plot of calculated versus theoretical fractal dimension for the *RMS* and variogram methods.

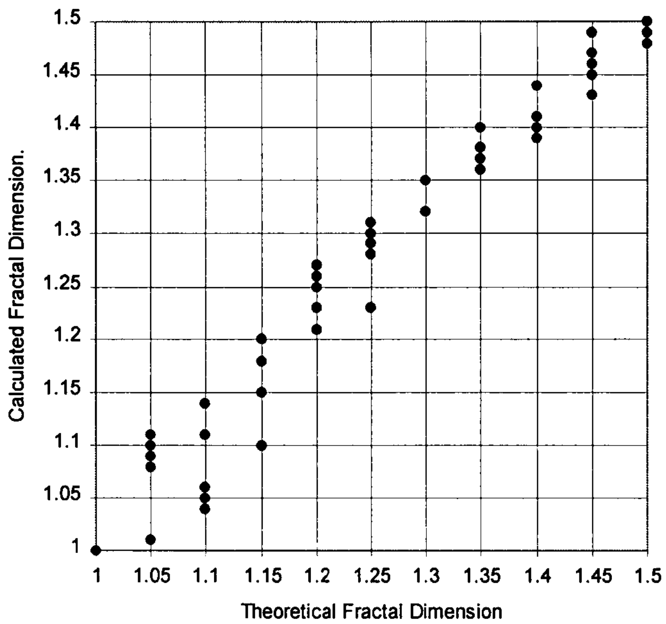

Figure 26 - A plot of calculated versus theoretical fractal dimension for the *WAM* method.

number of profiles were used in the verification of the *WAM* method, the statistical parameters obtained from the verification of the variogram and *RMS* methods could not be compared with those from the verification of the *WAM* method.

The model verifications showed that the variogram and *WAM* methods proved to be the best at predicting the fractal dimension of the fBm function. Both methods worked well for fractal dimensions from 1 to 1.5; however, both tended to overestimate the fractal dimension. The *RMS* method was found to be unsuitable for the estimation of fractal parameters. At fractal dimensions greater than 1.25 the *RMS* method seemed to falter. This was likely caused by the method's inability to evaluate the longer roughness wavelengths present at higher fractal dimensions.

Fractal Parameters

The only fractal parameter mentioned to this point has been the slope of the log-log plot, which has been shown to yield the fractal dimension. Obviously two parameters are obtained from the linear fit; the slope and intercept. The intercept of the linear fit has been largely ignored by all but a few researchers (Hsiung, et al. 1995, Kulatilake, et al. 1995). Ignoring the fractal intercept may have been in error, as the intercept yields the magnitude of roughness (Russ 1994). Figure 27 shows two linear fits generated with the variogram method using JRC standard profile number ten (see figure 4). The solid line is for the standard profile and the dotted line for the standard profile with the elevation values reduced by one-half. The plot shows how the intercept of the reduced-elevation standard profile was reduced significantly from the original standard profile intercept, yet the slopes are the same. It should stand to reason that the magnitude of roughness (intercept) would have more impact on shear strength than the variation of roughness with scale (slope). In this study both the fractal dimension and intercept will be examined.

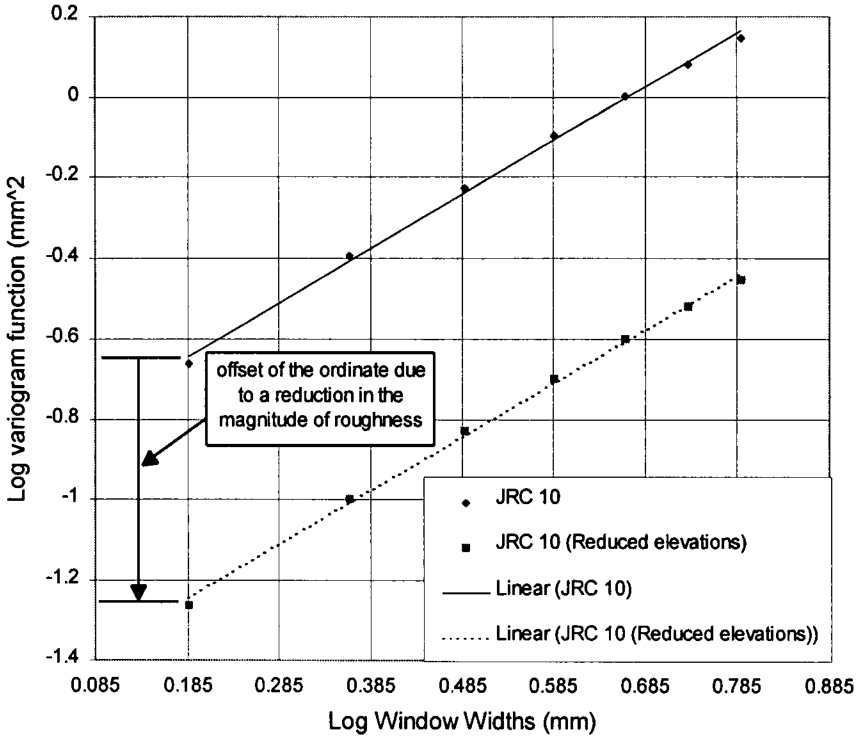

Figure 27 - A plot of log variogram function versus log window widths showing the effect of the magnitude of roughness on the ordinate of the power-law linear fit. The solid line corresponds to JRC profile 10; the dashed line to the same profile with the elevation values reduced by one-half. The slope, β, is the same for both cases.

CHAPTER 5: PROJECTS

Foothills Parkway Project

The Foothills Parkway Project was conceived to link an existing portion of the Foothills Parkway near Townsend, Tennessee through Wears Valley to US Highway 321. The project, to be constructed through a portion of the Great Smoky Mountains National Park, was commissioned by the Federal Highways Administration, while the National Park Service had the responsibility of dealing with environmental and aesthetic concerns. The project was initially begun by the Tennessee Department of Transportation (TDOT). However, design deficiencies and aesthetic concerns forced the project to be overtaken by the Federal Highways Administration (FHWA). The geotechnical investigation was contracted by FHWA for certain aspects of the project. The geotechnical contractor selected was HDR Engineering (HDR), Pittsburgh, Pennsylvania.

The project corridor is along the portion of the Appalachian Mountains which includes Wears Valley. The topography of this region is very rugged with steep-sided valleys. The use of design and conventional road construction techniques would require large volumes of cut and fill. To eliminate excavation of large volumes of material and to minimize adverse environmental impacts, the alternative of spanning the valleys with bridges was adopted. A series of ten bridges have been designed for construction along the proposed roadway. The planned bridging operation is unique in that the bridges would be supported only at the abutments (on the ridge lines) once completed. During construction, the precast concrete epoxy-bound spans would be supported by temporary piers. Once the spans were complete the piers would be removed and all loads would be transferred to the abutments. This plan would limit the environmental impact to the pier and abutment locations.

The geotechnical investigation by HDR was obligated to be conducted within the strict environmental guidelines imposed by the National Park Service. Again, another ingenious plan was developed to satisfy environmental concerns. The sampling points, located near proposed abutment and temporary pier locations, were not readily accessible from a previously constructed access road. The solution was to use the access road to get as near as possible to the temporary pier locations and with a bulldozer construct drill pads. Then, using helicopters, drilling rigs were lowered onto the preconstructed drilling pads. Using this system, only small areas of the forest were compromised for the geotechnical investigation.

Geology of the Foothills Region

The Foothills Parkway Project is located in the Foothills of the Great Smoky Mountains. Samples for this study were obtained from rock core of the Shields Formation of the Walden Creek Group. These rocks are Precambrian age and are described as massive conglomerate, sandstone, and argillaceous slate (Hardeman, 1966). The rocks are all low grade metamorphic rocks, regarded as metasedimentary. Such rocks have been metamorphosed, but not beyond recognition of their sedimentary properties.

The samples tested in this study consisted of core samples (NX size) of three rock types; sandstone, conglomerate, and slate. The sandstone is well-sorted, medium-grained, and arkosic. The primary mineral constituents are quartz, feldspar, and pyrite bound by a silica cement. Some of the sandstone contains intraclasts of slate. Slight to moderate weathering of the sandstone has resulted in a thin layer of oxide deposition on most discontinuity surfaces. The fine-grained, well-sorted sandstones would generally produce lower fractal intercepts which would increase as grain size increased.

The next rock type tested was the conglomerate. The poorly-sorted conglomerate is mostly composed of rounded pebbles ranging from two to twenty-five millimeters. The pebbles, mostly quartz, are of varying rock types in a matrix of angular quartz grains and feldspar grains. Most of the conglomerate exhibit extreme weathering of the matrix material, as evidenced by iron staining. Weathering has also produced very rough joint profiles due to removal of the matrix, leaving quartz fragments and rock pebbles extending from the surface of the discontinuity. The poor sorting and removal of the matrix would most likely lead to high fractal intercepts since the topography of such a joint surface is very rough.

The rock categorized as slate is an argillaceous rock composed mainly of clay minerals. The slate units are highly anisotropic due to clay recrystallization in a platy orientation parallel to bedding. Due to the structure of these platy minerals, they offer little resistance to shearing. Discontinuities in the slate have very smooth roughness profiles and thus, a low unconfined compressive strength when tested parallel to bedding. The slates would have fractal intercepts less than the sandstones and conglomerates since the discontinuities in this unit have very smooth surfaces.

The primary factor affecting the fractal intercept of discontinuities in the rock types discussed above is the degree of jaggedness. Therefore, the conglomerate is expected to have higher fractal intercepts, on average, than the sandstone or shale. This is related to the removal of the matrix leaving behind large pebbles and quartz grains extending from the discontinuity surface. The sandstone should have discontinuities with fractal intercepts less then the conglomerates. Discontinuities in the sandstone are less jagged due to their smaller grain size. The grain size is the controlling factor on the maximum size feature that comprises the discontinuity surface. By this rational, the slate discontinuities would have the smallest fractal intercepts of all the rocks of the Foothills Parkway Project. This is due to a small grain size but also the recrystallization of clay minerals. This recrystallization has made the slate units highly anisotropic thus producing very smooth discontinuity surfaces.

US Highway 19E Project

The next study site examined was a series of roadcuts along US Highway 19E (US19E) near Biltmore, Tennessee. The cuts, some of which measured forty meters in height, were made ten years ago, during the construction of US19E. The particular slope chosen for sampling was the topic of another study by University of Tennessee Graduate student Scott Arwood. The focus of that study was a new energy model for slope stability in folded rock masses (Arwood, 1996). The cut chosen is the site of a large slope failure, shown in figure 28, which occurred a short period after the cut was made. In the years since construction of US19E, catch fences have been added to prevent spall from the slope entering the roadway. Samples from the slope were obtained during an Institute for Geotechnology field trip conducted August 8, 1996. Members of the trip included Matt Haston, Bill Kupsch, Alex Bredikhin, Michael Yang, and Scott Arwood. Samples were gathered using a crowbar and sledgehammer. Sampling was biased toward areas of the outcrop that were readily

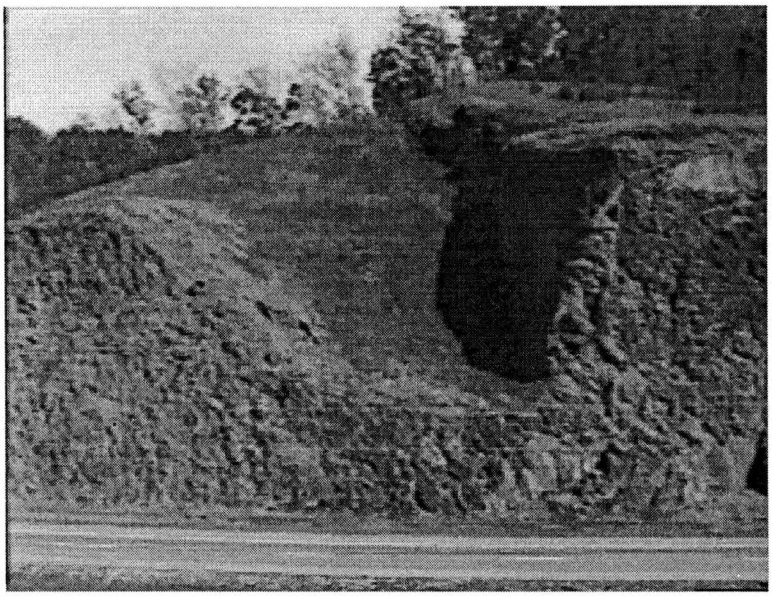

Figure 28 - US-19E slope failure.

accessible i.e., less than a height of 1.5 meters. Since the only tools on hand were simple, samples that could easily be removed were taken. After the rock surrounding the discontinuity had been loosened, the two halves of the discontinuity could be removed. The samples were then scored with chalk to indicate the direction in which they were to be sheared. This direction was determined, relative to the slope, based upon the presumed direction of the slope failure. The samples were then stored in sampling bags.

Geology of the US19E Project Area

The area where the samples were collected is part of the Valley and Ridge province. The topography of the Valley and Ridge province is dominated by numerous parallel narrow ridges, separated by linear valleys. Rock slopes along US19E were formed when these ridges were bisected by the highway alignment. The Ordovician-aged Sevier Shale comprising the rock slopes is part of the Chickamauga Group (Arwood, 1996). Shale at the sampling site has been folded and faulted; although only low grade metamorphism has occurred. The thinly bedded shale at the site was folded in a large syncline. The bedding surface, in the trough of the fold, corresponds to the failure surface. Low grade metamorphism in the form of rock cleavage was also evident in the rock mass.

CHAPTER 6: TESTING EQUIPMENT

Introduction

The samples collected were tested with a digital roughness gage, direct shear and point load test devices. The digital roughness gage is used to obtain measurements of the rock joint surface that can be used to estimate the fractal parameters. The direct shear test is used to determine the peak shear strength of the rock discontinuities and base friction angles from sawn samples. The point load tests are used to determine and average value of the unconfined compressive strength of the rock samples. In this chapter, the equipment used to perform these tests is described.

Direct Shear Testing Machine

The device used for direct shear testing was the Model PHI-10 Portable Shear Box designed by Roctest Inc., Plattsburgh, New York. The PHI-10 was designed based upon work conducted at Imperial College, London. The PHI-10 consists of two elements: the shear box assembly/loading frame and the hydraulic system.

The shear box assembly is composed of upper and lower half-cylinders, each with a diameter of 14.8 cm which contain the molded sample during testing. The lower half-cylinder, fixed to the loading frame, is equipped with a lateral key to prevent rotation of the sample during testing. The geometry of the two cylinders allows for core samples up to 115 mm in diameter or square samples of measuring 115 x 115 mm. The shear load application system, mounted to the loading frame, is composed of two horizontal Enerpac rams each with a working capacity of five tons. The header and valve assembly allows for hydraulic pressure to be shunted to one of the rams so that the sample can be sheared in the forward or reverse direction. The shear load is applied through spherical seat yokes attached to either side of the upper half-cylinder. The normal load application system consists of a vertical U-shaped frame to which a vertical five ton working capacity Enerpac ram is fixed. The normal load is applied to the upper half-cylinder through a spherical seat plate attached to a roller carriage assembly thus preventing skew in the normal load. The shearing load application system is designed to ensure that the shear force be applied exactly in the plane of the discontinuity to be sheared. A extensiometer, used to measure shear displacement, is attached to the upper half-cylinder by means of v-shaped screw clamp.

The second element in the PHI-10 shear device are the hydraulic system consisting of the hydraulic pumps and the pressure maintainer. The shear and normal loadings are developed by the use of two Enerpac ten ton capacity hand driven hydraulic pumps. For the shear load a dual scale (psf and kPa) bourdon type gauge with a follower pointer is used to record the shear loading. A similar apparatus is used for the normal load system except that, unique to the PHI-10 device, a pressure maintainer is mounted on a metallic block fixed to the hydraulic pump to assure that the normal stress is constant throughout the test. The pressure maintainer is a critical portion of the PHI-10 hydraulic system. The component is essential for successful shear tests since the calculated shear strength is uniquely related to the normal pressure. The pressure maintainer is basically a pressure magnifier consisting of a pressure gauge, flexible membrane, pneumatic reservoir, and a floating piston. The pneumatic reservoir is formed from the flexible membrane which makes direct contact with the top extremity of the free-floating piston. The hydraulic fluid pressure acting on the base of the floating piston can be counterbalanced by a much smaller pressure in the pneumatic reservoir since the top surface of the piston is much larger that the bottom surface. An equilibrium can be attained between the applied normal pressure and the pneumatic reservoir pressure which then allows for compensation of changes in normal pressure due to dilation of the sample during a test. The pneumatic reservoir is filled with a prescribed amount of air according to the normal loading.

Digital Roughness Gage

A digital roughness gage was donated by Mark McKeown, a geologist at the U.S. Bureau of Reclamation in Denver, Colorado, to be used as a measuring device for rock discontinuity surface roughness. The gage consists of four basic components; the gage, a parallel port interface, computer program, and a jig to secure the gage in position over the sample. A set of resistors in the gage alter the potential fed into the parallel port interface when the gage is moved. These potentials are then compared with the reference voltages to determine the precise position of the gage. These data are transferred to the computer where a program takes the voltages and converts them into displacement measurements and writes them to a file. The gage has two degrees of freedom (x and z). The positioning of the gage is performed manually.

Jig Assembly

In order to keep the gage in position over the sample a jig was developed. The jig was designed incorporating the lower mold set from the direct shear test. The sample is held in concrete fixed from motion by two retaining screws. The jig was constructed from a piece of pegboard in which a hole was cut to provide a window for the discontinuity, as shown in figure 29. Four small rectangular inserts were also sawed in the board to match the four posts extending from the corners of the lower direct shear mold set. In this manner the jig would be held securely in place by the four posts with the molded discontinuity extending from the center. Next, two fiberglass rods were cut to approximately 15 cm in length and attached to the gage to act as stabilizing rods. Two small aluminum channels were then epoxyed into place parallel to one another on the pegboard jig. The stabilizing rods fit into the channels fixing the gage from movement on the jig. The final arrangement is shown in figures 29 and 30.

Electrical Connections

The digital roughness gage as received was not in working order. The first task was to rewire the gage so information could be passed between it and the computer. The gage

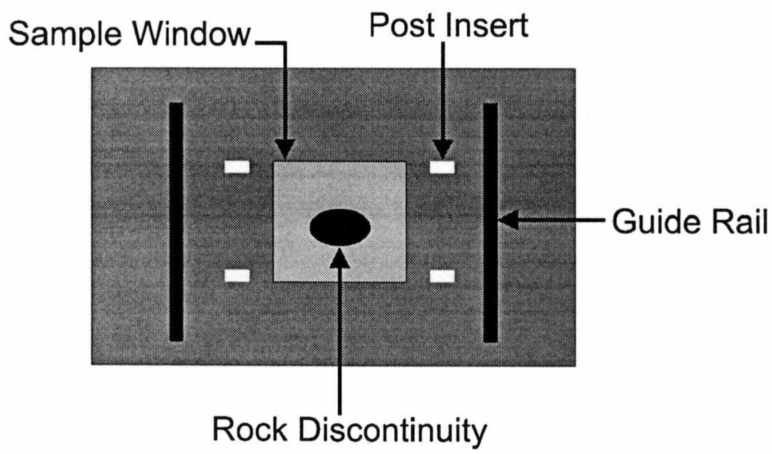

Figure 29 - Digital roughness gage overhead view.

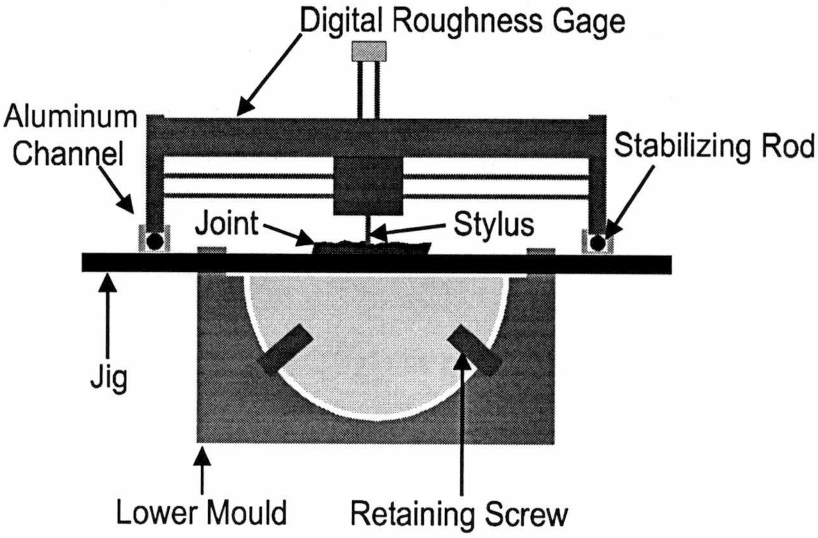

Figure 30 - Digital roughness gage side view.

works on a five volt direct current operating system. This voltage is supplied by a transformer which uses alternating current from any standard wall outlet. The transformer is equipped with a 1.8 mm male plug which is inserted into the side of the parallel port interface. The parallel port interface is equipped with a plastic screw-operated electrical connection system. Various slots are provided for the wires which at the other end are connected to the gage.

In the current configuration, only six of the connection slots are used. The first two are for the five volts supply and the five reference volts. The supply five volts powers the electronics within the parallel port interface and supplies the operating power to the gage. The reference five volts is the standard against which the change in potential caused by movement of the gage is measured. The two positive voltage inputs are wired in parallel at the port. The next two slots are used for input one, which is the variable potential line from the horizontal potentiometer (IN1), and input two used as the variable potential line from the vertical potentiometer (IN0). Lastly, the negative supply and reference five volts are wired in parallel at the far left of the bin of slots. Figure 31 shows the arrangement of the connections at the parallel port interface.

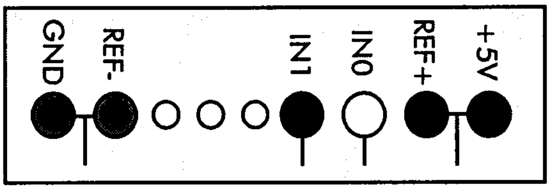

Figure 31 - Parallel port wiring schematic.

Once the wires were connected properly at the parallel port interface they could then be positioned on the gage. A five-strand shielded strain gage wire was used for the connection. A color coded sequence was established for the wiring connections. First the red and black wires were attached in parallel to the +5V and REF+, then to the upper post of the vertical potentiometer and to the middle post (located inside of the slide) of the horizontal potentiometer, respectively. The white wire attached to INO was then soldered to the left vertical potentiometer post numbered two (2). The green wire is then connected from IN1 at the parallel port interface to the upper post on the horizontal potentiometer. Finally, the uncoated ground wire attached in parallel to the REF- and GND is attached to the right lower post on the vertical and to the lower post on the horizontal potentiometer, both numbered three (3). Figure 32 shows the connections at both the vertical and horizontal potentiometers.

The gage should be checked with a multi-meter prior to operation. The gage can be checked by first placing the positive lead of the meter on the +5V connection at the parallel port interface and the negative lead on the REF- and GND connections. This voltage should read close to five volts. The positive lead should then be placed on the REF+ and the negative on the REF- and GND connections. This connection should also read a steady five

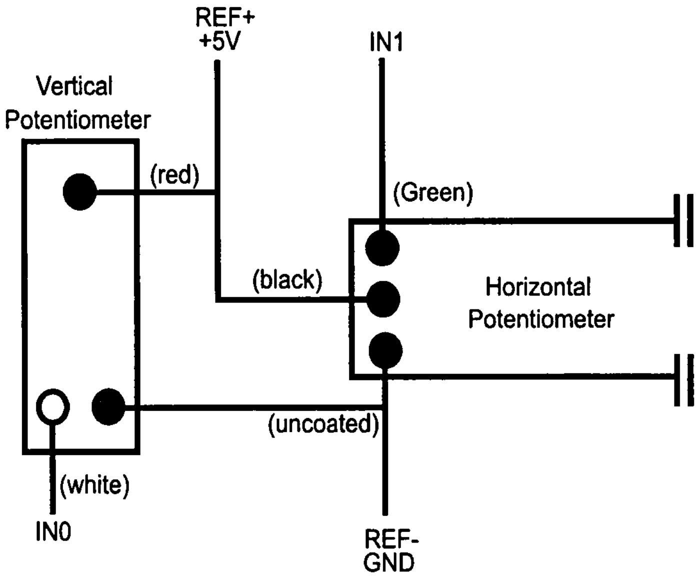

Figure 32 - Potentiometer wiring schematic.

volts. The horizontal and vertical potentiometers can be checked by placing the positive lead of the multi-meter on the IN0 or IN1 connections (depending upon which one is to be tested) and the negative lead on the REF- lead. The voltage measured across IN0 should cycle between zero and five volts as the stylus of the vertical potentiometer is moved thru its entire range. The voltage measured across IN1 should also cycle between zero and five volts as the slide of the horizontal potentiometer is moved thru its entire range.

Computer Program

The electrical signals generated by the gage are read by the parallel port interface and converted into digital signals to be processed by the computer. In this case a program named DRG was written using *Microsoft QuickBASIC* which controls data acquisition and file handling. When started, the program shows an operation guide detailing the operation of the gage when collecting data. Next, the user will be prompted to enter the input voltages and filenames for writing data. The program then shows the current x coordinate of the gage stylus and prompts the user whether to write the current x and z coordinates to a file. The program then prompts the user to reposition the stylus. Lastly, a choice of whether to continue digitizing or exit the program was provided. The code for the basic program, DRG, is shown as appendix B.

Point Load Testing Machine

The device used for point load testing was the model PIL-5 point load tester manufactured by Roctest Inc., Plattsburgh, New York. The PIL-5 was designed based upon the guidelines presented in *International Society for Rock Mechanics Commission on Testing Methods - Suggested Method for Determining Point Load Strength* (ISRM, 1985). The PIL-5 consist of a rigid loading frame and a hydraulic system.

The rigid frame assembly contains the hydraulic system, conical load platens, and a graduated scale for recording platen separation distance. The hydraulic piston used in the PIL-5 has a capacity of five tons which corresponds to a maximum pressure of 39 MPa. The piston is mounted in the base of the rigid frame as shown in figure 33. The lower conical platen is mounted to the piston while the upper platen is mounted to the rigid frame. The lower platen is moved upward by a lever attached to the hydraulic piston. A quick-connect coupling was provided on the rigid frame for the attachment of a pressure gage. The gage has a pressure range of 0-41 MPa and is equipped with a follower needle. Platen separation distance is measured by a small graduated scale attached to the rigid frame. The conical platens follow ISRM standards and are shown in figure 34.

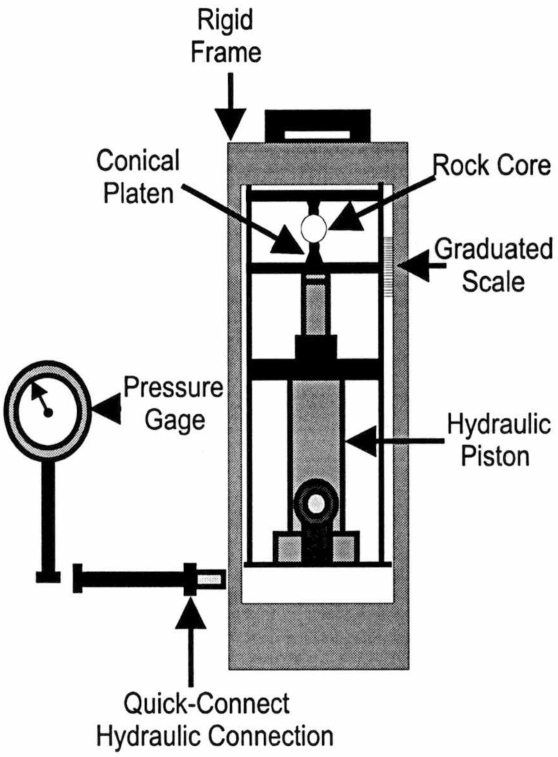

Figure 33 - Point load machine.

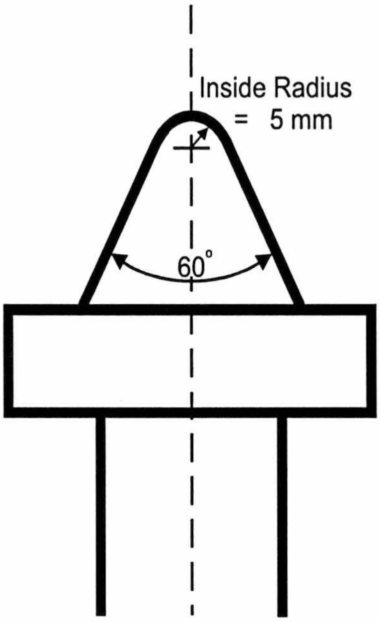

Figure 34 - Conical platen used in the point load testing machine.

CHAPTER 7: SAMPLE PREPARATION AND TESTING

Sample Preparation

The samples must first be trimmed to fit in the PHI-10 moulds. The sample should be no more than 115 mm in width or length and no more than 50 mm in height as measured from either side of the surface of the discontinuity. The 50mm diameter cores of the Foothills Parkway Project were trimmed with a three pound Estwing metal hammer and three inch cold strike. The method involved wrapping the side of the discontinuity to be trimmed in foam to limit disturbance to the discontinuity then placing the wrapped sample on a firm, steady surface. Next, the cold strike was placed on the sample approximately 50mm from the discontinuity and a swift, hard blow was applied to the strike with the hammer. The procedure resulted in a tensile failure of the core at the position where the strike was placed.

The irregularly shaped Sevier Shale samples of the US19E Project were more difficult to trim than the core samples. The US19E samples were sawn with a slab saw before testing. First, the samples as taken from the site were marked with chalk lines where the saw cuts were to be made. Next, both halves of the discontinuity were mated and secured in the correct position with wooden shims and the adjustable fastener incorporated into the saw. The safety hood was closed and the water that cooled the saw blade was valved on before the saw was started. The start button of the saw was activated and the hydraulic arm controlling the travel of the saw was adjusted into cut mode. When the saw blade made contact with the sample the hydraulic pressure was adjusted to forty pounds per square inch as this value seemed to provide the best rate of sawing. When the sample was completely sawed, as evidenced through the plexiglass viewport, the saw was stopped and the sampled removed and allowed to dry. The hydraulic arm was then returned manually as the hydraulic system that controlled the return did not function. None of the US-19E samples required any trimming to reduce their height.

The two halves of the discontinuity were then mated and bound with 18 gage uncoated wire to prevent movement of one half of the sample with respect to the other during the positioning and moulding phases. The sample is then placed in the locating clamp supplied with the PHI-10 shear device as shown in figure 35. The correct positioning of the

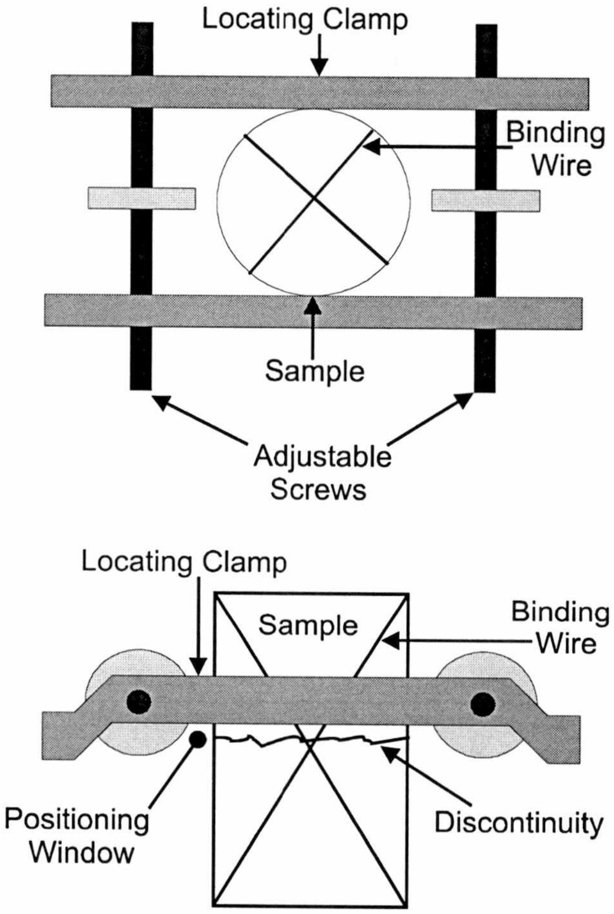

Figure 35 - A sample with the joint aligned correctly in the locating clamp.

sample in the locating clamp is of utmost importance. The discontinuity must be leveled using both the positioning window on the locating clamp and the targeting crosshairs on the acrylic side plates attached to the lower mold. The most effective manner to level the discontinuity is to use the positioning window as a rough guide and then to fine tune the position with the targeting crosshairs while the locating clamp is in position on the lower mould. When the shear plane has been properly leveled check to make sure that the discontinuity is positioned vertically within the bounds of the targeting window on the acrylic side plate. If the shear plane is not within the window it should be repositioned or the sample will be contaiminated with cement during moulding. Once the discontinuity has been properly positioned it should be placed in the upper half of the mould for safe keeping.

Sample Molding

In the moulding procedure the cylindrical moulds supplied with the PHI-10 shear device are used to fix the shearing plane into a prescribed orientation using a weak concrete. First, the lower mould (with the lateral key and retaining screws) and two acrylic side plates were thoroughly cleaned to ensure that no debris from previous moulding operations were present. Next, the side plates are attached by sliding them over four fastening screws located on each corner of the mould and then tightening the fastening screws. The thoroughly cleaned retaining screws located on the underside of the lower mould set are then extended completely. Finally, paying special attention to the retaining screws, all interior surfaces of the mould set were coated with oil to prevent the concrete from bonding with the mould.

The next step in the moulding process was to prepare and pour the concrete in the lower half of the mould set. First approximately four cups of Portland Type I Cement were added to a small plastic bucket. Next, an equal amount of Quickcrete sand and small limestone aggregate was added to the bucket. Water was then added while stirring the mixture with a small trowel until a pourable yet thick consistency was obtained. The mixture was then poured into the lower half of the mould set to a level just below the upper lip of the lower mold. This allows for the displacement of concrete due to the insertion of the sample. The sample was then slowly and carefully lowered into position making sure that the lower edge of the locating clamp was in contact with the upper lip of the lower mold. Care was taken to ensure the sample was centered in the mold and the shear plane was not in danger of being contaminated by the concrete. If the cement was thick then a small bulge would form around the sample during insertion into the concrete. A simple shaking of the mould set containing the sample and concrete was sufficient to distribute the bulge.

While the lower half of the molded sample was allowed to set (approximately six hours) the upper mould set could be prepared. This involved thoroughly cleaning the upper mould set of any debris and coating the surface of the mould with oil. After the concrete of the lower mould set had hardened sufficiently for the retaining screws to hold the molded sample in place the acrylic side plates could be removed. The side plates were then cleaned, coated with oil, and attached to the upper mould set using the fastening screws. Any concrete that had hardened to the side of the lower mould set during the curing time was also removed. The concrete was prepared, poured and the sample inserted in the same manner as with lower mould. The fastening screws on the lower mold, inverted over the upper mould, were tightened thus securing the upper mould to the lower mold. The entire upper and lower mould were left in this position and allowed to cure for at least seventy-two hours. Figure 36 shows the final molded arrangement.

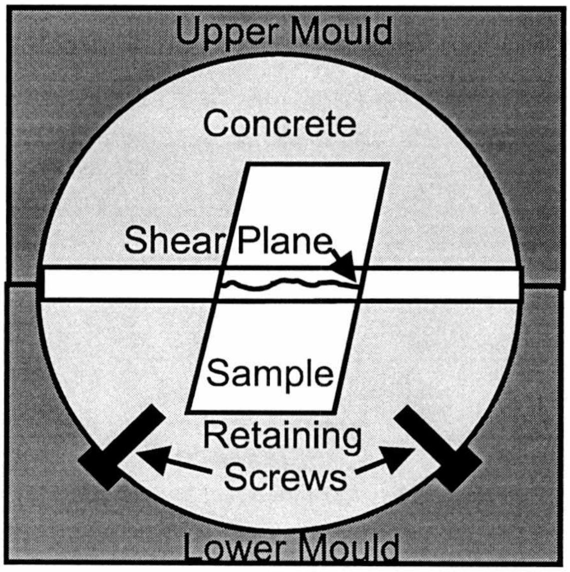

Figure 36 - Final molded arrangement.

The time involved in the molding process can be shortened by replacing part or all of the Portland Cement with White Hydrocal Gypsum Cement available locally from the A. G. Heins Company. When an equal ratio of Portland Cement and Hydrocal was used, curing times were reduced by eighty percent. However, care must be taken when using Hydrocal cement to ensure that the water to cement ratio is high enough to prevent flash curing. The Portland Cement/Hydrocal mix was used with some of the samples from the Foothills Parkway and all samples from the US19E project.

Digitizing Procedure

The samples were ready to be digitized after the molding operation was completed. In this manner, the samples' surfaces would be profiled in the orientation in which they would later be tested. The first step was to use a hacksaw or a pair of wire cutters to sever the wires used in binding the upper half to the discontinuity to the lower half. The lower portion of the sample was then fixed in the lower mold set by tightening the retaining screws. Note that only the lower portion of the sample was profiled. Digitizing the lower half of the sample was consistent with published studies and related to the fact that the upper half of the sample was free to move over the lower half when tested (Nicholson, 1983, Kulatilake et al., 1995).

The digital roughness gage jig was then fixed to the lower mold by positioning the four cutouts on the jig over the metallic posts on the lower mold. A standard engineering scale was placed across the jig in close proximity to the discontinuity surface. The concrete surface of the lower sample was then scored at one centimeter increments corresponding to points where profiles were to be taken. The stabilizing bars attached to the base of the digital roughness gage were then placed in the aluminum channels on the jig. The gage stylus was positioned so the zero x coordinate corresponded to the left edge of the discontinuity surface. The BASIC program, DRG, was then started and the first set (x,z) of coordinates taken. Next, the stylus was repositioned to the right one unit (as read from the BASIC program) and that set of coordinates taken. This process was repeated until the rightmost point of the discontinuity was digitized. The gage was then repositioned to the location where the next z coordinate was to be taken and the digitizing process repeated. When all of the profiles had been digitized the gage, jig and sample were removed from the lower mold set.

Shear Testing Procedure

Before molding and testing, the test conditions had to be determined. The first step involved the determination of the surface area of the plane to be sheared. For the samples obtained from the vertical boreholes at the Foothills Parkway Project, this involved the estimation of the angle of dip of the discontinuity as measured from a horizontal plane normal to the direction of coring. The core was placed along a standard engineering scale resting on a piece of engineering paper. A line was then drawn along the edge of the scale in contact with the sample which indicated the orientation of the core wall. A thin plastic piece of plexiglass was then placed in direct contact with the surface of the discontinuity and a line drawn along the edge of the plexiglass. The angle of dip, ψ was then measured by a protractor as shown in figure 37. The cross-sectional area of the sample was then calculated

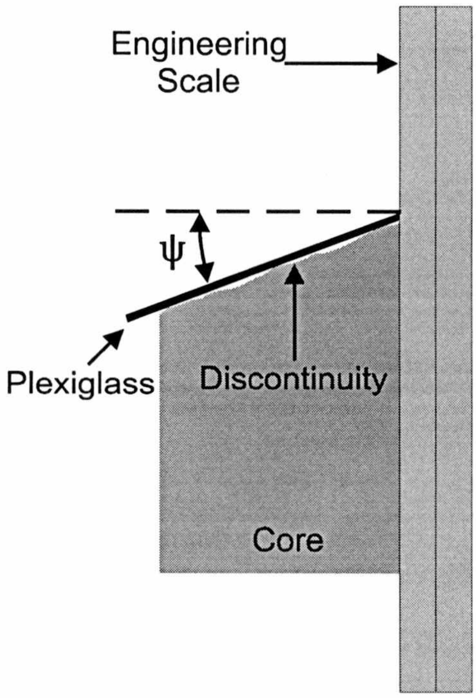

Figure 37 - Method of determining the angle of dip, ψ.

and modified to account for the angle of dip by:

$$A' = \frac{\pi r^2}{\cos\psi} \tag{28}$$

where r is the radius of the core, ψ is the angle of dip, and A' the area of the discontinuity surface. This procedure was not necessary for the US19E Project samples as the area of the shear plane was measured directly using the engineering scale.

The next step in the shear testing procedure was to determine the fluid and pneumatic pressures required to operate the PHI-10 shear machine. The normal piston area for the PHI-10 was stated in the PHI-10 instruction manual as 0.002026 meters square. The level of normal stress, σ_n, required on the joint was then converted to the correct normal fluid pressure to be read on the PHI-10 normal loading system gage by:

$$P = \frac{\sigma_n A'}{0.002026} \tag{29}$$

where P is the required fluid pressure in kPa, σ_n is the required normal pressure in kPa, and A' is the area of the shear plane in m^2. The pneumatic pressure in the pressure maintainer was set according to table 3 in the PHI-10 instruction manual. The pneumatic pressure shown in the manual was related to the fluid pressure in the hydraulic piston.

After the calculations had been made and recorded on a data sheet developed for the PHI-10 device (shown as appendix F) the test was started. The first step was to remove the spherical seat plate, roller carriage, and upper shear box section from the PHI-10. The lower box section was then cleaned with a small brush to ensure no debris was present from previous tests. The lower half of the sample, having already been separated from the upper half during the digitizing process, was then inserted into the lower shear box. The sample was then tapped with a hammer so as to ensure a good fit in the lower shear box. Also during this step the valve corresponding to the desired shearing direction was fully opened. Next, the upper half of the sample was inserted so that the upper and lower halves of the discontinuity were correctly mated. The upper shear box was then placed over the upper sample. To accomplish this correctly, the lower edge of the upper shear box was held and gently fitted over the upper sample. The alignment was then checked to verify that the upper edge of the sample and lower edge of the upper shear box were parallel. The roller carriage and spherical seat plate were then inserted into position.

Using a standard bicycle pump, the pneumatic reservoir of the pressure maintainer was inflated to the correct pressure. The pressure in the maintainer could be read from a small gage attached to the pressure maintainer. Note that this step must be carried out with no fluid pressure in the normal loading system. The normal loading ram was then held in position over the spherical seat plate and the normal load applied. The Enerpac ram was pumped until the correct normal fluid pressure was read from the normal pressure gage. The extensiometer and shear gage follower needle were then zeroed and the shear ram brought into contact with the spherical seat yoke attached to the jointed arm on the upper shear box.

All subsequent testing procedures are provided as a summary of the guidelines found in *Suggested Methods for Determining Shear Strength* (ISRM, 1974). The samples were allowed to stabilize for a period of ten minutes. This was not for the dissipation of excess pore water pressures as all samples were tested at an air dry state. The stabilization period was necessary so that any elastic deformation or redistribution of normal stresses would stabilize.

After the stabilization period, the test could begin. The lever of the shear hydraulic pump was moved at a steady rate until the first 0.2 mm of shear displacement had occurred. Shearing was then stopped and the values of shear and normal loadings recorded. Note that the normal load remained constant as a rule but should be checked and recorded after every load application. Shearing was then continued in 0.2 mm increments until failure occurred. Here failure was defined by the samples' inability to maintain the current level of shear stress. This was readily evident as the follower needle provided the maximum level of shear stress that had occurred during the test.

Point Load Testing Procedure

The point load test was designed for use with 50 mm diameter cores. Since the samples from the Foothills Parkway Project were 50 mm diameter cores, trimming prior to testing was simple. The cores had to be trimmed such that the length, *L*, extending past the platen contact points was greater that one-half the core diameter, *D*, as shown in figure 38.

After the cores were trimmed the pressure gage attached to the point loading machine was zeroed. The core was then inserted into the point load machine and the platens brought into contact with the core wall. Care was taken to ensure that the platens were centered on the core and at least one-half of a core diameter extended from each side of the platens. The platen separation distance was read from the graduated scale on the point load machine and

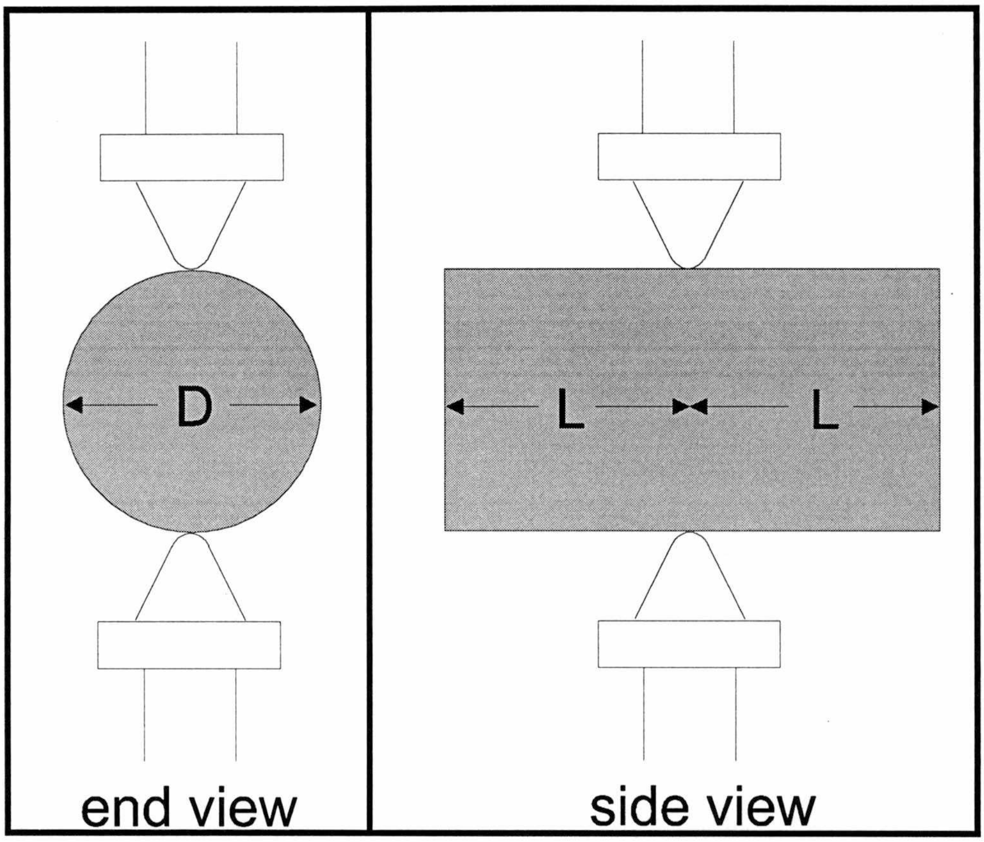

Figure 38 - Proper aspect ratio for rock cores used in the point load test. L is greater than or equal to one-half D (ISRM, 1985).

recorded on a data sheet prepared especially for the point load test (shown as appendix G). A protective blast shield was then fitted over the top of the loading frame to prevent injuries caused by flying rock fragments. The load was then steadily applied through the hydraulic jack such that failure occurred within ten to sixty seconds. The load at failure was read from the follower needle on the pressure gage. The sample was then examined to ensure that the failure plane extended through both platens. If the failure surface passed through only one loading point the test was rejected (ISRM, 1985).

The samples from the US19E Project required more trimming than those from the Foothills Parkway. Samples had to be trimmed into small blocks such as the one shown in figure 39. The dimensions of the samples were then measured and recorded on the data sheet prior to testing. The testing procedure was the same as that for the Foothills Parkway samples.

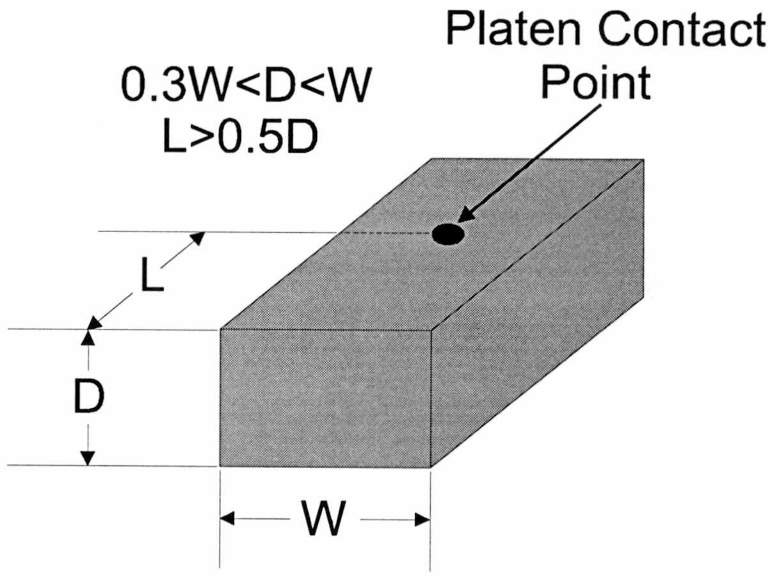

Figure 39 - Correct proportion of rock blocks used in the "lump" type point load test (ISRM, 1985).

CHAPTER 8: INTERPRETATION OF RESULTS

Introduction

Values recorded during testing had to be transformed into parameters that represented the materials. When the material properties were determined they could then be used in the correlation between joint roughness and fractal parameters. JRC values were back-calculated using Barton's shear strength equation using values of shear stress, normal stress, base friction angle, and unconfined compressive strength values obtained from the testing. The fractal parameters, slope and intercept, were then calculated in the aforementioned spreadsheets.

Shear Tests Results

The values of shear and normal fluid pressures recorded at failure were used to calculate the shear and normal stress on the discontinuity at failure. With the given normal piston area of 0.002026 square meters the normal stress could be calculated as:

$$\sigma_n = \frac{P\ (0.002026)}{A'} \tag{30}$$

where σ_n in the normal stress on the discontinuity at failure in kPa, P is the normal fluid pressure at failure in kPa, and A' is the area of the shear plane in m^2. The shear stress could be calculated in much the same way with the piston area of 0.001443 meters squared given in the PHI-10 instruction manual. The formula used to calculate the shear stress was:

$$\tau = \frac{S\,(0.001443)}{A'} \tag{31}$$

where τ is the shear stress at failure in kPa, S is the shear fluid pressure at failure in kPa, and A' the area of the shear plane in m^2.

The samples from the Foothills Parkway project were tested at two normal stresses; 600 and 1000 kPa. The values of normal stress and sample numbering were related by Jim Sheahan, Chief Geotechnical Engineer at HDR, and are representative of project specifications for the Foothills Parkway project. The results from these test are shown in Table 2 below. In Table 2 and all subsequent tables the following notations have been used to indicate rock type: Conglomerate - Cg, Sandstone - Ss, Slate - Sl, and Shale - Sh. Note that the samples were stage tested at successively higher normal stresses in order to determine Coulomb parameters for the samples. However, since the samples were profiled before testing only the first test represents the discontinuity as profiled.

Samples from the US19E project were tested at a normal stress values of 400, 600 and 800 kPa. The value of 400 kPa was determined by estimating a slope height of 20 meters and a unit weight of 20 kN per cubic meter. The values of shear stress for the tests conducted at 400 kPa normal stress are shown in Table 3. All shear test data are shown in Appendix H.

A series of tests for calculating the base friction angles of the various rock types were also conducted. The base friction angle is the friction angle of the rock without any roughness induced dilation or shearing of asperities. The tests were conducted on sawn discontinuities which meant that no peak shear stress was obtained. After a certain amount

Table 2 - Peak shear and normal stress values for the Foothills Parkway samples.

Sample (Rock Type)	Normal Stress at Failure (kPa)	Shear Stress at Failure (kPa)	Stress Ratio (τ/σ_n)
10-1 (Sl)	965	1065	1.10
10-5b (Sl)	1027	894	0.87
10-8a (Sl)	963	717	0.74
1-1b (Ss)	978	2925	2.99
1-4a (Ss)	1010	3098	3.07
2-2b-10.50 (Ss)	1018	1610	1.58
2-2b-11.80 (Ss)	1027	1885	1.84
4-6a (Ss)	649	1295	2.00
5-4b (Ss)	620	2853	4.60
6-1a (Ss)	618	1019	1.65
7-4a (Ss)	606	755	1.24
3-3a (Cg)	641	2435	3.80
4-4b (Cg)	606	755	1.24
a-8 (Cg)	1008	2348	2.33

Table 3 - Peak shear and normal stress values for the US19E samples.

Sample (Rock Type)	Normal Stress at Failure (kPa)	Shear Stress at Failure (kPa)	Stress Ratio (τ/σ_n)
US-1 (Sh)	392	437	1.11
US-2 (Sh)	410	587	1.43
US-3 (Sh)	392	559	1.43
US-4 (Sh)	392	497	1.27
US-5 (Sh)	402	474	1.18
US-6 (Sh)	397	370	0.93
US-7 (Sh)	391	541	1.38
US-8 (Sh)	384	422	1.10
US-9 (Sh)	394	374	0.95
US-10 (Sh)	399	383	0.96
US-11 (Sh)	391	765	1.96
US-12 (Sh)	414	337	0.81
US-13 (Sh)	387	447	1.16
US-14 (Sh)	392	359	0.92
US-15 (Sh)	393	447	1.14
US-16 (Sh)	401	455	1.13
US-17 (Sh)	399	567	1.42
US-18 (Sh)	405	493	1.22
US-19 (Sh)	402	376	0.94
US-20 (Sh)	377	358	0.95

of shearing the shear stress held constant for any additional shear displacement. These tests were conducted at three values of normal stress for each sample. The peak shear and normal stresses were calculated using the same equations presented above. The values of peak shear stress and normal stress for each sample were then entered into a *Borland Quattro Pro version 5.0* spreadsheet and a linear regression performed. The base friction angle, ϕ_b, was then reported as the inverse tangent of the slope of the line obtained from the linear regression. The each of the samples was tested at three values of normal stress to determine the Mohr-Coulomb failure envelope. Due to the highly diverse nature of the samples obtained from the Foothills Parkway project, tests were conducted on each sample. Two tests were conducted on the Sevier Shale from the US19E project. The results of these tests are shown in Tables 4 and 5. All test data are shown in Appendix I.

Point Load Tests Results

The samples from the Foothills Parkway project were well suited to point load testing. Since the test was designed for 50 mm diameter cores, the normalized 50 mm diameter core point load strength, $I_{S(50)}$, could be calculated from:

$$I_{S(50)} = \frac{P}{D_e^2} \tag{32}$$

where P is the gage pressure read from the point load machine at failure in kPa, and D_e is the core diameter in mm (ISRM, 1985). Mean values of $I_{S(50)}$ determined from point load testing for the Foothills Parkway samples are shown in Table 6.

Table 4 - Base friction angles for the Foothills Parkway samples.

Sample (Rock Type)	Base Friction Angle (degrees)
10-1 (Sl)	20
10-5b (Sl)	23
10-8a (Sl)	19
1-1b (Ss)	30
1-4a (Ss)	37
2-2b-10.50 (Ss)	28
2-2b-11.80 (Ss)	27
4-6a (Ss)	28
5-4b (Ss)	33
6-1a (Ss)	23
7-4a (Ss)	27
3-3a (Cg)	36
4-4b (Cg)	32
a-8 (Cg)	29

Table 5 - Base friction angles for the US19E samples.

Sample (Rock Type)	Base Friction Angle (degrees)
USBFA-1 (Sh)	22
USBFA-2 (Sh)	24

Table 6 - Point load indices for the Foothills Parkway samples.

Sample (Rock Type)	Mean $I_{S(50)}$ (MPa)
10-1 (Sl)	0.9
10-5b (Sl)	0.8
10-8a (Sl)	0.4
1-1b (Ss)	3.1
1-4a (Ss)	1.3
2-2b-10.50 (Ss)	0.6
2-2b-11.80 (Ss)	3.0
4-6a (Ss)	1.2
5-4b (Ss)	1.2
6-1a (Ss)	1.7
7-4a (Ss)	0.4
3-3a (Cg)	0.4
4-4b (Cg)	1.0
a-8 (Cg)	2.4

Standard ISRM testing guidelines required that ten tests be conducted for all samples (ISRM, 1985). Not enough core was received to meet this requirement for all samples. Samples marked with an asterisk (*) in the table above are those that did not meet the standard ISRM testing requirement regarding number of tests. All samples were tested parallel to planes of weakness which corresponded to the direction in which they were sheared, as shown in figure 40.

The specially prepared samples from the US19E project were tested according to block testing procedures. Since the samples were not 50 mm diameter cores, special procedures had to be used to determine the $I_{S(50)}$ value. First the uncorrected point load strength, I_S, was calculated by:

$$I_S = \frac{P}{(4A/\pi)} \tag{33}$$

where P was the gage pressure at failure in kPa and A was the minimum cross-sectional area of the block in mm^2. A size correction factor, F, was then calculated according to:

$$F = \left(\frac{D_e}{50}\right)^{0.45} \tag{34}$$

where D_e was the square root of the minimum cross-sectional area of each block in mm (ISRM, 1985). The uncorrected point load strength was then multiplied by the size correction factor to obtain the correct $I_{S(50)}$ value for each block tested. The average of the $I_{S(50)}$ values for the ninety-one tests conducted was 1.4 MPa. All point load tests were conducted parallel

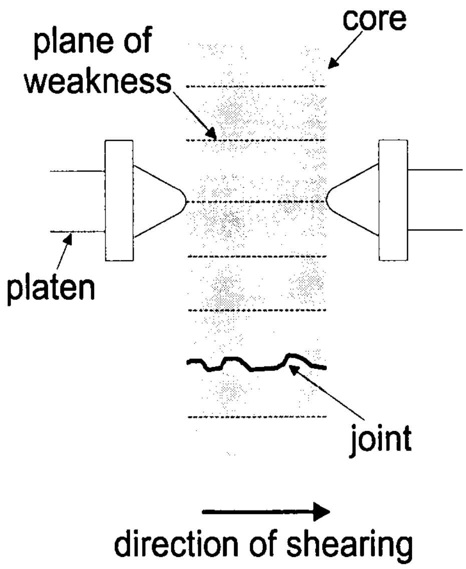

Figure 40 - Diagram showing how samples were point load tested parallel to planes of weakness.

to planes of weakness (Fig. 40), corresponding to the direction of shearing.

The $I_{S(50)}$ value has been shown to be related to unconfined compressive strength by the following relationship:

$$\sigma_c = I_{S(50)}(24) \tag{35}$$

(ISRM, 1985). The relationship was used for relating all point load values to unconfined compressive strengths. All point load test data are shown in Appendix J.

Calculation of JRC Values

The values of normal stress, shear stress, unconfined compressive strength, and base friction angle were used to predict the JRC values according to:

$$JRC = \frac{\tan^{-1}(\tau/\sigma_n) - \phi_b}{\log_{10}(\sigma_c/\sigma_n)} \qquad \textbf{(36)}$$

where τ is the peak shear strength, σ_n is the normal stress, ϕ_b is the base friction angle, and σ_c the unconfined compressive strength. Table 7 shows the JRC values for the Foothills Parkway samples while Table 8 shows the JRC values for the US19E project samples.

Fractal Parameters

Since the BASIC program used to read data from the roughness gage reads in absolute units, the data must be converted into physical units of measure. The gage was calibrated using a one-half inch calibration block obtained from Geotechnical and Materials Laboratory Supervisor, Curtis Allin. The results of the calibration revealed that the gage had a horizontal resolution of 0.77 mm/absolute unit and a vertical resolution of 0.10 mm/absolute unit. The comma-delimited ASCII files were then read into a *Microsoft Excel version 7.0* spreadsheet. Each file was checked to ensure that no duplication of points had occurred during the digitizing process. The absolute units were then changed to physical units and the file saved as an *Excel 7.0* file.

The files for each sample's profiles were then input into the spreadsheets used in calculating the fractal parameters. The spreadsheet templates for the variogram and *WAM* methods were described in Chapter 4 and are shown as Appendix D and E. Since each profile was of a different length as demonstrated in figure 41, the fractal parameters were normalized using the following relationships:

Table 7 - JRC values for the Foothills Parkway samples

Sample (Rock Type)	JRC
10-1 (Sl)	28.9
10-5b (Sl)	14.2
10-8a (Sl)	17.7
1-1b (Ss)	22.1
1-4a (Ss)	23.5
2-2b-10.50 (Ss)	25.8
2-2b-11.80 (Ss)	18.6
4-6a (Ss)	21.5
5-4b (Ss)	26.8
6-1a (Ss)	19.7
7-4a (Ss)	20.7
3-3a (Cg)	33.4
4-4b (Cg)	12.1
a-8 (Cg)	21.9

Table 8 - JRC values for the US19E samples.

Sample (Rock Type)	JRC
US-1 (Sh)	12.7
US-2 (Sh)	16.5
US-3 (Sh)	16.3
US-4 (Sh)	14.6
US-5 (Sh)	13.6
US-6 (Sh)	10.1
US-7 (Sh)	15.8
US-8 (Sh)	12.5
US-9 (Sh)	10.4
US-10 (Sh)	10.6
US-11 (Sh)	20.4
US-12 (Sh)	8.2
US-13 (Sh)	19.7
US-14 (Sh)	9.8
US-15 (Sh)	13
US-16 (Sh)	13.1
US-17 (Sh)	16.3
US-18 (Sh)	14.1
US-19 (Sh)	10.2
US-20 (Sh)	10.3

$$D_n = \frac{\sum_{j=1}^{j} D_j L_j}{\sum_{j=1}^{j} L_j} \quad \textbf{(37)}$$

and

$$b_{n,\log} = \frac{\sum_{j=1}^{j} b_{j,\log} L_j}{\sum_{j=1}^{j} L_j} \quad \textbf{(38)}$$

where D_n is the normalized fractal dimension, D_j is the fractal dimension of the *j*th profile, L_j is the length of the *j*th profile, $b_{n,log}$ is the normalized fractal intercept in log form, and $b_{j,log}$ is the fractal intercept of the *j*th profile in log form. The fractal parameters from the

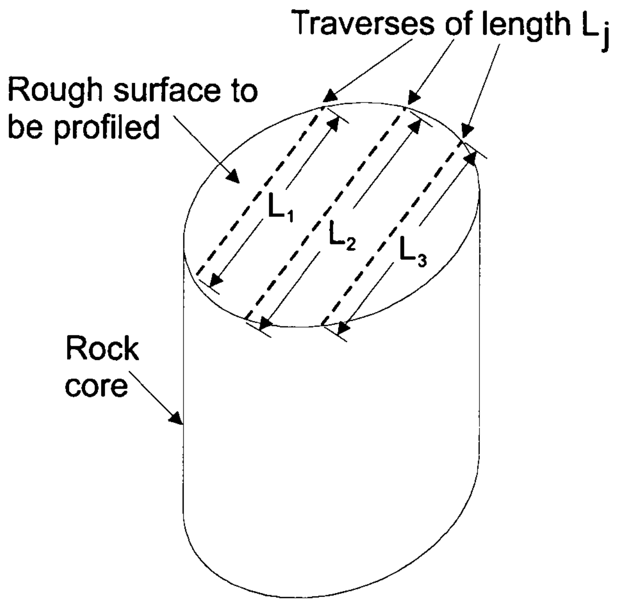

Figure 41 - Shear test sample with traverses of various lengths, L_j.

variogram method for the samples of the Foothills Parkway project are shown in Table 9. The fractal intercept for all tables has been converted from its log form by:

$$b_n = 10^{b_{n\log}}. \qquad \textbf{(39)}$$

The fractal parameters from the *WAM* method for the Foothills Parkway project samples are shown in Table 10. The same process was repeated for the samples from the US19E project. The normalized fractal parameters from the variogram and *WAM* methods are shown in Tables 11 and 12, respectively.

Table 9 - Fractal parameters from the variogram method for Foothills Parkway samples.

Sample (Rock Type)	Normalized Fractal Dimension (D_n)	Normalized Fractal Intercept (b_n)
10-1 (Sl)	1.18	0.0322
10-5b (Sl)	1.31	0.0084
10-8a (Sl)	1.28	0.0198
1-1b (Ss)	1.22	0.0292
1-4a (Ss)	1.39	0.0313
2-2b-10.5 (Ss)	1.27	0.0430
2-2b-11.8 (Ss)	1.31	0.0151
4-6a (Ss)	1.27	0.0187
5-4b (Ss)	1.35	0.0485
6-1a (Ss)	1.31	0.0123
7-4a (Ss)	1.34	0.0468
3-3a (Cg)	1.25	0.0635
4-4b (Cg)	1.32	0.0255
a-8 (Cg)	1.28	0.0175

Table 10 - Fractal parameters from the *WAM* method for Foothills Parkway samples.

Sample (Rock Type)	Normalized Fractal Dimension (D_n)	Normalized Fractal Intercept (b_n)
10-1 (Sl)	1.06	10.34
10-5b (Sl)	1.19	4.99
10-8a (Sl)	1.18	7.25
1-1b (Ss)	1.11	9.81
1-4a (Ss)	1.31	10.66
2-2b-10.5 (Ss)	1.17	11.72
2-2b-11.8 (Ss)	1.20	7.09
4-6a (Ss)	1.15	7.52
5-4b (Ss)	1.22	12.94
6-1a (Ss)	1.11	6.04
7-4a (Ss)	1.23	11.69
3-3a (Cg)	1.17	14.82
4-4b (Cg)	1.18	9.10
a-8 (Cg)	1.19	7.84

Table 11 - Fractal parameters from the variogram method for US19E samples.

Sample (Rock Type)	Normalized Fractal Dimension (D_n)	Normalized Fractal Intercept (b_n)
US-1 (Sh)	1.30	0.0107
US-2 (Sh)	1.33	0.0245
US-3 (Sh)	1.31	0.0100
US-4 (Sh)	1.30	0.0126
US-5 (Sh)	1.28	0.0093
US-6 (Sh)	1.40	0.0063
US-7 (Sh)	1.18	0.0138
US-8 (Sh)	1.33	0.0054
US-9 (Sh)	1.34	0.0042
US-10 (Sh)	1.35	0.0091
US-11 (Sh)	1.36	0.0120
US-12 (Sh)	1.40	0.0072
US-13 (Sh)	1.21	0.0257
US-14 (Sh)	1.29	0.0085
US-15 (Sh)	1.33	0.0069
US-16 (Sh)	1.27	0.0138
US-17 (Sh)	1.30	0.0126
US-18 (Sh)	1.35	0.0072
US-19 (Sh)	1.35	0.0093
US-20 (Sh)	1.38	0.0047

Table 12 - Fractal parameters from the *WAM* method for US19E samples

Sample (Rock Type)	Normalized Fractal Dimension (D_n)	Normalized Fractal Intercept (b_n)
US-1 (Sh)	1.18	5.62
US-2 (Sh)	1.16	7.76
US-3 (Sh)	1.21	5.62
US-4 (Sh)	1.21	6.17
US-5 (Sh)	1.15	4.57
US-6 (Sh)	1.26	4.17
US-7 (Sh)	1.08	6.92
US-8 (Sh)	1.17	3.55
US-9 (Sh)	1.20	3.39
US-10 (Sh)	1.22	4.68
US-11 (Sh)	1.22	8.20
US-12 (Sh)	1.26	3.98
US-13 (Sh)	1.08	8.13
US-14 (Sh)	1.15	4.79
US-15 (Sh)	1.18	4.07
US-16 (Sh)	1.12	6.17
US-17 (Sh)	1.16	5.89
US-18 (Sh)	1.16	4.07
US-19 (Sh)	1.23	4.79
US-20 (Sh)	1.19	3.24

CHAPTER 9: CORRELATIONS

Introduction

The Joint Roughness Coefficient values back-calculated from the experimental laboratory results should be related to some fractal parameter. Two parameters were obtained from the fractal methods: slope and intercept. The slope of the fractal log-log plot has been shown as related to the way in which roughness varies with scale. The slope of the fractal log-log plot yields the magnitude of roughness. Here, the parameters from the variogram and *WAM* methods will be related to the Joint Roughness Coefficient values.

Correlation Between Methods

The Joint Roughness Coefficient values and normalized fractal parameters from both methods were entered into a *Microsoft Excel version 7.0* spreadsheet. The first step was to perform a regression between the normalized fractal dimensions for the Foothills Parkway samples from both methods. The regression yielded a multiple R of 0.8658 with a standard deviation of 0.0281. The same was done for the normalized fractal dimensions obtained from the US19E samples which yielded a multiple R 0.8813 with a standard deviation of 0.0271.

The sample procedure was undertaken to determine the degree of similarity between the normalized fractal intercepts from both methods. The normalized fractal intercepts obtained from the variogram and *WAM* methods were input into the spreadsheet and a regression performed which yielded a multiple R of 0.9827 with a standard deviation of 0.0031. The same was done for the normalized fractal intercepts for the US19E samples which yielded a multiple R of 0.8737 with a standard deviation of 0.0028.

The correlations between the two methods revealed that the normalized fractal intercept showed less variability between the methods than the normalized fractal dimension. This could be related to the break from a perfect linear slope in the log-log plot seen in all fractal methods. The slope would have been affected to a greater degree by the break than the intercept since the intercept was anchored by the initial linear portion of the plot.

Laboratory JRC Correlation with Fractal Parameters

The same approach used to correlate the two methods was used in generating the correlation between fractal parameters and Joint Roughness Coefficients. First, the normalized fractal dimension obtained from the variogram and *WAM* methods were correlated with the JRC values. The results of the correlation for the Foothills Parkway samples yielded multiple Rs of 0.3635 and 0.1456 with standard deviations of 5.4676 and 5.8066 for the variogram and *WAM* methods, respectively. The same was done for the normalized fractal dimensions from the US19E sample. This gave multiple Rs of 0.5069 and 0.4774 with standard deviations of 2.9581 and 3.0153 for the variogram and *WAM* methods, respectively.

The normalized fractal intercepts were then checked to see how they correlated with the joint roughness coefficients. For the samples from the Foothills Parkway this yielded multiple Rs of 0.7416 and 0.7617 with standard deviations of 3.9374 and 3.8029 for the variogram and *WAM* methods, respectively. The correlation between JRC and normalized fractal intercept for the US19E samples yielded multiple Rs of 0.6894 and 0.8322 with standard deviations of 2.4860 and 1.9028 for the variogram and *WAM* methods, respectively.

The results of these correlations showed exactly what was expected. The normalized intercept was more closely correlated with the JRC values back-calculated from the laboratory data than the normalized fractal dimensions. This was expected as the normalized intercept yields the magnitude of roughness which was the controlling factor that governed shear strength with all other parameters accounted. Furthermore, the *WAM* method produced fractal intercepts that were more closely related to the JRC values than the variogram method when linear statistical measures were used. The results of these correlations are thought to provide proof that the normalized fractal intercept is correlated with the JRC values back-calculated from shear tests.

Analysis of the Standard Joint Roughness Profiles

As another correlation, the fractal dimensions and intercepts of the standard JRC profiles were analyzed. The standard profiles were first digitized at a resolution corresponding to that of the digital roughness gage. This was done in order to eliminate ambiguities associated with differing horizontal resolutions discussed in Chapter 4. The fractal parameters for the variogram and *WAM* methods were then calculated.

Figure 42 shows a plot of the fractal dimensions versus the joint roughness coefficients representing the standard joint roughness profiles. As can be seen, the fractal dimensions for both methods are somewhat similar. The fractal dimensions tend to be larger for the smoother profiles than the rougher profiles. Fractal dimensions obtained from the *WAM* method tend to be less than those for the variogram method. Again no

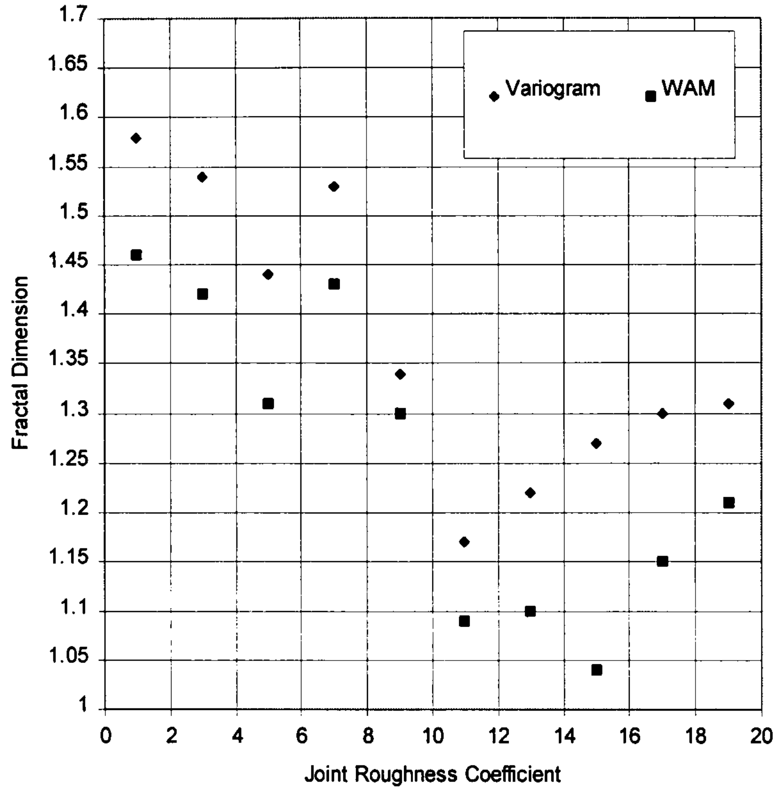

Figure 42 - Fractal dimension versus standard profile JRC.

significant correlation between joint roughness coefficient and fractal dimension was obtained.

Fractal intercepts, b_n obtained from the fractal analysis of the standard JRC profiles showed a stronger correlation with joint roughness coefficients. Figure 43 shows the results obtained from the variogram method analysis. The results do not lend themselves to a linear fit, however a logarithmic equation fit the data quite well. The line in the figure corresponds to a logarithmic regression which yielded the equation:

$$JRC = (6.8)\ln(b_n) + 32.2 \qquad \textbf{(40)}$$

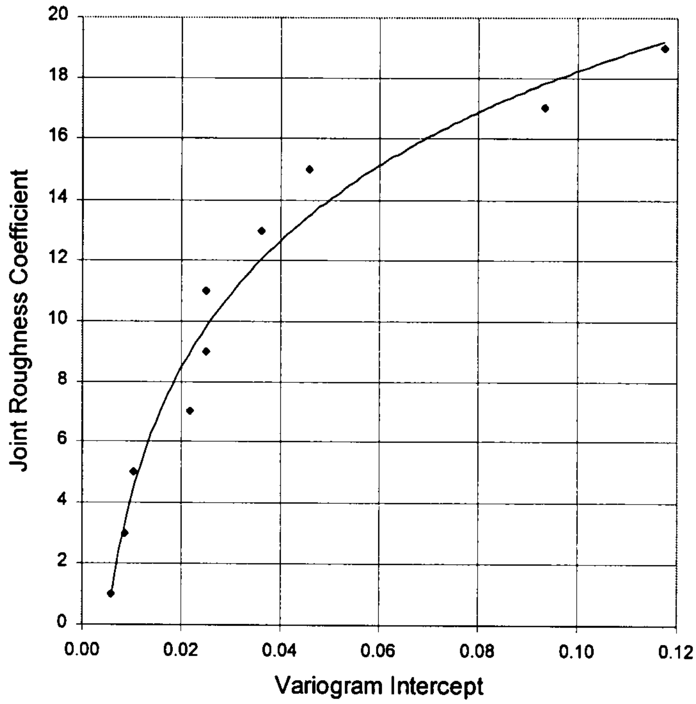

Figure 43 - Standard profile JRC versus variogram intercept.

with an R^2 of 0.9687. The logarithmic trend of the results may have been responsible for the lower standard error of estimates (R) obtained from the back-calculated JRC values discussed earlier.

The same method was applied to the normalized intercepts obtained from the *WAM* method. The results are shown in figure 44. Data followed a linear trend shown by the line in the figure given by the equation:

$$JRC = 1.29(b_n) - 2.32 \tag{41}$$

with an R^2 of 0.9032. These results are complementary to those obtained from the JRC values back-calculated from laboratory tests.

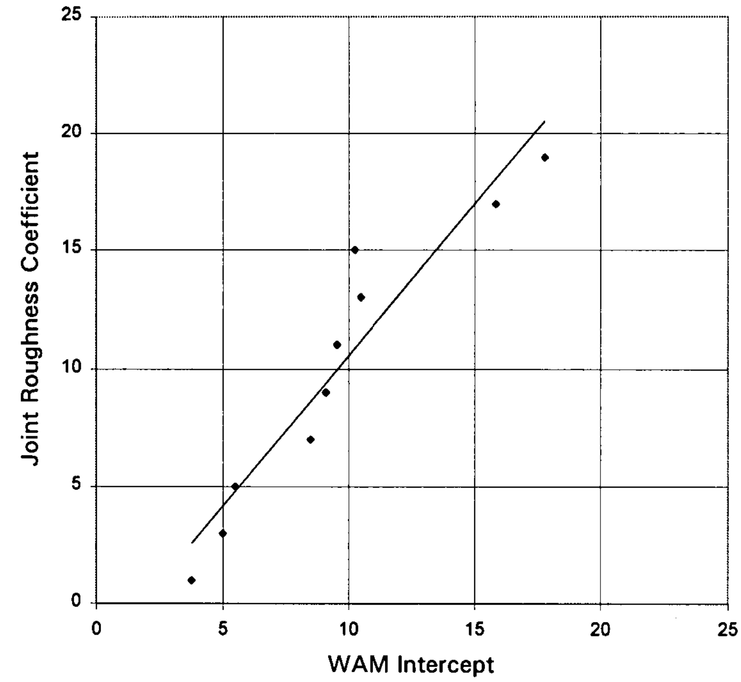

Figure 44 - Standard profile JRC versus *WAM* intercept.

Fractal Intercept Based Joint Roughness Coefficient

The correlations between laboratory and standard profile JRCs and the fractal parameters showed the fractal intercept was a better measure for estimating the JRC value of a rock joint. Here all laboratory calculated JRC values will be used to generate a relationship between fractal intercept and the JRC. Relationships for both the variogram and *WAM* methods will be explored.

JRCs back-calculated from laboratory data were plotted versus the normalized fractal intercepts, b_n. The resulting relationship followed a logarithmic curve given by:

$$JRC = (7.24)\ln(b_n) + 47.69 \tag{42}$$

with an R^2 0.7112 . The resulting plot is shown in figure 45.

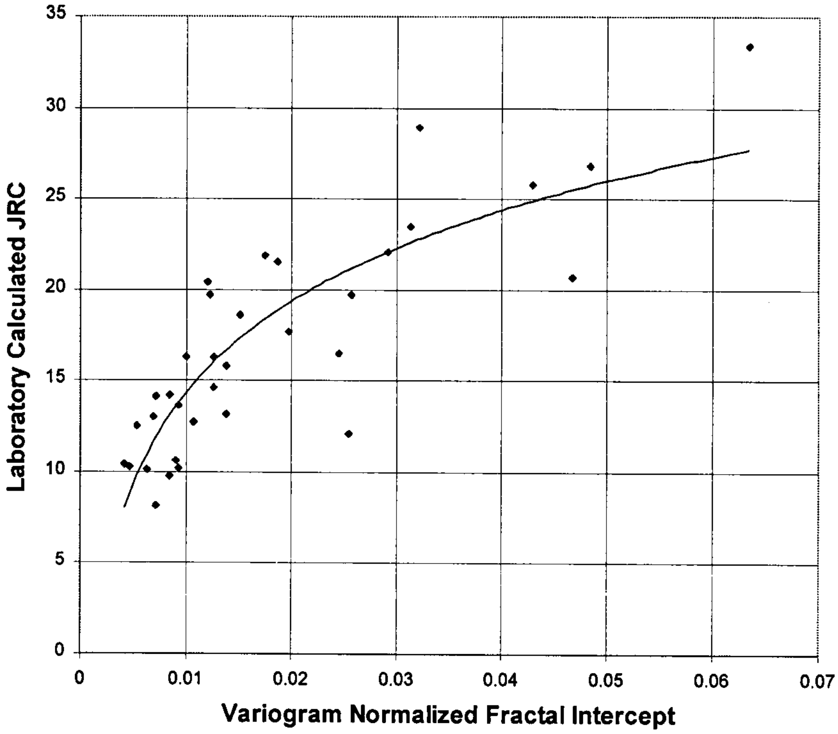

Figure 45 - Laboratory JRC versus variogram intercept.

The data followed the same trend as did the standard profile JRC data, with one exception. The laboratory relationship yielded higher JRC values than the standard profile relationship, for the same fractal intercept. Initially this was thought to have been related to misrepresentation of material properties; however, it was more likely that the conservative nature of Barton's empirical relationship was the explanation. Since the laboratory JRC values were calculated from Barton's equation any conservatism inherent in the equation would manifest itself in the reported JRCs.

The same procedure was used in developing the relationship between fractal intercepts and joint roughness coefficients for the *WAM* method. Figure 46 shows the data

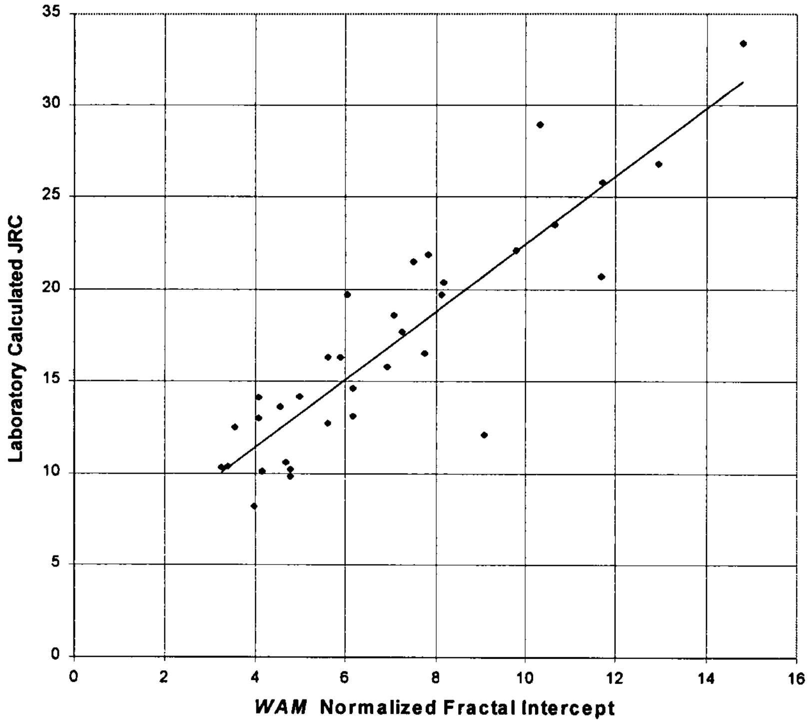

Figure 46 - Laboratory JRC versus *WAM* intercept.

with the resulting regression given by:

$$JRC = 1.83(b_n) + 4.11 \tag{43}$$

which had an R^2 of 0.7911. Again, for the same normalized fractal intercept the joint roughness coefficients predicted by the laboratory relationship were greater than those predicted from the standard profile relationship. This gave further proof that the conservative nature of Barton's equation was responsible for the discrepancy between the relationships developed for laboratory and standard profile joint roughness coefficients.

Fractal Intercept Based Peak Shear Strength Prediction

The equations developed from the correlation of fractal intercepts with laboratory calculated JRCs can be used to estimate the JRC values used in Barton's peak shear strength criterion. The fractal intercept for the discontinuity in question would be determined by either the variogram or *WAM* method and a JRC value determined from equation 42 or 43, respectively. The other parameters necessary to use Barton's equation: level of normal stress, base friction angle and joint compressive strength would then be determined in order to predict the peak shear strength of the discontinuity.

The fractal intercepts from the variogram method for samples of both the Foothills Parkway and US19E projects were substituted into equation 42. This yielded the fractal intercept based joint roughness coefficients. The fractal intercept based JRCs and all other necessary parameters (discussed in Chapter 8) were input into Barton's peak shear strength criterion, which yielded predicted peak shear strengths for the samples. The predicted peak shear strengths were then plotted versus the laboratory measured peak shear strengths (Figure 47). The statistical analysis of the data resulted in an R^2 of 0.9270 with a standard error of 197 kPa.

The same approach was used to evaluate the *WAM* method fractal intercept based joint roughness coefficients. The fractal intercept for each sample was entered into equation 43, which yielded a fractal intercept based joint roughness coefficient for each sample. Barton's peak shear strength criterion was then entered with the fractal intercept based joint roughness coefficients and other necessary parameters to estimate the peak shear strength. The predicted peak shear strengths were then plotted versus the measured peak shear

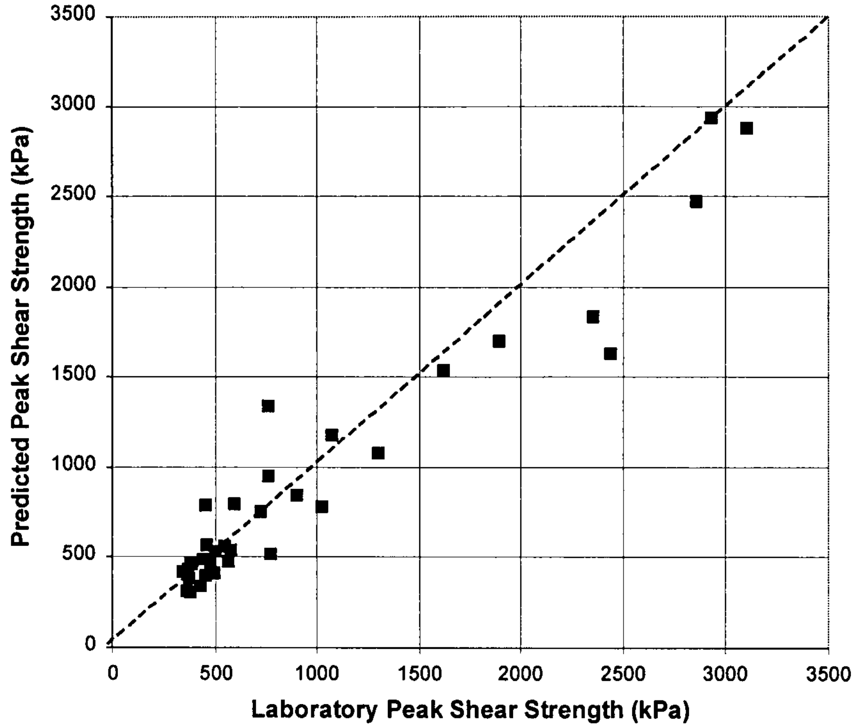

Figure 47 - Plot of predicted peak shear strength versus laboratory peak shear strength. The predicted peak shear strengths were obtained from Barton's equation using fractal intercept based joint roughness coefficients from the variogram method.

strengths (Figure 48). The statistical analysis of the data resulted in an R^2 of 0.9453 with a standard error of 194 kPa.

Both models are thought to be significant improvements over the current method of determining joint roughness coefficients. While much more laboratory analysis should be conducted before a final relationship is established; the procedures and results contained in this study are thought to be the genesis for further studies on the subject. Since the models were developed using experimental data from real rock joints, several factors should be considered. First, experimental error must be considered. Errors are generated by all laboratory experiments. If published test procedures are followed, however, these errors are minimized. Second, both the peak shear strength criteria developed by Barton and the relationship between unconfined compressive strength and the point load index are empirical. For average cases these formulae have been shown to hold true. In some special cases, however the formulae could not be applied correctly. Finally, the models developed from the laboratory JRC data are not conservative. The fractal intercept based joint roughness coefficients would yield the same shear stress as obtained in the direct shear test when used in Barton's peak shear strength criterion. The approach of visually selecting joint roughness coefficients will generally result in a conservative estimate of peak shear strength.

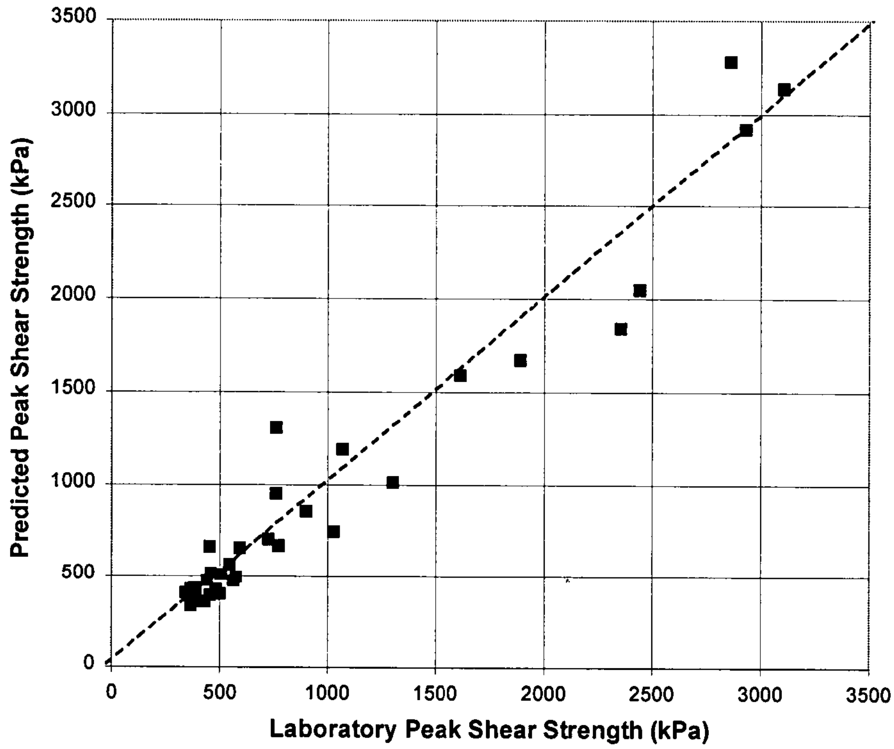

Figure 48 - Plot of predicted peak shear strength versus laboratory peak shear strength. The predicted peak shear strengths were obtained from Barton's equation using fractal intercept based joint roughness coefficients from the *WAM* method.

CHAPTER 10: CONCLUSIONS

The subjective nature of visually estimating Joint Roughness Coefficients leads to the introduction of errors in Barton's peak shear strength criteria. In order to eliminate the uncertainty, a method based upon fractal geometry has been proposed. Fractal geometry was developed to deal with highly complex shapes such as those found in nature.

Several methods for calculating the fractal dimension of rock discontinuities were examined. The *WAM* method was developed as a result of this study. Fractional Brownian motion functions were generated in order to verify each of the methods. The variogram and *WAM* methods were then shown as the most accurate for the calculation of the fractal dimension of the fBm profiles.

A laboratory testing program was then initiated so that JRC values could be back-calculated. The samples used for the laboratory experiments were obtained from two projects; the Foothills Parkway project, and the US Highway 19E project. The Foothills Parkway samples were 50 mm diameter cores of sandstone, conglomerate, and slate. The samples from the US Highway 19E project were square blocks of Sevier Shale. The surfaces of the discontinuities were profiled with a digital roughness gage. The gage consisted of two potentiometers: one vertical and one horizontal. A computer program was written to read data from each of the potentiometers. A jig was also developed to secure the gage in position over the molded samples.

The samples were then tested in direct shear. Samples were sheared in 0.2 mm increments until the peak shear strength was determined. Samples were then sawn and tested in order that the base friction angle of the various rock types could be determined. The remainder of the cores were tested in a point load testing machine. The point load test was then used so that a representative value of the unconfined compressive strength of the rock could be estimated.

The data from the laboratory test were then entered into Barton's equation. From this the JRC values were back-calculated for each sample. JRC values were then compared with the fractal parameters obtained from the profiled samples. The variogram and *WAM* method were used to estimate the fractal parameters. The intercept of the power law plot was then shown as to be more closely correlated with JRC values than the slope. This met with expectations, as the intercept theoretically yields the magnitude of roughness.

The intercept values from the variogram and *WAM* methods were then used to determine relationships with joint roughness coefficients from laboratory results and the standard JRC profiles. Good agreement was found between the experimental and standard profile JRC data and the fractal intercepts of both methods. The equations developed from the correlation of fractal intercepts and laboratory calculated JRCs were then used to estimate peak shear strengths. The fractal intercepts obtained from the *WAM* and variogram methods were used to obtain JRCs which were input into Barton's peak shear strength criterion. The other parameters necessary to predict peak shear strength were input into Barton's equation and predicted peak shear strengths determined for samples of the Foothills Parkway and US19E projects. The results of the fractal intercept based predicted peak shear strengths were then compared with the laboratory measured peak shear strengths. The results of this correlation showed that the fractal intercept is a useful parameter for quantifying joint roughness coefficients to be used in the prediction of peak shear strength.

REFERENCES

REFERENCES

Arwood S.M., "An Energy Model for Rock Slope Stability Analysis." Master's Thesis, Dept. of Civil and Environmental Engineering, University of Tennessee, 1996.

Barton N., "Review of a New Shear Strength Criterion for Rock Joints." *Engineering Geology*, 7, pp. 287-332, 1973.

Barton N.R. and Choubey V., "The Shear Strength of Rock Joints in Theory and Practice." *Rock Mechanics*, 10, pp. 1-54, 1977.

Brown S.R., "Measuring the Dimension of Self-Affine Fractals: The Example of Rough Surfaces." *Geophysical Research Letters*, 15, No. 3, 1992.

Carr J.R., E-mail correspondence, Jul. 16, 1996.

Carr J.R., *Surface Roughness Characterization of Rock Masses Using the Fractal Dimension and the Variogram.* Dept. of the Army, Waterways Experiment Station, Technical Report REMR-GT-14, Vicksburg, Mississippi, 1990.

Carr J.R. and Warriner J.B., "Relationship Between the Fractal Dimension and Joint Roughness Coefficient." *Bull. of the Assoc. of Eng. Geologist*, XXVI(2), pp. 253-263, 1989.

Dight P.M., and Chiu H. K., "Prediction of Shear Behavior of Joints Using Profiles." *Int. Journal for Rock Mech. and Min. Sci. Geomechan. Abstracts.* 15, pp. 303-307, 1981.

Goodman, R.E., *Introduction to Rock Mechanics.* Wiley, New York, 2nded., pp. 164-171, 1989.

Hardeman W. D., Geologic Map of Tennessee. Division of Geology, State of Tennessee, 1966.

Hsiung S.M., Ghosh A., and Chowdhury A.H., "On Natural Rock Joint Profile Characterization Using Self-Affine Fractal Approach." *Rock Mechanics*, 28, pp. 681-687, 1995.

Hsiung S.M., Ahola M.P., Chowdhury A.H., Ghosh A., "Laboratory Characterization of Rock Joints.", Center for Nuclear Waste Regulatory Analyses., Report CNWRA 93-013, San Antonio, TX, 1993.

Hsiung S.M., Ghosh A., Ahola M.P., and Chowdhury A.H., "Assessment of Conventional Methodologies for Joint Roughness Coefficient Determination." *Int. Journal for Rock Mech. and Min. Sci. Geomechan. Abstracts.* 30, pp. 825-829, 1993.

International Society for Rock Mechanics, "Suggested Methods for Determining Point Load Strength.", *Int. Journal for Rock Mech. and Min.Sci.Geomechan.Abstracts.*, 22, pp. 51-60, 1985.

International Society for Rock Mechanics, "Suggested Methods for Determining Shear Strength. " *Commission on Standardization of Laboratory and Field Tests, Doc. No. 1*, Lisboa Codex, Portugal, 1974.

Kulatilake P.H.S.W., Shou G., Huang T.M., Morgan R.M., "New Peak Shear Strength Criteria for Anisotropic Rock Joints." *Int. Journal for Rock Mech. and Min. Sci. Geomechan. Abstracts.* 32, pp. 673-697, 1995.

Lee Y.H., Carr J.R., Barr D.J., and Haas C.J., "The Fractal Dimension as a Measure of the Roughness of Rock Discontinuity Profiles." *Int. Journal for Rock Mech. and Min. Sci. Geomechan. Abstracts.* 27, pp. 453-464, 1990.

Maerz N.H., Franklin J.A., and Bennett C.P., "Joint Roughness Measurement Using Shadow Profiliometry." *Int. Journal for Rock Mech. and Min. Sci. Geomechan. Abstracts.* 27, pp. 329-344, 1990.

Mandelbrot B.B., *The Fractal Geometry of Nature.* W.H. Freeman and Co., New York, 1983.

McWilliams P.C., Kerkering J.C., and Miller S.M., "*Estimation of Shear Strength Using Fractals as a Measure of Rock Fracture Roughness.*" US Bureau of Mines, Report RI-9447, 1993.

Miller S.M., McWilliam, P.C., Kerkering J.C., "Evaluation of stereo digitizing rock fracture roughness." *Rock Mechanics as a Guide for Efficient Utilization of Natural Resources*, A.W. Hair, ed., Balkema, Totterdam, pp. 201-210, 1989.

Nicholson G.A., *In-Situ and Laboratory Shear Devices for Rock: A Comparison.* Dept. of the Army, Waterways Experiment Station, Technical Report GL-83-14, Vicksburg, Mississippi,1983.

Odling N.E., "Natural Fracture Profiles, Fractal Dimension and Joint Roughness Coefficients." *Rock Mechanics*, 27, pp. 135-153, 1994.

Patton F. D., "Multiple Modes of Shear Failure in Rock." *Proceedings 1st Congr. Int. Soc. Rock Mech.*, Lisbon, pp. 503-524, 1966.

Power W.L. and Tullis T.E., “Euclidean and Fractal Models for the Description of Rock Surface Roughness.” *Journal of Geophysical Research.*, 96, pp. 415-424, 1991.

Reeves M.J., “Rock Surface Roughness and Frictional Strength.” *Int. Journal for Rock Mech. and Min. Sci. Geomechan. Abstracts.* 22, pp. 429-442, 1990.

Russ J.C., *Fractal Surfaces.*, Plenum Press, New York, 1994.

Tse R. and Cruden D.M., “Estimating Joint Roughness Coefficients.” *Int. Journal for Rock Mech. and Min. Sci. Geomechan. Abstracts.* 15, pp. 303-307, 1978.

Wakabayashi N. and Fukushige I., “Experimental Study on the Relation Between Fractal Dimension and Shear Strength.”, *Proceedings Conf. Fractured and Jointed Rock Masses,* A.A. Balkema, Rotterdam, 1995.

Wu T.H. and Ali E.M., “Statistical Representation of the Joint Roughness.” *Int. Journal for Rock Mech. and Min. Sci. Geomechan. Abstracts.* 15, pp. 259-262, 1978.

APPENDICES

APPENDIX A

Modified Divider Method Computer Program

```
C PROGRAM FRACTAL FORTRAN
C   this program was received from Dr. James Carr
c  at the University of Nevada Reno to replace
c  the faulty program found in the US Army Corps of
c  Engineers Technical Report  REMR-GT-14.
c  ************************************************
c
c  USERS GUIDE
c
c  FREE FORMAT TYPE INPUT
c
c  Card 1   K - # of step sizes
c  Card 2   length of each step size (1., 2., etc.)
c  Card 3   X.,Y. coordinates (new card for each set)
C
C
C  *************************************************
     DIMENSION X(1000), Y(1000), S(100), N(100)
     REAL N, LN
c     OPEN (5, FILE = ' ')
c     above was open din;t seem to like
     READ (5,*) K
     READ (5,*) (S(JK), JK = 1,K)
     II = 0
10   CONTINUE
     READ  (5,*,END=20) DUM1, DUM2
     II = II + 1
     X(II) = DUM 1
     Y(II) = DUM 2
     GO TO 10
20   CONTINUE
     DO 100 JJ = 1,K
     R = S(JJ)
     XC = X(1)
     YC = Y(1)
     LN = 0
     J = 2
     DO 50 I = J, II
```

```
      DX = XC -X(I)
      DY = YC - Y(I)
      DIST = SQRT(DX * DX + DY * DY)
      IF (DIST .GE. R) THEN
      LN = LN + 1
      M = I -1
      R1 = SQRT((XC - X(M))**2 + (YC - Y(M))**2)
      R2 = DIST
      Z = ABS((R2 - R) / (R2 - R1))
      EX = X(I) - X(M)
      EY = Y(I) - Y(M)
      HYP = SQRT(EX * EX + EY * EY)
      HSIN = EY/HYP
      HCOS = EX/HYP
      CALL ITER (R, XC, YC, HSIN, HCOS, HYP, X(M), Y(M))
      ENDIF
50    CONTINUE
      DR = SQRT((XC - X(II))**2 + (YC - Y(II))**2)
      LN = LN + DR/R
      N(JJ) = LN
100   CONTINUE
      DO 200 I = 1, K
      WRITE (*,210) S(I), N(I)
200   CONTINUE
210   FORMAT (5X, 'Y = ', F10.3,  ' N = ', F10.3)
      DUM1 = 0.0
      DUM2 = 0.0
      DUM3 = 0.0
      DUM4 = 0.0
      DO 300 I = 1, K
      DUM1 = DUM1 + ALOG10(S(I))*ALOG10(N(I))
      DUM2 = DUM2 + ALOG10(N(I))
      DUM3 = DUM3 + ALOG10(S(I))
      DUM4 = DUM4 + ALOG10(S(I))**2
300   CONTINUE
      FD = -(DUM1 - DUM2*DUM3/FLOAT(K))/(DUM4-DUM3**2/FLOAT(K))
      WRITE (*,400) FD
400   FORMAT (5X, 'FRACTAL DIMENSION IS ', F15.6)
c     OPEN (1, FILE = '  ', STATUS = 'NEW')
C     din't seem to like
      DO 500 I = 1, K
      WRITE(*,*) S(I), N(I)
500   CONTINUE
```

```
      STOP
      END
      SUBROUTINE ITER (R, XC, YC, HSIN, HCOS, HYP, XM, YM)
      DIMENSION X(20), Y(20), DIST(20)
      DO 10 I =1, 20
      X(I) = XM + HCOS*0.05*FLOAT(I)*HYP
      Y(I) = YM + HSIN*0.05*FLOAT(I)*HYP
      DIST(I) = ABS(R - SQRT((XC - X(I))**2 +  (YC-Y(I))**2))
10    CONTINUE
      XMIN = 1000000.0
      K = 0
      DO 20 I = 1, 20
      IF (DIST(I) .LT. XMIN) THEN
      XMIN = DIST(I)
      K = I
      ENDIF
20    CONTINUE
      XC = X(K)
      YC = Y(K)
      RETURN
      END
```

APPENDIX B

Microsoft QuickBASIC Digital Roughness Gage Program

```
CLS
PRINT "PROGRAM: DIGITAL ROUGHNESS GAGE version 3.0"
PRINT "THE UNIVERITY OF TENNESSEE, KNOXVILLE"
PRINT "THE DEPARTMENT OF CIVIL AND ENVIRONMENTAL ENGINEERING"
PRINT "IN ASSOCIATION WITH THE INSTITUTE FOR GEOTECHNOLOGY"
PRINT "version 3.0 BY Matt B. Haston 7/15/96"
PRINT
PRINT "USERS GUIDE"
PRINT "CONNECT THE 25-PIN CONNECTOR TO A PARALLEL PORT ON A
COMPUTER THAT"
PRINT "SUPPORTS MICROSOFT QUICKBASIC THEN RUN DIGITAL
ROUGHNESS GAGE VERSION"
PRINT "3.0. THE PROGRAM WILL PROMPT YOU FOR THE INPUT VOLTAGE (5
AND 0 DEFAULT)"
PRINT "NEXT INPUT THE FILE NAME FOR YOUR DATA NEXT THE PROGRAM
WILL GIVE YOU"
PRINT "THE CURRENT X LOCATION OF THE STYLUS TIP ENTER 1 IF THIS IS
OK - PRESS"
PRINT "ENTER IF YOU NEED TO REPOSITION THE STYLUS. THEN YOU WILL
BE GIVEN A"
PRINT "CHOICE OF WHETHER TO CONTINUE OR QUIT"
PRINT ""
PRINT "*********************"
PRINT "*    DRG v.3.0      *"
PRINT "*    UTK-CEE-IG     *"
PRINT "*  Matt B. Haston   *"
PRINT "*********************"

INPUT "PRESS ENTER TO BEGIN"; G$

150 CLS
160 PP = &H3BC
170 REM PP is the address of the Parallel Port used.
190 REM
200 OUT PP + 2, &H4
210 REM This disables the IRQ 7 interrupt and sets up the PP+2
220 REM location so that you can use it to input data.
230 REM
250 LOCATE 21, 20: INPUT "ENTER THE MAXIMUM VOLTAGE (ie. 5)"; MAX
```

```
260 LOCATE 22, 20: INPUT "ENTER THE MINIMUM VOLTAGE (ie. 0)"; MIN
270 LOCATE 23, 20: INPUT "ENTER THE FILENAME FOR YOUR DATA"; Q$

290 FOR INMUX = 0 TO 1
300 GOSUB 530: REM Read data from the I/O port.
310 REM IB is the Input Byte from the I/O port.
320 b = IB: GOSUB 390: REM Organize the data into binary bits for display.
330 VOLT = IB

IF INMUX = 1 THEN X = VOLT ELSE z = VOLT
CLS
350 NEXT INMUX
DO
PRINT "CURRENT X COORDINATE "; X
INPUT "OK TO WRITE TO FILE (1 - YES, ENTER - NO)"; b
IF b = 1 THEN GOTO 354 ELSE GOTO 290
354 OPEN Q$ FOR APPEND AS #2 LEN = LEN(RED)
WRITE #2, X, z
PRINT "COORDINATES WRITTEN TO FILE", Q$
PRINT "x="; X, "z="; z

INPUT "PRESS ENTER WHEN GAGE STYLUS HAS BEEN RELOCATED (Q TO
QUIT)"; R$
IF R$ = "Q" THEN GOTO 1000
LOOP WHILE UCASE$(R$) = "Q"
CLOSE #2

360 A$ = INKEY$: IF LEN(A$) < 1 THEN 290
370 REM Input data from the keyboard if there is any.
380 IF A$ = "Q" OR A$ = "q" THEN LOCATE 23, 1: END ELSE 300
390 REM
400 REM BINARY DISPLAY SUBROUTINE
410 REM
420 b = INT(b)
430 B7 = 0: B6 = 0: B5 = 0: B4 = 0: B3 = 0: B2 = 0: B1 = 0: B0 = 0
440 IF b > 127 THEN B7 = 1: b = b - 128
450 IF b > 63 THEN B6 = 1: b = b - 64
460 IF b > 31 THEN B5 = 1: b = b - 32
470 IF b > 15 THEN B4 = 1: b = b - 16
480 IF b > 7 THEN B3 = 1: b = b - 8
490 IF b > 3 THEN B2 = 1: b = b - 4
500 IF b > 1 THEN B1 = 1: b = b - 2
510 IF b = 1 THEN B0 = 1
```

```
520 REM this was return
530 REM
540 REM Subroutine to read data from the A/D converter.
550 REM
560 OUT PP, &H0: REM Set all bits low on the output port.
570 IM = INMUX AND &H7
580 OUT PP, IM: REM Set the INput MUltipleXer to the correct port.
590 OUT PP, &H8 OR IM: REM Set ALE high.
600 OUT PP, IM: REM Set ALE back low to latch the address of the desired mux.
610 OUT PP, &H10: REM Set START high.
620 OUT PP, &H0: REM Set START back low to start the A/D conversion.
630 IF INP(PP + 1) AND &H8 = 0 THEN 630: REM Wait for the EOC (End Of
640 REM       Convert) Signal to go high before reading the data.
650 A1 = INP(PP + 1) AND &HF0: REM Input the upper half of the byte.
660 A2 = INP(PP + 2) AND &HF: REM Input the lower half of the byte.
670 IB = A1 OR A2: REM Combine then into one byte.
680 REM IB is the Input Byte from the I/O port.

690 RETURN

1000 CLS
BEEP
1010 PRINT "YOUR DIGITAL ROUGHNESS GAGE SESSION IS OVER"
1020 PRINT "CHECK YOUR DATA FOR DUPLICATION OR OMISSION"
PRINT
PRINT "YOUR FILE", Q$
PRINT "CAN BE FOUND IN THE C:/> DIRECTORY"
PRINT
PRINT
PRINT

PRINT "*********************"
PRINT "*   DRG v.3.0     *"
PRINT "*   UTK-CEE-IG    *"
PRINT "* Matt B. Haston  *"
PRINT "*********************"

1030 END
```

APPENDIX C

Microsoft Excel RMS Method Spreadsheet

2.31 mm window size - File: rmstemp.xls

Columns A..F

	A	B	C	D	E	F
1	Window L					
2			I1	S1	I2	S2
3	x cood	z coord	=+INTERCEPT(B3:B6,A3:A6)	=SLOPE(B3:B6,A3:A6)		
4	x cood	z coord	=C3	=D3	=INTERCEPT(B4:B7,A4:A7)	=SLOPE(B4:B7,A4:A7)
5	x cood	z coord	=C4	=D4	=E4	=F4
6	x cood	z coord	=C5	=D5	=E5	=F5
7	x cood	z coord			=E6	=F6
8	x cood	z coord	=+INTERCEPT(B8:B11,A8:A11)	=SLOPE(B8:B11,A8:A11)		
9	x cood	z coord	=C8	=D8	=INTERCEPT(B9:B12,A9:A12)	=SLOPE(B9:B12,A9:A12)
10	x cood	z coord	=C9	=D9	=E9	=F9
11	x cood	z coord	=C10	=D10	=E10	=F10
12	x cood	z coord			=E11	=F11
13	x cood	z coord	=+INTERCEPT(B13:B16,A13:A16)	=SLOPE(B13:B16,A13:A16)		
14	x cood	z coord	=C13	=D13	=INTERCEPT(B14:B17,A14:A17)	=SLOPE(B14:B17,A14:A17)
15	x cood	z coord	=C14	=D14	=E14	=F14
16	x cood	z coord	=C15	=D15	=E15	=F15
17	x cood	z coord			=E16	=F16
18	x cood	z coord	=+INTERCEPT(B18:B21,A18:A21)	=SLOPE(B18:B21,A18:A21)		
19	x cood	z coord	=C18	=D18	=INTERCEPT(B19:B22,A19:A22)	=SLOPE(B19:B22,A19:A22)
20	x cood	z coord	=C19	=D19	=E19	=F19
21	x cood	z coord	=C20	=D20	=E20	=F20
22	x cood	z coord			=E21	=F21
23	x cood	z coord	=+INTERCEPT(B23:B26,A23:A26)	=SLOPE(B23:B26,A23:A26)		
24	x cood	z coord	=C23	=D23	=INTERCEPT(B24:B27,A24:A27)	=SLOPE(B24:B27,A24:A27)
25	x cood	z coord	=C24	=D24	=E24	=F24
26	x cood	z coord	=C25	=D25	=E25	=F25
27	x cood	z coord			=E26	=F26

Columns M..N

	M	N
2	R1	R2
3	=IF(C3<>"",(((B3-(D3*A3+C3))^2)/2)^0.5,"")	
4	=IF(C4<>"",(((B4-(D4*A4+C4))^2)/2)^0.5,"")	=IF(E4<>0,(((B4-(F4*A4+E4))^2)/2)^0.5,"")
5	=IF(C5<>"",(((B5-(D5*A5+C5))^2)/2)^0.5,"")	=IF(E5<>0,(((B5-(F5*A5+E5))^2)/2)^0.5,"")
6	=IF(C6<>"",(((B6-(D6*A6+C6))^2)/2)^0.5,"")	=IF(E6<>0,(((B6-(F6*A6+E6))^2)/2)^0.5,"")
7	=IF(C7<>"",(((B7-(D7*A7+C7))^2)/2)^0.5,"")	=IF(E7<>0,(((B7-(F7*A7+E7))^2)/2)^0.5,"")
8	=IF(C8<>"",(((B8-(D8*A8+C8))^2)/2)^0.5,"")	=IF(E8<>0,(((B8-(F8*A8+E8))^2)/2)^0.5,"")
9	=IF(C9<>"",(((B9-(D9*A9+C9))^2)/2)^0.5,"")	=IF(E9<>0,(((B9-(F9*A9+E9))^2)/2)^0.5,"")
10	=IF(C10<>"",(((B10-(D10*A10+C10))^2)/2)^0.5,"")	=IF(E10<>0,(((B10-(F10*A10+E10))^2)/2)^0.5,"")
11	=IF(C11<>"",(((B11-(D11*A11+C11))^2)/2)^0.5,"")	=IF(E11<>0,(((B11-(F11*A11+E11))^2)/2)^0.5,"")
12	=IF(C12<>"",(((B12-(D12*A12+C12))^2)/2)^0.5,"")	=IF(E12<>0,(((B12-(F12*A12+E12))^2)/2)^0.5,"")
13	=IF(C13<>"",(((B13-(D13*A13+C13))^2)/2)^0.5,"")	=IF(E13<>0,(((B13-(F13*A13+E13))^2)/2)^0.5,"")
14	=IF(C14<>"",(((B14-(D14*A14+C14))^2)/2)^0.5,"")	=IF(E14<>0,(((B14-(F14*A14+E14))^2)/2)^0.5,"")
15	=IF(C15<>"",(((B15-(D15*A15+C15))^2)/2)^0.5,"")	=IF(E15<>0,(((B15-(F15*A15+E15))^2)/2)^0.5,"")
16	=IF(C16<>"",(((B16-(D16*A16+C16))^2)/2)^0.5,"")	=IF(E16<>0,(((B16-(F16*A16+E16))^2)/2)^0.5,"")
17	=IF(C17<>"",(((B17-(D17*A17+C17))^2)/2)^0.5,"")	=IF(E17<>0,(((B17-(F17*A17+E17))^2)/2)^0.5,"")
18	=IF(C18<>"",(((B18-(D18*A18+C18))^2)/2)^0.5,"")	=IF(E18<>0,(((B18-(F18*A18+E18))^2)/2)^0.5,"")
19	=IF(C19<>"",(((B19-(D19*A19+C19))^2)/2)^0.5,"")	=IF(E19<>0,(((B19-(F19*A19+E19))^2)/2)^0.5,"")
20	=IF(C20<>"",(((B20-(D20*A20+C20))^2)/2)^0.5,"")	=IF(E20<>0,(((B20-(F20*A20+E20))^2)/2)^0.5,"")
21	=IF(C21<>"",(((B21-(D21*A21+C21))^2)/2)^0.5,"")	=IF(E21<>0,(((B21-(F21*A21+E21))^2)/2)^0.5,"")
22	=IF(C22<>"",(((B22-(D22*A22+C22))^2)/2)^0.5,"")	=IF(E22<>0,(((B22-(F22*A22+E22))^2)/2)^0.5,"")
23	=IF(C23<>"",(((B23-(D23*A23+C23))^2)/2)^0.5,"")	=IF(E23<>0,(((B23-(F23*A23+E23))^2)/2)^0.5,"")
24	=IF(C24<>"",(((B24-(D24*A24+C24))^2)/2)^0.5,"")	=IF(E24<>0,(((B24-(F24*A24+E24))^2)/2)^0.5,"")
25	=IF(C25<>"",(((B25-(D25*A25+C25))^2)/2)^0.5,"")	=IF(E25<>0,(((B25-(F25*A25+E25))^2)/2)^0.5,"")
26	=IF(C26<>"",(((B26-(D26*A26+C26))^2)/2)^0.5,"")	=IF(E26<>0,(((B26-(F26*A26+E26))^2)/2)^0.5,"")
27	=IF(C27<>"",(((B27-(D27*A27+C27))^2)/2)^0.5,"")	=IF(E27<>0,(((B27-(F27*A27+E27))^2)/2)^0.5,"")
28	=IF(C28<>"",(((B28-(D28*A28+C28))^2)/2)^0.5,"")	=IF(E28<>0,(((B28-(F28*A28+E28))^2)/2)^0.5,"")
29	=IF(C29<>"",(((B29-(D29*A29+C29))^2)/2)^0.5,"")	=IF(E29<>0,(((B29-(F29*A29+E29))^2)/2)^0.5,"")

Columns M..N (lower)

	M	N
1028	=IF(C1028<>"",(((B1028-(D1028*A1028+C1028)	=IF(E1028<>0,(((B1028-(F1028*A1028+E1028)
1029	=IF(C1029<>"",(((B1029-(D1029*A1029+C1029)	=IF(E1029<>0,(((B1029-(F1029*A1029+E1029)
1030		
1031	=SUM(M3:M1029)	=SUM(N3:N1029)
1032		
1033		=SUM(M1030:Q1030)
1034		
1035		=SUM(R7:R1025)
1036		
1037	RMS =	=N1033/1022
1038		

3.85 mm window size
Columns A..D

	A	B	C	D
1	RMS	3.85		
2			I1	S1
3	x coord	z coord	=INTERCEPT(B3:B8,A3:A8)	=SLOPE(B3:B8,A3:A8)
4	x coord	z coord	=C3	=D3
5	x coord	z coord	=C4	=D4
6	x coord	z coord	=C5	=D5
7	x coord	z coord	=C6	=D6
8	x coord	z coord	=C7	=D7
9	x coord	z coord		
10	x coord	z coord	=INTERCEPT(B10:B15,A10:A15)	=SLOPE(B10:B15,A10:A15)
11	x coord	z coord	=C10	=D10
12	x coord	z coord	=C11	=D11
13	x coord	z coord	=C12	=D12
14	x coord	z coord	=C13	=D13
15	x coord	z coord	=C14	=D14
16	x coord	z coord		
17	x coord	z coord	=INTERCEPT(B17:B22,A17:A22)	=SLOPE(B17:B22,A17:A22)
18	x coord	z coord	=C17	=D17
19	x coord	z coord	=C18	=D18
20	x coord	z coord	=C19	=D19
21	x coord	z coord	=C20	=D20
22	x coord	z coord	=C21	=D21
23	x coord	z coord		

Column Q

	Q
1	
2	R1
3	=IF(C3<>"",(((B3-(D3*A3+C3))^2)/4)^0.5,"")
4	=IF(C4<>"",(((B4-(D4*A4+C4))^2)/4)^0.5,"")
5	=IF(C5<>"",(((B5-(D5*A5+C5))^2)/4)^0.5,"")
6	=IF(C6<>"",(((B6-(D6*A6+C6))^2)/4)^0.5,"")
7	=IF(C7<>"",(((B7-(D7*A7+C7))^2)/4)^0.5,"")
8	=IF(C8<>"",(((B8-(D8*A8+C8))^2)/4)^0.5,"")
9	=IF(C9<>"",(((B9-(D9*A9+C9))^2)/4)^0.5,"")

coulmns P..Q (lower)

	P	Q
1026		=IF(C1026<>"",(((B1026-(D1026*A1026+C1026))^2)/4)^0.5,"")
1027		=IF(C1027<>"",(((B1027-(D1027*A1027+C1027))^2)/4)^0.5,"")
1028		=IF(C1028<>"",(((B1028-(D1028*A1028+C1028))^2)/4)^0.5,"")
1029		=SUM(Q3:Q1028)
1030		
1031	sums =	=SUM(Q1029:W1029)
1032		
1033		=SUM(X3:X1028)
1034		
1035	RMS =	=Q1031/Q1033

5.39 mm window size

Columns A..D

	A	B	C	D
1	RMS window 5.39			
2			I1	S1
3	x coord	z coord	=INTERCEPT(B3:B10,A3:A10)	=SLOPE(B3:B10,A3:A10)
4	x coord	z coord	=C3	=D3
5	x coord	z coord	=C4	=D4
6	x coord	z coord	=C5	=D5
7	x coord	z coord	=C6	=D6
8	x coord	z coord	=C7	=D7
9	x coord	z coord	=C8	=D8
10	x coord	z coord	=C9	=D9

Column U

	U
1	
2	R1
3	=IF(C3<>"",(((B3-(D3*A3+C3))^2)/6)^0.5,"")
4	=IF(C4<>"",(((B4-(D4*A4+C4))^2)/6)^0.5,"")
5	=IF(C5<>"",(((B5-(D5*A5+C5))^2)/6)^0.5,"")
6	=IF(C6<>"",(((B6-(D6*A6+C6))^2)/6)^0.5,"")
7	=IF(C7<>"",(((B7-(D7*A7+C7))^2)/6)^0.5,"")
8	=IF(C8<>"",(((B8-(D8*A8+C8))^2)/6)^0.5,"")
9	=IF(C9<>"",(((B9-(D9*A9+C9))^2)/6)^0.5,"")
10	=IF(C10<>"",(((B10-(D10*A10+C10))^2)/6)^0.5,"")
11	=IF(C11<>"",(((B11-(D11*A11+C11))^2)/6)^0.5,"")
12	=IF(C12<>"",(((B12-(D12*A12+C12))^2)/6)^0.5,"")
13	=IF(C13<>"",(((B13-(D13*A13+C13))^2)/6)^0.5,"")
14	=IF(C14<>"",(((B14-(D14*A14+C14))^2)/6)^0.5,"")
15	=IF(C15<>"",(((B15-(D15*A15+C15))^2)/6)^0.5,"")
16	=IF(C16<>"",(((B16-(D16*A16+C16))^2)/6)^0.5,"")

Columns T..U (lower)

	T	U
1025	=T1024	=IF(C1025<>"",(((B1025-(D1025*A1025+C1025))^2)/6)^0.5,"")
1026	=T1025	=IF(C1026<>"",(((B1026-(D1026*A1026+C1026))^2)/6)^0.5,"")
1027	##	=IF(C1027<>"",(((B1027-(D1027*A1027+C1027))^2)/6)^0.5,"")
1028	"	
1029	sums R1=	=SUM(U3:U1028)
1030		
1031	sum Rs=	=SUM(U1029:AC1029)
1032		
1033	Num. Win.	=SUM(AD6:AD1026)
1034		
1035	RMS =	=U1031/U1033

APPENDIX D

Microsoft Excel Variogram Method Spreadsheet

File: vartemp.xls
Columns A..F

	A	B	C	D	E	F
1				Variogram	Fractal Dimension	
2	x coord	z coord				
3	x coord	z coord	=IF(D3<>"",1,"")	=IF(B3<>"",(B2-B3)^2,"")		
4	x coord	z coord	=IF(D4<>"",1,"")	=IF(B4<>"",(B3-B4)^2,"")	=IF(B4<>"",(B4-B2)^2,"")	
5	x coord	z coord	=IF(D5<>"",1,"")	=IF(B5<>"",(B4-B5)^2,"")	=IF(B5<>"",(B5-B3)^2,"")	=IF(B5<>"",(B2-B5)^2,"")
6	x coord	z coord	=IF(D6<>"",1,"")	=IF(B6<>"",(B5-B6)^2,"")	=IF(B6<>"",(B6-B4)^2,"")	=IF(B6<>"",(B3-B6)^2,"")
7	x coord	z coord	=IF(D7<>"",1,"")	=IF(B7<>"",(B6-B7)^2,"")	=IF(B7<>"",(B7-B5)^2,"")	=IF(B7<>"",(B4-B7)^2,"")
8	x coord	z coord	=IF(D8<>"",1,"")	=IF(B8<>"",(B7-B8)^2,"")	=IF(B8<>"",(B8-B6)^2,"")	=IF(B8<>"",(B5-B8)^2,"")
9	""""""""""""""""	""""""""""""""""	""""""""""""""""""""""	""""""""""""""""""""""	""""""""""""""""""""""	""""""""""""""""""""""
10			=SUM(C3:C8)	=SUM(D3:D8)	=SUM(E3:E8)	=SUM(F3:F8)
11						
12						
13				=D10/(2*C10)	Smallest Window Size	
14				=(E10/(2*(C10-1)))	Next Window Size	
15				=(F10/(2*(C10-2)))	Next Window Size	
16				=(G10/(2*(C10-3)))	Next Window Size	
17				=H10/(2*(C10-4))	Next Window Size	
18				=I10/(2*(C10-5))	Next Window Size	
19				""""""""""""""""""""""""	""""""""""""""""""""""""	

Columns G..J

	G	H	I	J
1				
2				
3				
4				
5				
6	=IF(B6<>"",(B2-B6)^2,"")			
7	=IF(B7<>"",(B3-B7)^2,"")	=IF(B7<>"",(B2-B7)^2,"")		
8	=IF(B8<>"",(B4-B8)^2,"")	=IF(B8<>"",(B3-B8)^2,"")	=IF(B8<>"",(B2-B8)^2,"")	
9	""""""""""""""""""""""	""""""""""""""""""""""	""""""""""""""""""""""	""""""""""
10	=SUM(G3:G8)	=SUM(H3:H8)	=SUM(I3:I8)	""""""""""
11				
12	y	x		
13	=LOG(D13)	=LOG(E13)		
14	=LOG(D14)	=LOG(E14)		
15	=LOG(D15)	=LOG(E15)		
16	=LOG(D16)	=LOG(E16)		
17	=LOG(D17)	=LOG(E17)		
18	=LOG(D18)	=LOG(E18)		
19	""""""""""""""""""""""""	""""""""""""""""""""""""""		

APPENDIX E

Microsoft Excel WAM Method Spreadsheet

Columns A..E File: wamtemp.xls

	A	B	C	D	E
1			Microangle	Fractal Dimension	
2	x coord	z coorc			
3	x coord	z coorc	=IF(D3<>"",1,"")	=IF(B3<>"",DEGREES(ATAN(ABS((B3-B2)/(A3-A2)))),"")	
4	x coord	z coorc	=IF(D4<>"",1,"")	=IF(B4<>"",DEGREES(ATAN(ABS((B4-B3)/(A4-A3)))),"")	=IF(B4<>"",(DEGREES(ATAN(ABS(B4-B2)/(A4-A2)))),"")
5	x coord	z coorc	=IF(D5<>"",1,"")	=IF(B5<>"",DEGREES(ATAN(ABS((B5-B4)/(A5-A4)))),"")	=IF(B5<>"",(DEGREES(ATAN(ABS(B5-B3)/(A5-A3)))),"")
6	x coord	z coorc	=IF(D6<>"",1,"")	=IF(B6<>"",DEGREES(ATAN(ABS((B6-B5)/(A6-A5)))),"")	=IF(B6<>"",(DEGREES(ATAN(ABS(B6-B4)/(A6-A4)))),"")
7	x coord	z coorc	=IF(D7<>"",1,"")	=IF(B7<>"",DEGREES(ATAN(ABS((B7-B6)/(A7-A6)))),"")	=IF(B7<>"",(DEGREES(ATAN(ABS(B7-B5)/(A7-A5)))),"")
8	x coord	z coorc	=IF(D8<>"",1,"")	=IF(B8<>"",DEGREES(ATAN(ABS((B8-B7)/(A8-A7)))),"")	=IF(B8<>"",(DEGREES(ATAN(ABS(B8-B6)/(A8-A6)))),"")
9	x coord	z coorc	=IF(D9<>"",1,"")	=IF(B9<>"",DEGREES(ATAN(ABS((B9-B8)/(A9-A8)))),"")	=IF(B9<>"",(DEGREES(ATAN(ABS(B9-B7)/(A9-A7)))),"")
10	x coord	z coorc	=IF(D10<>"",1,"")	=IF(B10<>"",DEGREES(ATAN(ABS((B10-B9)/(A10-A9)))),"")	=IF(B10<>"",(DEGREES(ATAN(ABS(B10-B8)/(A10-A8)))),"")
11	x coord	z coorc	=IF(D11<>"",1,"")	=IF(B11<>"",DEGREES(ATAN(ABS((B11-B10)/(A11-A10)))),"")	=IF(B11<>"",(DEGREES(ATAN(ABS(B11-B9)/(A11-A9)))),"")
12	x coord	z coorc	=IF(D12<>"",1,"")	=IF(B12<>"",DEGREES(ATAN(ABS((B12-B11)/(A12-A11)))),"")	=IF(B12<>"",(DEGREES(ATAN(ABS(B12-B10)/(A12-A10)))),""
13	x coord	z coorc	=IF(D13<>"",1,"")	=IF(B13<>"",DEGREES(ATAN(ABS((B13-B12)/(A13-A12)))),"")	=IF(B13<>"",(DEGREES(ATAN(ABS(B13-B11)/(A13-A11)))),""
14	x coord	z coorc	=IF(D14<>"",1,"")	=IF(B14<>"",DEGREES(ATAN(ABS((B14-B13)/(A14-A13)))),"")	=IF(B14<>"",(DEGREES(ATAN(ABS(B14-B12)/(A14-A12)))),""
15			=SUM(C3:C14)	=SUM(D3:D14)	=SUM(E3:E14)
16					
17				WAM values	Windows
18				=D15/(C15)	Smallest window size
19				=(E15/((C15-1)))	Next window size
20				=(F15/((C15-2)))	Next window size
21				=(G15/((C15-3)))	Next window size
22				=#REF!/((C15-4))	Next window size
23				=H15/((C15-5))	Next window size
24				##########	##########
25					

Columns E..G

	E	F	G
2			
3			
4	=IF(B4<>"",(DEGREES(ATAN(ABS(B4-B2)/(A4-A2)))),"")		
5	=IF(B5<>"",(DEGREES(ATAN(ABS(B5-B3)/(A5-A3)))),"")	=IF(B5<>"",DEGREES(ATA	
6	=IF(B6<>"",(DEGREES(ATAN(ABS(B6-B4)/(A6-A4)))),"")	=IF(B6<>"",DEGREES(ATA	=IF(B6<>"",DEGREES(ATAN(ABS(B6-B2)/(A6-A2))),"")
7	=IF(B7<>"",(DEGREES(ATAN(ABS(B7-B5)/(A7-A5)))),"")	=IF(B7<>"",DEGREES(ATA	=IF(B7<>"",DEGREES(ATAN(ABS(B7-B3)/(A7-A3))),"")
8	=IF(B8<>"",(DEGREES(ATAN(ABS(B8-B6)/(A8-A6)))),"")	=IF(B8<>"",DEGREES(ATA	=IF(B8<>"",DEGREES(ATAN(ABS(B8-B4)/(A8-A4))),"")
9	=IF(B9<>"",(DEGREES(ATAN(ABS(B9-B7)/(A9-A7)))),"")	=IF(B9<>"",DEGREES(ATA	=IF(B9<>"",DEGREES(ATAN(ABS(B9-B5)/(A9-A5))),"")
10	=IF(B10<>"",(DEGREES(ATAN(ABS(B10-B8)/(A10-A8)))),"")	=IF(B10<>"",DEGREES(AT	=IF(B10<>"",DEGREES(ATAN(ABS(B10-B6)/(A10-A6))),"")
11	=IF(B11<>"",(DEGREES(ATAN(ABS(B11-B9)/(A11-A9)))),"")	=IF(B11<>"",DEGREES(AT	=IF(B11<>"",DEGREES(ATAN(ABS(B11-B7)/(A11-A7))),"")
12	=IF(B12<>"",(DEGREES(ATAN(ABS(B12-B10)/(A12-A10)))),""	=IF(B12<>"",DEGREES(AT	=IF(B12<>"",DEGREES(ATAN(ABS(B12-B8)/(A12-A8))),"")
13	=IF(B13<>"",(DEGREES(ATAN(ABS(B13-B11)/(A13-A11)))),""	=IF(B13<>"",DEGREES(AT	=IF(B13<>"",DEGREES(ATAN(ABS(B13-B9)/(A13-A9))),"")
14	=IF(B14<>"",(DEGREES(ATAN(ABS(B14-B12)/(A14-A12)))),""	=IF(B14<>"",DEGREES(AT	=IF(B14<>"",DEGREES(ATAN(ABS(B14-B10)/(A14-A10))),""
15	=SUM(E3:E14)	=SUM(F3:F14)	=SUM(G3:G14)
16			
17	Windows	y	x
18	Smallest window size	=LOG(D18)	=LOG(E18)
19	Next window size	=LOG(D19)	=LOG(E19)
20	Next window size	=LOG(D20)	=LOG(E20)
21	Next window size	=LOG(D21)	=LOG(E21)
22	Next window size	=LOG(D22)	=LOG(E22)
23	Next window size	=LOG(D23)	=LOG(E23)
24	##########	##########	##########

APPENDIX F

Shear Test Data Sheet

The University of Tennessee
Department of Civil and Environmental Engineering
Geotechnical Research Laboratory File: shear.wpd
Direct Shear Test

Date__________ Tested by______________________________
Project____
Sample Identification____
____

Sample Diameter__________ Dip of Discontinuity __________

Shear Plane Area__________

Required Normal Stress on Shear Plane____________

Corresponding Normal Load_____________

Normal Gage Pressure Required_____________

Corresponding Pressure Maintainer Setting: Initial______ Final _________

Normal Piston Area = 20.26 cm^2 Shear Piston Area = 14.43 cm^2

Normal Gage Pressure	Shear Gage Pressure	Horizontal Displacement

APPENDIX G

Point Load Test Data Sheet

File: point.wpd

THE UNIVERSITY OF TENNESSEE

Department of Civil and Environmental Engineering

Geotechnical Laboratory

POINT LOAD TESTING

Project ____________________ Sample I.D. ____________________

Description of Sample ____

Tested By _________ Date _________ Platens: Conical Flat Plate

Test	Type*	W (mm)	D(mm)	L(mm)	DP_I**	DP_F***	Gage (units)

*Use the following notations: d - diametral, a - axial, l - lump; also record whether the test was conducted parallel (II) or perpendicular($\perp$) to planes of weakness.

whether the test was conducted parallel (II) or perpendicular($\perp$) to planes of weakness.

** Initial platen distance as read from the point load machine.

*** Final platen distance as read from the point load machine.

APPENDIX H

SHEAR TEST DATA

Direct Shear Test Results		
Sample 1-1B*2		
Tested 7/16/96 by MBH	Dip = 36 degrees	
	Diameter = 50mm	
Normal Gage Pressure (kPa)	Shear Gage Pressure (kPa)	Shear Plane Area (m^2)**
1173	4300	0.00243
2375	6300	0.00243
3625	7550	0.00243
Normal Stress (kPa)	Shear Stress (kPa)	
977.98	2925.00	
1980.14	3741.11	
3022.33	4483.40	

Direct Shear Test Results		
Sample 10-5B (19.2)		
Tested 7/22/96 by MBH	Dip = 28 degrees	
	Diameter = 50mm	
Normal Gage Pressure (kPa)	Shear Gage Pressure (kPa)	Shear Plane Area (m^2)**
1125	1605	0.00222
2200	2300	0.00222
3300	3375	0.00222
Normal Stress (kPa)	Shear Stress (kPa)	
1026.69	893.75	
2007.75	1495.00	
3011.62	2193.75	

Direct Shear Test Results		
Sample 10-8A		
Tested 7/16/96 by MBH	Dip = 55 degrees	
	Diameter = 50mm	
Normal Gage Pressure (kPa)	Shear Gage Pressure (kPa)	Shear Plane Area (m^2)**
1625	1700	0.00342
3375	2850	0.00342
5050	4050	0.00342
Normal Stress (kPa)	Shear Stress (kPa)	
962.65	717.28	
1999.34	1202.50	
2991.61	1708.82	

Direct Shear Test Results		
Sample 10-1		
Tested 7/22/96 by MBH	Dip = 21 degrees	
	Diameter = 50mm	
Normal Gage Pressure (kPa)	Shear Gage Pressure (kPa)	Shear Plane Area (m^2)**
1000	1550	0.00210
2075	2475	0.00210
3125	2700	0.00210
Normal Stress (kPa)	Shear Stress (kPa)	
964.76	1605.25	
2001.88	1700.68	
3014.88	1855.29	

Direct Shear Test Results		
Sample 1-4A (10.77)		
Tested 7/22/96 by MBH	Dip = 53 degrees	
	Diameter = 50mm	
Normal Gage Pressure (kPa)	Shear Gage Pressure (kPa)	Shear Plane Area (m^2)**
1625	7000	0.00326
3250	8625	0.00326
4875	10625	0.00326
Normal Stress (kPa)	Shear Stress (kPa)	
1009.89	3098.47	
2019.79	3817.75	
3029.68	4703.03	

Direct Shear Test Results		
Sample 2-2B (10.53-10.80)		
Tested 7/17/96 by MBH	Dip = 29 degrees	
	Diameter = 50mm	
Normal Gage Pressure (kPa)	Shear Gage Pressure (kPa)	Shear Plane Area (m^2)**
1125	2500	0.00224
2250	3500	0.00224
3375	4375	0.00224
Normal Stress (kPa)	Shear Stress (kPa)	
1017.52	1610.49	
2035.04	2254.69	
3052.57	2818.36	

Direct Shear Test Results		
Sample 2-2B (11.8)		
Tested 7/17/96 by MBH	Dip = 28 degrees	
	Diameter = 50mm	
Normal Gage Pressure (kPa)	Shear Gage Pressure (kPa)	Shear Plane Area (m^2)**
1125	2900	0.00222
2125	3750	0.00222
3250	5000	0.00222
Normal Stress (kPa)	Shear Stress (kPa)	
1026.69	1885.00	
1939.30	2437.50	
2965.99	3250.00	

Direct Shear Test Results		
Sample 3-3A		
Tested 1/13/96 by MBH	Dip = 34 degrees	
	Diameter = 50mm	
Normal Gage Pressure (kPa)	Shear Gage Pressure (kPa)	Shear Plane Area (m^2)**
750	4000	0.00237
1250	3900	0.00237
1875	4325	0.00237
Normal Stress (kPa)	Shear Stress (kPa)	
641.14	2832.44	
1068.57	2374.56	
1602.85	2633.32	

Direct Shear Test Results		
Sample 7-4A		
Tested 1/5/96 by MBH	Dip = 33 degrees	
	Diameter = 50mm	
Normal Gage Pressure (KPa)	Shear Gage Pressure (KPa)	Shear Plane Area (m^2)**
700	1225	0.00234
1250	2100	0.00234
1875	2550	0.00234
Normal Stress (kPa)	Shear Stress (KPa)	
606.07	755.42	
1082.26	1295.00	
1623.40	1572.50	

Direct Shear Test Results		
Sample 4-6A		
Tested 1/3/96 by MBH	Dip = 19 degrees	
	Diameter = 50mm	
Normal Gage Pressure (KPa)	Shear Gage Pressure (KPa)	Shear Plane Area (m^2)**
500	1400	0.00156
875	1925	0.00156
1625	2750	0.00156
Normal Stress (kPa)	Shear Stress (KPa)	
649.36	1295.00	
1136.38	1780.63	
2110.42	2543.75	

Direct Shear Test Results		
Sample 5-4B		
Tested 1/15/96 by MBH	Dip = 0 degrees	
	Diameter = 50mm	
Normal Gage Pressure (KPa)	Shear Gage Pressure (KPa)	Shear Plane Area (m^2)**
600	3875	0.00196
1125	4200	0.00196
1500	4600	0.00196
Normal Stress (kPa)	Shear Stress (KPa)	
620.20	2852.87	
1162.88	3092.14	
1550.51	3386.63	

Direct Shear Test Results		
Sample 6-1A		
Tested 1/4/95 by MBH	Dip = 17 degrees	
	Diameter = 50mm	
Normal Gage Pressure (KPa)	Shear Gage Pressure (KPa)	Shear Plane Area (m^2)**
625	1175	0.00205
1125	1600	0.00205
1625	1900	0.00205
Normal Stress (kPa)	Shear Stress (KPa)	
617.68	1019.09	
1111.83	1126.24	
1605.98	1337.41	

Direct Shear Test Results		
Sample A-8 3.0		
Tested 7/22/96 by MBH	Dip = 12 degrees	
	Diameter = 50mm	
Normal Gage Pressure (kPa)	Shear Gage Pressure (kPa)	Shear Plane Area (m^2)**
1000	2675	0.00201
2000	3150	0.00201
3000	3700	0.00201
Normal Stress (kPa)	Shear Stress (kPa)	
1007.96	2348.25	
2015.92	2261.42	
3023.88	2656.27	

Direct Shear Test Results		
Sample 7-4A		
Tested 1/5/96 by MBH	Dip = 33 degrees	
	Diameter = 50mm	
Normal Gage Pressure (kPa)	Shear Gage Pressure (kPa)	Shear Plane Area (m^2)**
700	1225	0.00234
1250	2100	0.00234
1875	2550	0.00234
Normal Stress (kPa)	Shear Stress (kPa)	
606.07	755.42	
1082.26	1295.00	
1623.40	1572.50	

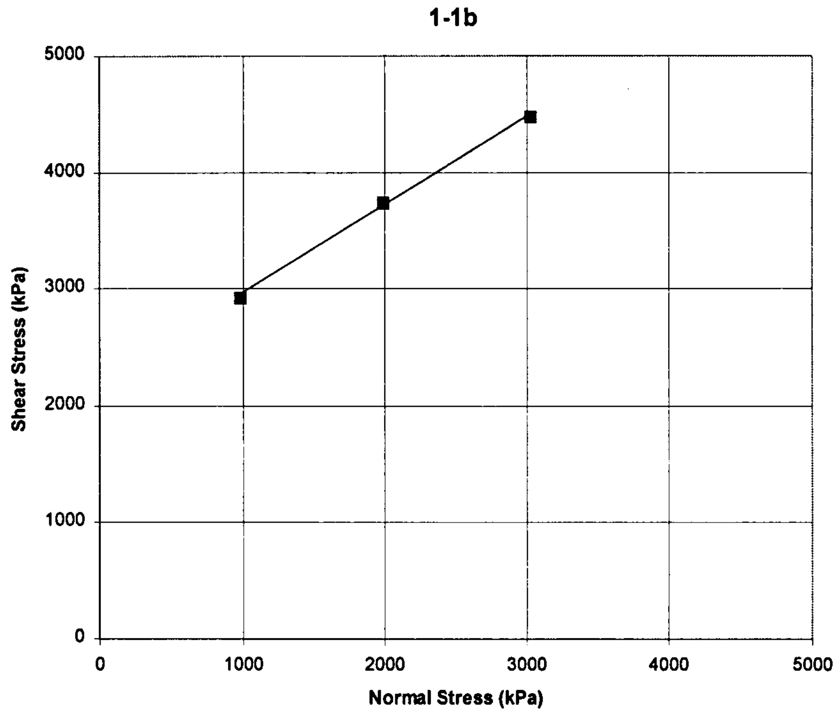

1-1b
Shear Stress (kPa)
5000
4000
3000
2000
1000
0
0
1000
2000
3000
4000
5000
Normal Stress (kPa)

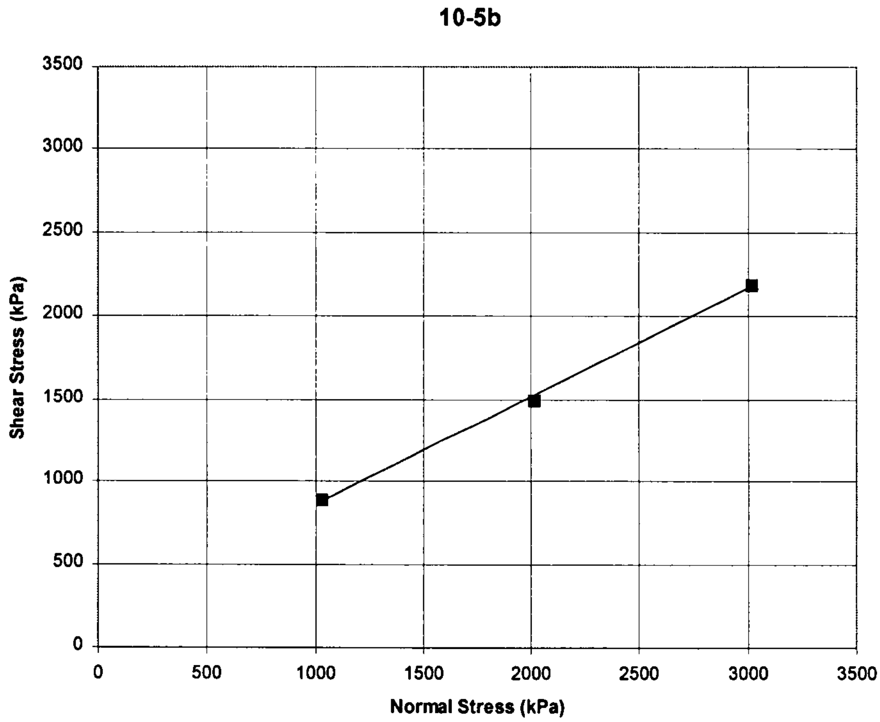

10-5b
Shear Stress (kPa)
3500
3000
2500
2000
1500
1000
500
0
0
500
1000
1500
2000
2500
3000
3500
Normal Stress (kPa)

10-8a

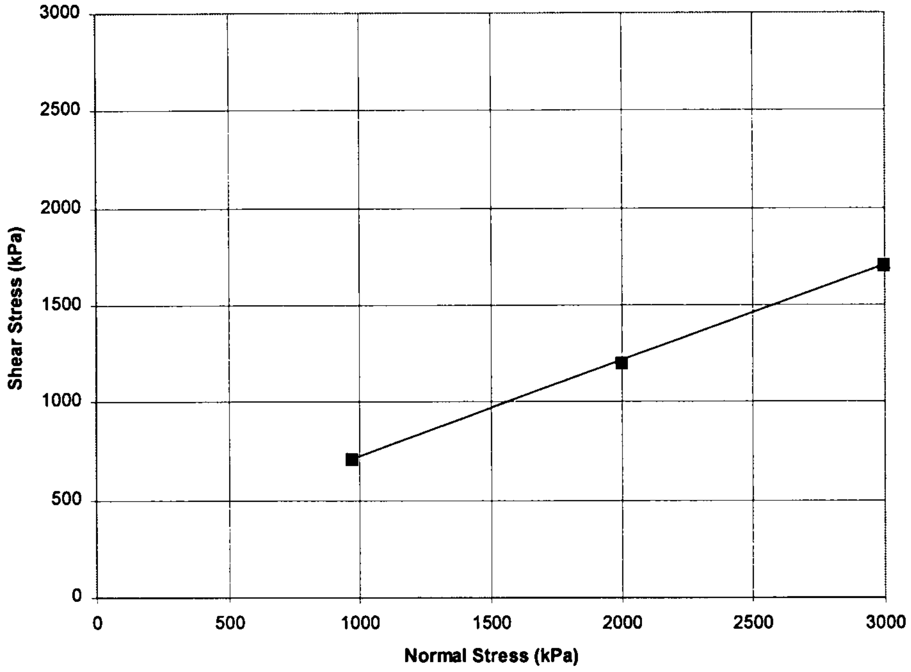

3000
2500
2000
1500
1000
500
0
Shear Stress (kPa)
0
500
1000
1500
2000
2500
3000
Normal Stress (kPa)

'10-1

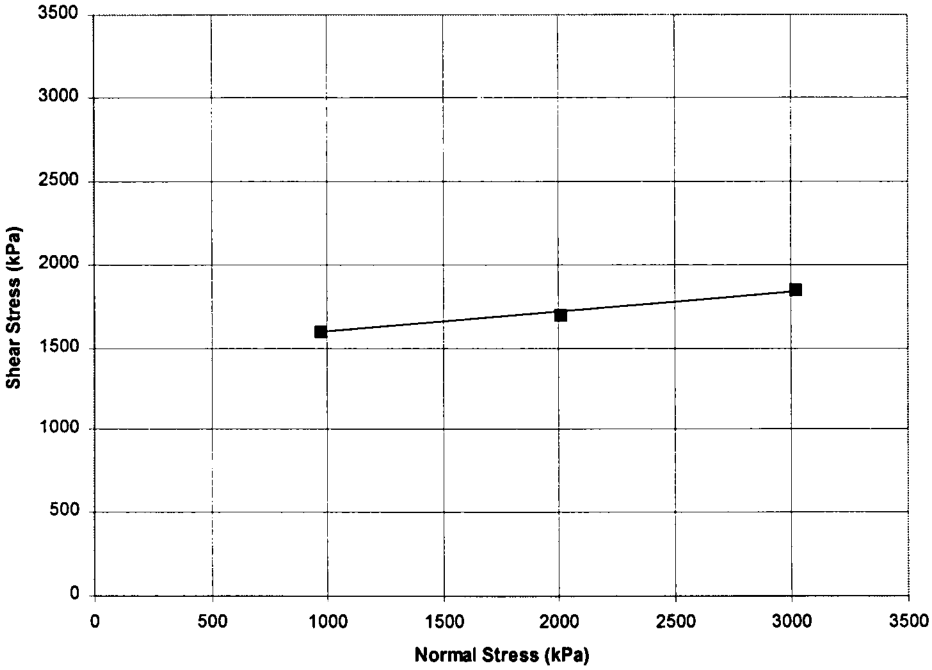

3500
3000
2500
2000
1500
1000
500
0
Shear Stress (kPa)
0
500
1000
1500
2000
2500
3000
3500
Normal Stress (kPa)

1-4a

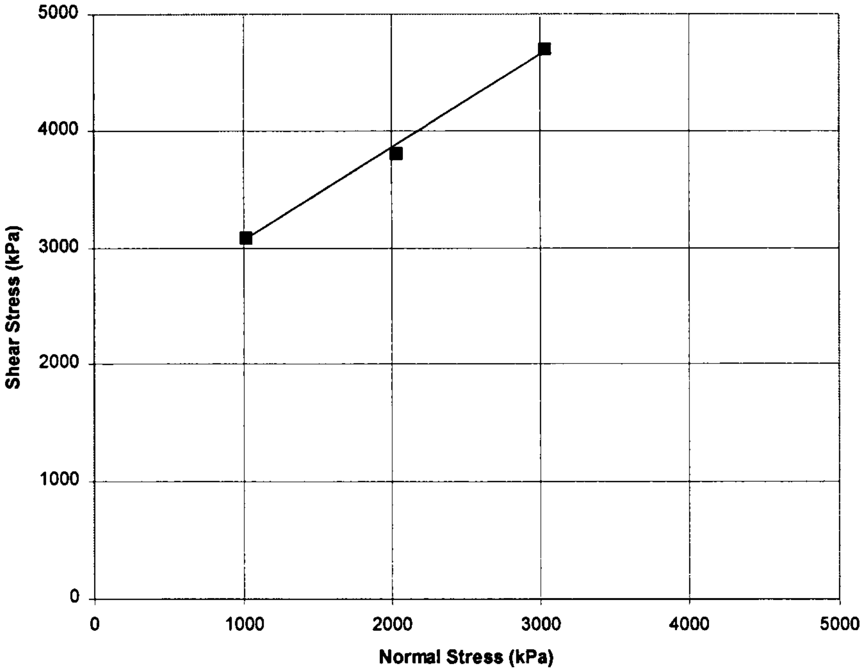

Shear Stress (kPa)
5000
4000
3000
2000
1000
0
0
1000
2000
3000
4000
5000
Normal Stress (kPa)

2-2b 10.53

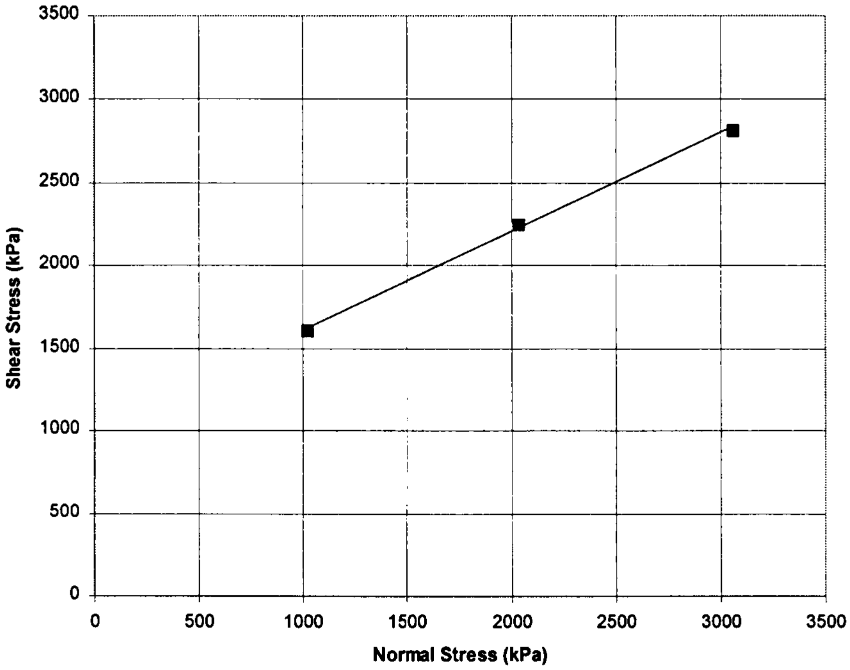

Shear Stress (kPa)
3500
3000
2500
2000
1500
1000
500
0
0
500
1000
1500
2000
2500
3000
3500
Normal Stress (kPa)

2-2b 11.8

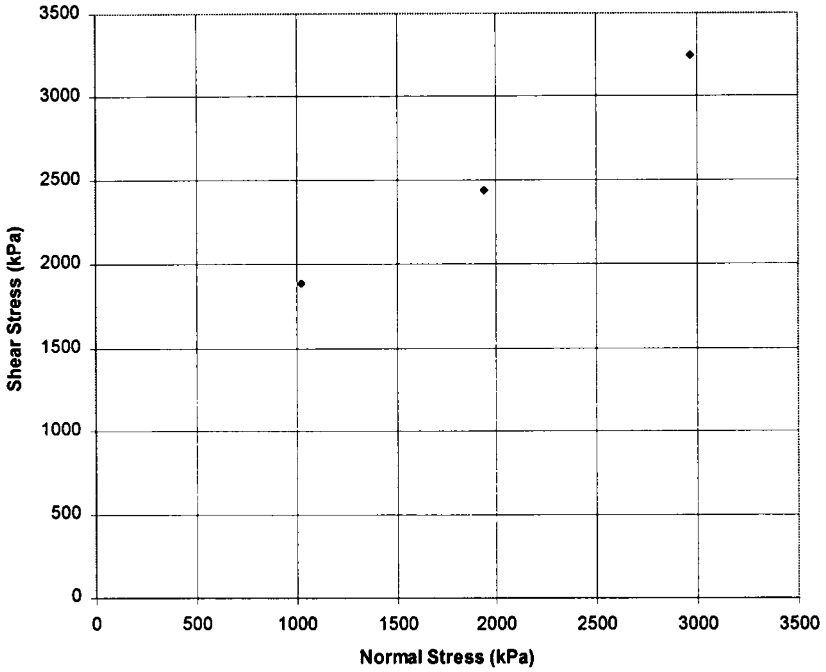
3500
3000
2500
2000
1500
1000
500
0
Shear Stress (kPa)
0
500
1000
1500
2000
2500
3000
3500
Normal Stress (kPa)

3-3a

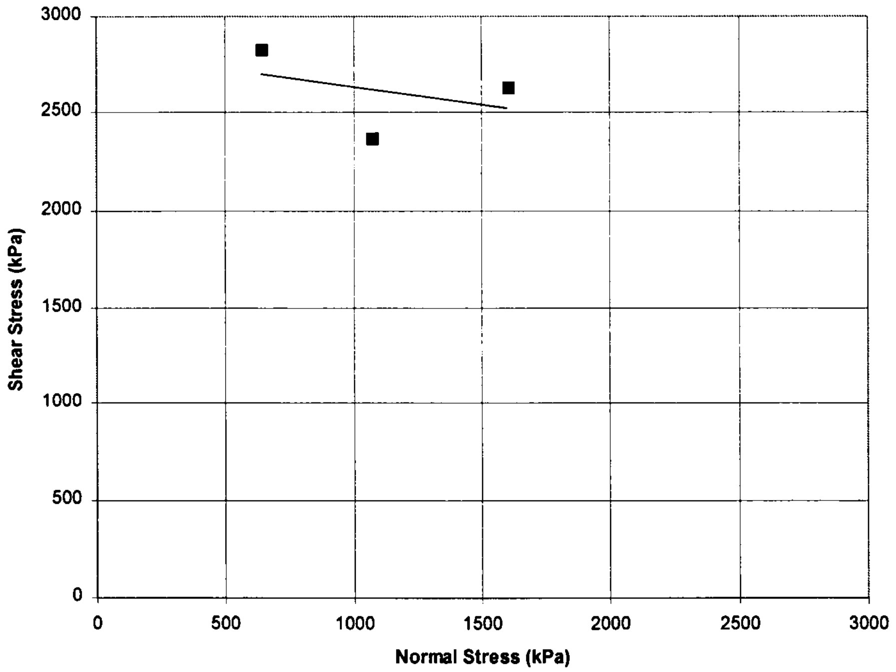
3000
2500
2000
1500
1000
500
0
Shear Stress (kPa)
0
500
1000
1500
2000
2500
3000
Normal Stress (kPa)

7-4a

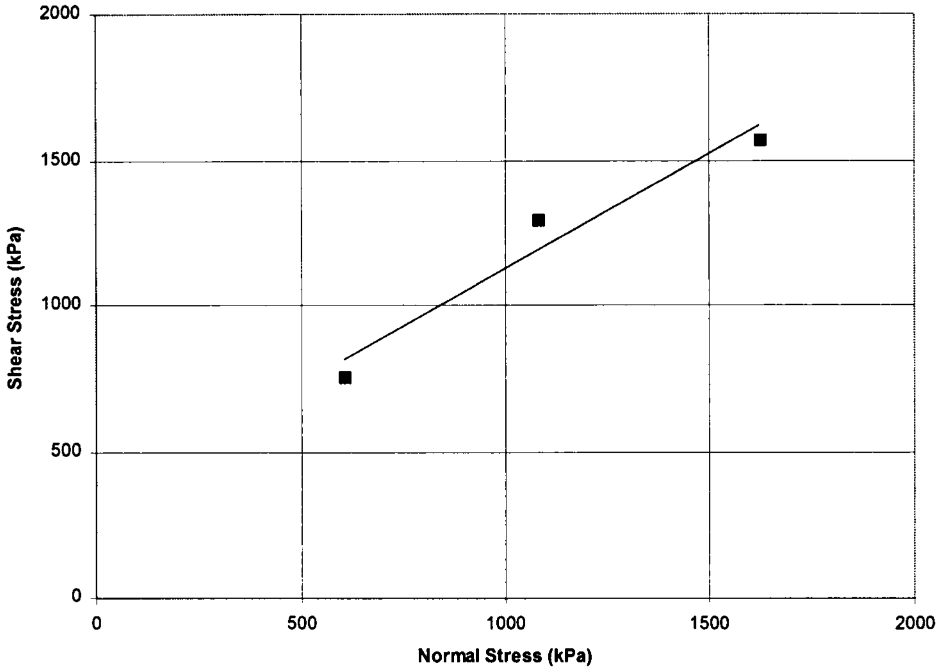

2000
1500
1000
500
0
Shear Stress (kPa)
0
500
1000
1500
2000
Normal Stress (kPa)

4-6a

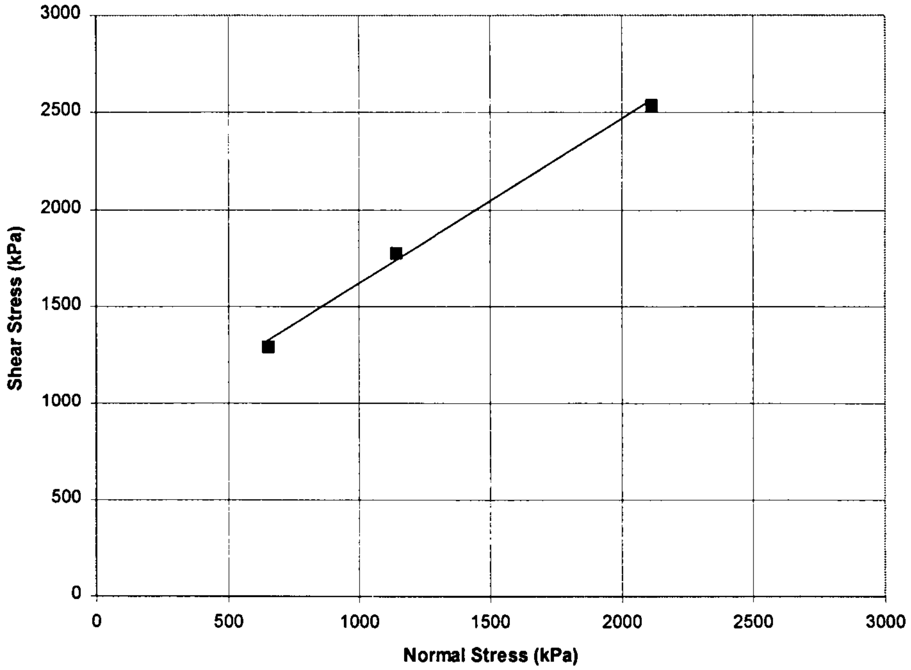

3000
2500
2000
1500
1000
500
0
Shear Stress (kPa)
0
500
1000
1500
2000
2500
3000
Normal Stress (kPa)

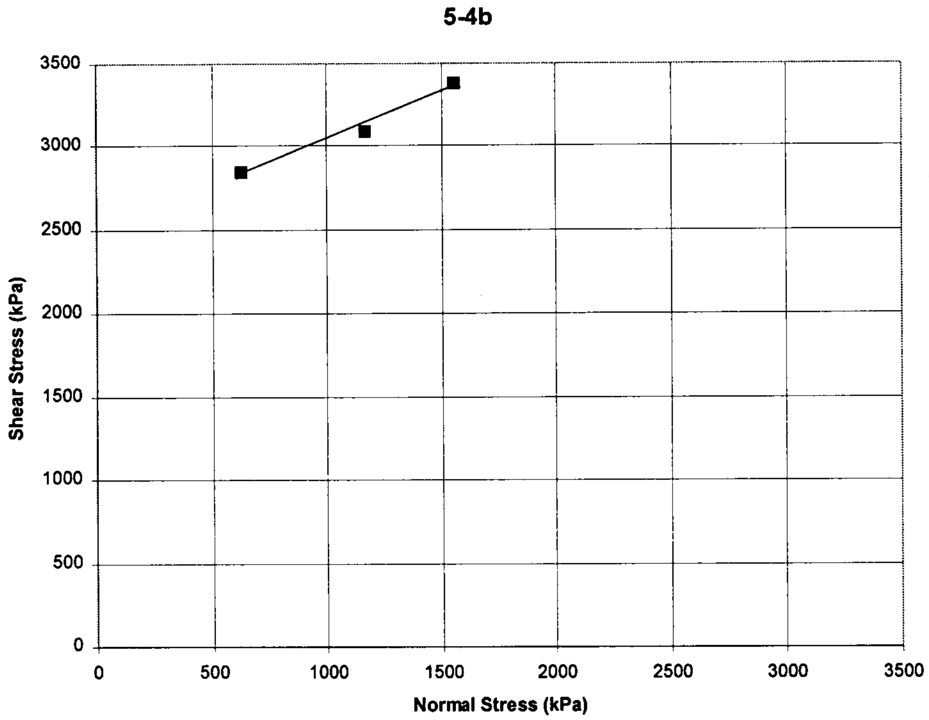
5-4b
Shear Stress (kPa)
3500
3000
2500
2000
1500
1000
500
0
0
500
1000
1500
2000
2500
3000
3500
Normal Stress (kPa)

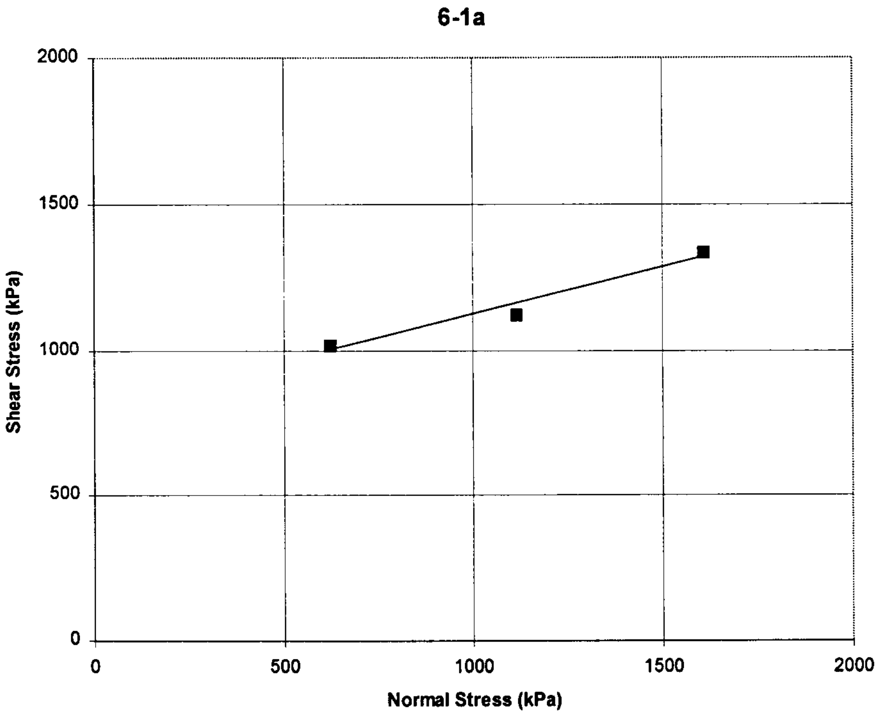
6-1a
Shear Stress (kPa)
2000
1500
1000
500
0
0
500
1000
1500
2000
Normal Stress (kPa)

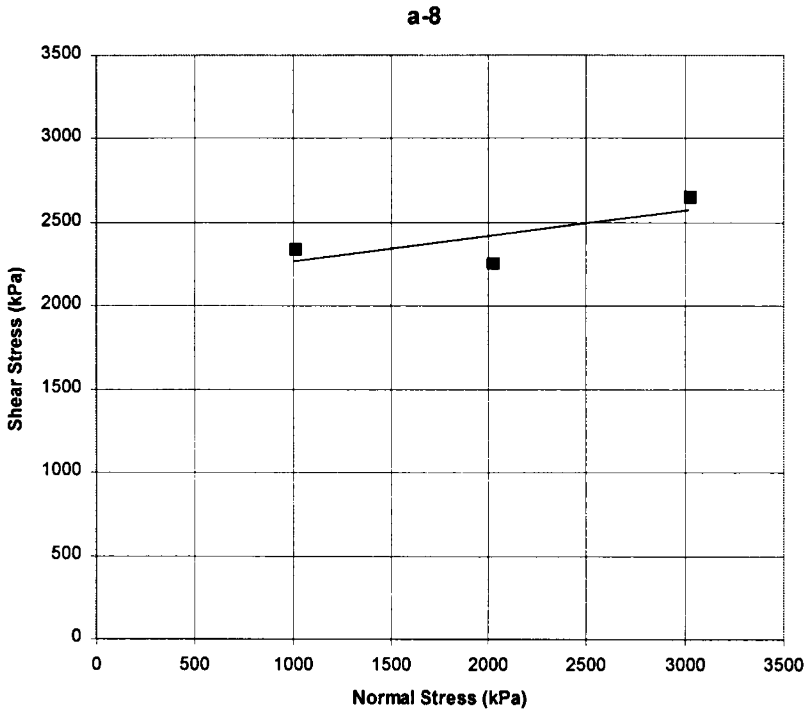
a-8
Shear Stress (kPa)
Normal Stress (kPa)
0
500
1000
1500
2000
2500
3000
3500

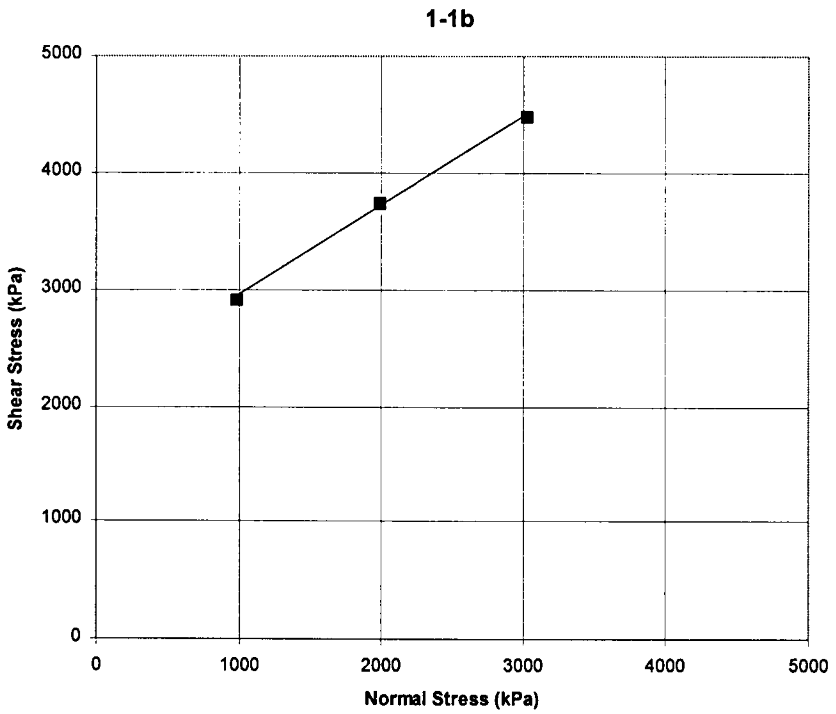
1-1b
Shear Stress (kPa)
Normal Stress (kPa)
0
1000
2000
3000
4000
5000

Direct Shear Test Results		
US19E Samples		
Tested 8/19/96 by MBH		
Sample	Normal Gage Pressure (kPa)	Shear Gage Pressure (kPa)
US-18	950	1625
US-3	1000	2000
US-6	1300	1700
US-12	875	1000
US-15	1000	1600
US-17	1250	2500
US-18	1375	1750
US-3	1500	2250
US-6	1950	2625
US-12	1250	1200
US-15	1500	1750
US-17	1875	2875
US-18	1875	2250
US-3	2050	2850
US-6	2625	3050
US-12	1625	1500
US-15	2000	1875
US-17	2500	3475
US-2	950	1650
US-5	1450	2400
US-10	1000	1350
US-11	1000	2750
US-13	1050	2750
US-20	750	1000
US-2	1375	2175
US-5	2125	3250
US-10	1500	1750
US-11	1500	3175
US-13	1625	5750
US-20	1250	1550
US-2	1875	2500
US-5	2875	3750
US-10	2000	2200
US-11	2050	3675

US-13	2200	4750
US-20	1550	1550
US-7	1000	1650
US-8	875	1350
US-9	1125	1500
US-14	875	1125
US-16	1375	2190
US-19	875	1150
US-7	1550	2400
US-8	1375	1800
US-9	1700	2000
US-14	1375	1550
US-16	2050	2850
US-19	1300	1600
US-7	2050	2700
US-8	1800	2100
US-9	2250	2400
US-14	1750	1750
US-16	2750	3125
US-19	1750	1875
US-4	1125	2000
US-4	1700	2450
US-4	2300	2950
US-1	750	1175
US-1	1125	1550
US-1	1500	1900
USBFA-1	875	900
USBFA-1	1375	1200
USBFA-1	1800	1450
USBFA-2	600	625
USBFA-2	800	700
USBFA-2	1125	950

Sample	Normal Stress (kPa)	Shear Stress (kPa)
US-18	404.86	493.24
US-3	392.33	558.87
US-6	397.25	370.00
US-12	413.81	336.83

US-15	392.64	447.44
US-17	399.45	569.01
US-18	585.61	530.85
US-3	588.50	628.73
US-6	595.88	571.32
US-12	591.15	404.20
US-15	588.95	489.39
US-17	599.17	654.36
US-18	798.56	682.52
US-3	804.28	796.39
US-6	802.15	663.82
US-12	768.50	505.25
US-15	785.27	524.35
US-17	798.90	790.92
US-2	409.68	506.80
US-5	401.87	473.76
US-10	398.66	383.32
US-11	390.82	765.48
US-13	386.71	721.37
US-20	377.23	358.24
US-2	592.97	668.06
US-5	588.95	641.55
US-10	597.99	496.90
US-11	586.23	958.24
US-13	598.48	883.78
US-20	628.72	555.28
US-2	808.59	767.88
US-5	796.82	740.25
US-10	797.32	624.68
US-11	801.18	1022.96
US-13	810.25	2035.12
US-20	779.62	555.28
US-7	390.82	459.29
US-8	383.71	421.66
US-9	393.92	374.09
US-14	392.11	359.07
US-16	401.06	454.96
US-19	402.26	376.55

US-7	605.77	668.06
US-8	602.98	562.21
US-9	595.26	498.79
US-14	616.18	494.72
US-16	597.94	592.07
US-19	597.64	523.89
US-7	801.18	751.56
US-8	789.35	655.91
US-9	787.85	598.55
US-14	784.23	558.56
US-16	802.12	649.20
US-19	804.52	613.94
US-4	392.30	496.73
US-4	592.81	608.49
US-4	802.03	732.68
US-1	392.03	437.44
US-1	588.04	577.05
US-1	784.06	707.35
USBFA-1	388.56	284.66
USBFA-1	610.60	379.55
USBFA-1	799.33	458.62
USBFA-2	431.57	320.19
USBFA-2	575.43	358.61
USBFA-2	809.19	486.69

APPENDIX I

Base Friction Angle Test Data

Direct Shear Test Results - BFA		
Sample 10-1 (3.75) BFA		
Tested 9/3/96 by MBH		
	Diameter = 50mm	
Normal Gage Pressure (KPa)	Shear Gage Pressure (KPa)	Shear Plane Area (m^2)**
1500	875	0.0020172
2000	1000	0.0020172
2500	1150	0.0020172
Normal Stress (kPa)	Shear Stress (KPa)	
1506.54	625.93	
2008.73	715.35	
2510.91	822.65	
	Regression Output:	
Constant	327.867836605	
Std Err of Y Est	7.30099002503	
R Squared	0.997252747253	
No. of Observations	3	
Degrees of Freedom	1	
X Coefficient(s)	0.195866238894	
Std Err of Coef.	0.0102803114319	

Direct Shear Test Results - BFA		
Sample 10-5B BFA		
Tested 9/3/96 by MBH		
	Diameter = 50mm	
Normal Gage Pressure (KPa)	Shear Gage Pressure (KPa)	Shear Plane Area (m^2)**
1500	930	0.0020172
2000	1125	0.0020172
2500	1525	0.0020172
Normal Stress (kPa)	Shear Stress (KPa)	
1506.54	665.27	
2008.72	804.77	
2510.91	1090.91	
	Regression Output:	
Constant	2.38	
Std Err of Y Est	59.87	
R Squared	0.96	
No. of Observations	3.00	
Degrees of Freedom	1.00	
X Coefficient(s)	0.42	
Std Err of Coef.	0.08	

Direct Shear Test Results - BFA		
Sample 10-8A BFA		
Tested 9/3/96 by MBH		
	Diameter = 50mm	
Normal Gage Pressure (KPa)	Shear Gage Pressure (KPa)	Shear Plane Area (m^2)**
1375	950	0.001858
1875	1550	0.001858
2250	1850	0.001858
Normal Stress (kPa)	Shear Stress (KPa)	
1499.33	737.81	
2044.54	1203.79	
2453.44	1436.79	
	Regression Output:	
Constant	-351.587728741	
Std Err of Y Est	54.1696478065	
R Squared	0.988416988417	
No. of Observations	3	
Degrees of Freedom	1	
X Coefficient(s)	0.739190523198	
Std Err of Coef.	0.0800197214158	

Direct Shear Test Results - BFA		
Sample 1-1b BFA		
Tested 1/15/96 by MBH		
	Diameter = 50mm	
Normal Gage Pressure (KPa)	Shear Gage Pressure (KPa)	Shear Plane Area (m^2)**
1450	900	0.00196
1950	1325	0.00196
2375	1700	0.00196
Normal Stress (kPa)	Shear Stress (KPa)	
1498.83	662.60	
2015.66	975.50	
2454.97	1251.58	
	Regression Output:	
Constant	-261.873047688	
Std Err of Y Est	4.46293198606	
R Squared	0.999885315449	
No. of Observations	3	
Degrees of Freedom	1	
X Coefficient(s)	0.615683433153	31.62
Std Err of Coef.	0.00659378575807	

Direct Shear Test Results - BFA		
Sample 1-4A BFA		
Tested 9/2/96 by MBH		
	Diameter = 50.0 mm	
Normal Gage Pressure (KPa)	Shear Gage Pressure (KPa)	Shear Plane Area (m^2)**
1450	1000	0.00196
1950	1450	0.00196
2375	2050	0.00196
Normal Stress (kPa)	Shear Stress (KPa)	
1498.83	736.22	
2015.66	1067.53	
2454.97	1509.26	
	Regression Output:	
Constant	-494.697782174	
Std Err of Y Est	70.5954695976	
R Squared	0.983433141596	
No. of Observations	3	
Degrees of Freedom	1	
X Coefficient(s)	0.803607044284	38.79
Std Err of Coef.	0.104301701991	

Direct Shear Test Results - BFA		
Sample 2-2b (10.5) BFA		
Tested 9/3/96 by MBH		
	Diameter = 50mm	
Normal Gage Pressure (KPa)	Shear Gage Pressure (KPa)	Shear Plane Area (m^2)**
1250	1000	0.00167
1625	1350	0.00167
2050	1625	0.00167
Normal Stress (kPa)	Shear Stress (KPa)	
1516.47	864.07	
1971.41	1166.50	
2487.01	1404.12	
	Regression Output:	
Constant	40.8861049033	
Std Err of Y Est	40.2100451735	
R Squared	0.988965320169	
No. of Observations	3	
Degrees of Freedom	1	
X Coefficient(s)	0.554325305489	
Std Err of Coef.	0.058553659391	

Direct Shear Test Results - BFA		
Sample 2-2b (11.8) BFA		
Tested 9/2/96 by MBH		
	Diameter = 50mm	
Normal Gage Pressure (KPa)	Shear Gage Pressure (KPa)	Shear Plane Area (m^2)**
1450	750	0.00196
1875	1000	0.00196
2375	1250	0.00196
Normal Stress (kPa)	Shear Stress (KPa)	
1498.83	552.17	
1938.14	736.22	
2454.97	920.28	
	Regression Output:	
Constant	-18.24	
Std Err of Y Est	12.17	
R Squared	1.00	
No. of Observations	3.00	
Degrees of Freedom	1.00	
X Coefficient(s)	0.38	
Std Err of Coef.	0.02	

Direct Shear Test Results - BFA		
Sample 3-3A BFA		
Tested 9/2/96 by MBH		
	Diameter = 50mm	
Normal Gage Pressure (KPa)	Shear Gage Pressure (KPa)	Shear Plane Area (m^2)**
1450	1150	0.00196
1875	1575	0.00196
2375	2125	0.00196
Normal Stress (kPa)	Shear Stress (KPa)	
1498.83	846.66	
1938.14	1159.55	
2454.97	1564.48	
	Regression Output:	
Constant	-286.082956506	
Std Err of Y Est	13.7945170478	
R Squared	0.999265417962	
No. of Observations	3	
Degrees of Freedom	1	
X Coefficient(s)	0.751694444524	36.931981
Std Err of Coef.	0.0203807923431	

Direct Shear Test Results - BFA		
Sample 4-4B BFA		
Tested 9/2/96 by MBH		
	Diameter = 50mm	
Normal Gage Pressure (KPa)	Shear Gage Pressure (KPa)	Shear Plane Area (m^2)**
1450	1000	0.00196
1875	1375	0.00196
2375	1850	0.00196
Normal Stress (kPa)	Shear Stress (KPa)	
1498.83	736.22	
1938.14	1012.31	
2454.97	1362.02	
	Regression Output:	
Constant	-249.83	
Std Err of Y Est	9.33	
R Squared	1.00	
No. of Observations	3.00	
Degrees of Freedom	1.00	
X Coefficient(s)	0.66	
Std Err of Coef.	0.01	

Direct Shear Test Results - BFA		
Sample 4-6A BFA		
Tested 9/2/96 by MBH		
	Diameter = 50mm	
Normal Gage Pressure (KPa)	Shear Gage Pressure (KPa)	Shear Plane Area (m^2)**
1450	1175	0.00196
1875	1425	0.00196
2375	1875	0.00196
Normal Stress (kPa)	Shear Stress (KPa)	
1498.83	865.06	
1938.14	1049.12	
2454.97	1380.42	
	Regression Output:	
Constant	33.7883396799	
Std Err of Y Est	43.006435502	
R Squared	0.986441217925	
No. of Observations	3	
Degrees of Freedom	1	
X Coefficient(s)	0.541967541494	
Std Err of Coef.	0.063540117305	

Direct Shear Test Results - BFA		
Sample 5-4b BFA		
Tested 9/3/96 by MBH		
	Diameter = 50mm	
Normal Gage Pressure (KPa)	Shear Gage Pressure (KPa)	Shear Plane Area (m^2)**
1500	1200	0.00196
1875	1625	0.00196
2375	2075	0.00196
Normal Stress (kPa)	Shear Stress (KPa)	
1550.51	883.47	
1938.14	1196.36	
2454.97	1527.67	
	Regression Output:	
Constant	-200.97	
Std Err of Y Est	29.95	
R Squared	1.00	
No. of Observations	3.00	
Degrees of Freedom	1.00	
X Coefficient(s)	0.71	35.31341
Std Err of Coef.	0.05	

Direct Shear Test Results - BFA		
Sample 6-1A BFA		
Tested 9/3/96 by MBH		
	Diameter = 50mm	
Normal Gage Pressure (KPa)	Shear Gage Pressure (KPa)	Shear Plane Area (m^2)**
1500	875	0.00196
1875	1100	0.00196
2375	1300	0.00196
Normal Stress (kPa)	Shear Stress (KPa)	
1550.51	644.20	
1938.14	809.85	
2454.97	957.09	
	Regression Output:	
Constant	124.859693878	
Std Err of Y Est	25.6753075572	
R Squared	0.986548760742	
No. of Observations	3	
Degrees of Freedom	1	
X Coefficient(s)	0.342645607108	
Std Err of Coef.	0.0400098607079	

Direct Shear Test Results - BFA		
Sample 74-A BFA		
Tested 9/3/96 by MBH		
	Diameter = 50mm	
Normal Gage Pressure (KPa)	Shear Gage Pressure (KPa)	Shear Plane Area (m^2)**
1500	1375	0.00196
1875	1625	0.00196
2375	2050	0.00196
Normal Stress (kPa)	Shear Stress (KPa)	
1550.51	1012.31	
1938.14	1196.36	
2454.97	1509.26	
	Regression Output:	
Constant	144.76	
Std Err of Y Est	23.54	
R Squared	1.00	
No. of Observations	3.00	
Degrees of Freedom	1.00	
X Coefficient(s)	0.55	28.92
Std Err of Coef.	0.04	

Direct Shear Test Results - BFA		
Sample A-8 3.0 BFA		
Tested 9/2/96 by MBH		
	Diameter = 47.4 mm	
Normal Gage Pressure (KPa)	Shear Gage Pressure (KPa)	Shear Plane Area (m^2)**
875	650	0.0017654
1300	900	0.0017654
1750	1325	0.0017654
Normal Stress (kPa)	Shear Stress (KPa)	
1004.16	531.30	
1491.90	735.64	
2008.33	1083.03	
2438.68	1226.07	
	Regression Output:	
Constant	-43.4593654497	
Std Err of Y Est	51.9537573823	
R Squared	0.982654495339	
No. of Observations	3	
Degrees of Freedom	1	
X Coefficient(s)	0.550649768462	
Std Err of Coef.	0.073159125968	28.839369

US19E Base Friction Angle Tests

USBFA-1	388.56	284.66
USBFA-1	610.60	379.55
USBFA-1	799.33	458.62
USBFA-2	431.57	320.19
USBFA-2	575.43	358.61
USBFA-2	809.19	486.69

APPENDIX J

Point Load Test Data

Point Load Test						
Sample 10-1 (3.75)						
slate						
Tested 4/17/96						
Diametral Tests						
L (mm)	L/2 (mm)	D (mm)	Gage(kPa)	Load (kN)	De (mm)	Is 50
50	25	50	3632.4	2.7	50	1.08
50	25	50	2098.7	1.6	50	0.62
50	25	50	2287.0	1.7	50	0.68
50	25	50	3228.8	2.4	50	0.96
50	25	50	2556.1	1.9	50	0.76
50	25	50	3632.4	2.7	50	1.08
					Is 50	0.9

Point Load Test						
Sample 10-5b(3.00)						
Slate						
Tested 4/17/96						
Diametral Tests						
L (mm)	L/2 (mm)	D (mm)	Gage(kPa)	Load (kN)	De (mm)	Is 50
50	25	50	2421.6	1.8	50	0.72
50	25	50	2287.0	1.7	50	0.68
50	25	50	3094.2	2.3	50	0.92
50	25	50	3228.8	2.4	50	0.96
50	25	50	3094.2	2.3	50	0.92
50	25	50	2287.0	1.7	50	0.68
50	25	50	2825.2	2.1	50	0.84
50	25	50	2421.6	1.8	50	0.72
50	25	50	3363.3	2.5	50	1.00
50	25	50	3228.8	2.4	50	0.96
50	25	50	2152.5	1.6	50	0.64
					Is 50	0.8

Point Load Test						
Sample 10-8a						
Slate						
Tested 4/17/96						
Diametral Tests						
L (mm)	L/2 (mm)	D (mm)	Gage(kPa)	Load (kN)	De (mm)	Is 50
50	25	50	941.7	0.7	50	0.28
50	25	50	1614.4	1.2	50	0.48
50	25	50	941.7	0.7	50	0.28
50	25	50	1748.9	1.3	50	0.52
50	25	50	1345.3	1.0	50	0.40
50	25	50	1210.8	0.9	50	0.36
50	25	50	1479.8	1.1	50	0.44
50	25	50	941.7	0.7	50	0.28
50	25	50	1479.8	1.1	50	0.44
50	25	50	1210.8	0.9	50	0.36
					Is 50	0.3

Point Load Test						
Sample 1-1B*2						
Sandstone						
Tested 7/12/96						
Diametral Tests						
L (mm)	L/2 (mm)	D (mm)	Gage(kPa)	Load (kN)	De (mm)	Is 50
50	25	50	11031.6	8.2	50	3.3
50	25	50	11166.1	8.3	50	3.3
50	25	50	11166.1	8.3	50	3.3
50	25	50	10224.4	7.6	50	3.0
50	25	50	10762.5	8.0	50	3.2
50	25	50	10089.9	7.5	50	3.0
50	25	50	10089.9	7.5	50	3.0
50	25	50	10493.5	7.8	50	3.1
50	25	50	10628.0	7.9	50	3.2
50	25	50	9820.8	7.3	50	2.9
50	25	50	10493.5	7.8	50	3.1
					Is 50	3.1

Point Load Test						
Sample 1-4A						
Metasandstone						
Tested 4/17/96						
Diametral Tests						
L (mm)	L/2 (mm)	D (mm)	Gage(kPa)	Load (kN)	De (mm)	Is 50
50	25	50	4305.0	3.2	50	1.28
50	25	50	4439.5	3.3	50	1.32
50	25	50	4708.6	3.5	50	1.40
50	25	50	3766.9	2.8	50	1.12
50	25	50	4305.0	3.2	50	1.28
50	25	50	3901.4	2.9	50	1.16
50	25	50	2825.2	2.1	50	0.84
50	25	50	4439.5	3.3	50	1.32
50	25	50	3766.9	2.8	50	1.12
50	25	50	4439.5	3.3	50	1.32
50	25	50	3901.4	2.9	50	1.16
					Is 50	1.3

Point Load Test						
Sample 2-2B (10.53 - 10.80)						
Metasandstone						
Tested 4/17/96						
Diametral Tests						
L (mm)	L/2 (mm)	D (mm)	Gage(kPa)	Load (kN)	De (mm)	Is 50
50	25	50	2018.0	1.5	50	0.60
50	25	50	1748.9	1.3	50	0.52
50	25	50	2825.2	2.1	50	0.84
50	25	50	1883.4	1.4	50	0.56
50	25	50	1479.8	1.1	50	0.44
50	25	50	3094.2	2.3	50	0.92
50	25	50	1210.8	0.9	50	0.36
50	25	50	2959.7	2.2	50	0.88
50	25	50	1614.4	1.2	50	0.48
50	25	50	2018.0	1.5	50	0.60
					Is 50	0.6

Point Load Test						
Sample 2-2B (11.8)						
Tested 9/3/96						
Diametral Tests						
L (mm)	L/2 (mm)	D (mm)	Gage(kPa)	Load (kN)	De (mm)	Is 50
50	25	50	9417.2	7	50	2.80
50	25	50	9148.2	6.8	50	2.72
50	25	50	10089.9	7.5	50	3.00
50	25	50	11031.6	8.2	50	3.28
50	25	50	9282.7	6.9	50	2.76
50	25	50	9686.3	7.2	50	2.88
50	25	50	9955.3	7.4	50	2.96
50	25	50	10897.1	8.1	50	3.24
					Is 50	3.0

Point Load Test						
Sample 3-3A						
Cong						
Tested 9/3/96						
Diametral Tests						
L (mm)	L/2 (mm)	D (mm)	Gage(kPa)	Load (kN)	De (mm)	Is 50
50	25	50	1076.3	0.8	50	0.32
50	25	50	1614.4	1.2	50	0.48
50	25	50	2959.7	2.2	50	0.88
50	25	50	538.1	0.4	50	0.16
50	25	50	1210.8	0.9	50	0.36
50	25	50	1614.4	1.2	50	0.48
50	25	50	1479.8	1.1	50	0.44
50	25	50	941.7	0.7	50	0.28
50	25	50	1748.9	1.3	50	0.52
50	25	50	1076.3	0.8	50	0.32
50	25	50	1210.8	0.9	50	0.36
50	25	50	1614.4	1.2	50	0.48
					Is 50	0.4

Point Load Test						
Sample 4-4b Cong.						
Tested 9/3/96						
L (mm)	L/2 (mm)	D (mm)	Gage(kPa)	Load (kN)	De (mm)	Is 50
50	25	50	3094.2	2.3	50	0.92
50	25	50	3363.2	2.5	50	1.00
50	25	50	4304.9	3.2	50	1.28
50	25	50	2825.1	2.1	50	0.84
50	25	50	2959.6	2.2	50	0.88
50	25	50	4170.4	3.1	50	1.24
50	25	50	3363.2	2.5	50	1.00
50	25	50	2959.6	2.2	50	0.88
50	25	50	4304.9	3.2	50	1.28
50	25	50	3363.2	2.5	50	1.00
					Is 50	1.0

Point Load Test						
Sample 4-6a						
Sandstone W/little weathering of the matrix and no observable anisotropy						
Tested 4/4/96						
L (mm)	L/2 (mm)	D (mm)	Gage(kPa)	Load (kN)	De (mm)	Is 50
50	25	50	3094.2	2.3	50	0.92
50	25	50	3497.8	2.6	50	1.04
50	25	50	3363.3	2.5	50	1.00
50	25	50	3766.9	2.8	50	1.12
50	25	50	4708.6	3.5	50	1.40
50	25	50	2959.7	2.2	50	0.88
50	25	50	4843.1	3.6	50	1.44
50	25	50	2287.0	1.7	50	0.68
50	25	50	4843.1	3.6	50	1.44
50	25	50	3497.8	2.6	50	1.04
50	25	50	3766.9	2.8	50	1.12
50	25	50	4843.1	3.6	50	1.44
50	25	50	4843.1	3.6	50	1.44
50	25	50	4574.1	3.4	50	1.36
50	25	50	3901.4	2.9	50	1.16
50	25	50	4843.1	3.6	50	1.44
					Is 50	1.2

Point Load Test						
Sample 5-4B						
Sandstone						
Tested 9/3/96						
Diametral Tests						
L (mm)	L/2 (mm)	D (mm)	Gage(kPa)	Load (kN)	De (mm)	Is 50
50	25	50	3372.3	2.5	50	1.00
50	25	50	4721.2	3.5	50	1.40
50	25	50	3642.1	2.7	50	1.08
50	25	50	4316.6	3.2	50	1.28
50	25	50	5395.7	4	50	1.60
50	25	50	4316.6	3.2	50	1.28
50	25	50	3237.4	2.4	50	0.96
50	25	50	3102.5	2.3	50	0.92
50	25	50	3372.3	2.5	50	1.00
					Is 50	1.2

Point Load Test						
Sample 6-1A						
Sstone						
Tested 9/3/96						
Diametral Tests						
L (mm)	L/2 (mm)	D (mm)	Gage(kPa)	Load (kN)	De (mm)	Is 50
50	25	50	5246.737942	3.9	50	1.56
50	25	50	7802.841041	5.8	50	2.32
50	25	50	5650.333168	4.2	50	1.68
50	25	50	5784.86491	4.3	50	1.72
50	25	50	3766.888779	2.8	50	1.12
50	25	50	5246.737942	3.9	50	1.56
					Is 50	1.7

Point Load Test						
Sample 7-4A						
Sstone						
Tested 9/3/96						
Diametral Tests						
L (mm)	L/2 (mm)	D (mm)	Gage(kPa)	Load (kN)	De (mm)	Is 50
50	25	50	1210.8	0.9	50	0.36
50	25	50	1076.3	0.8	50	0.32
50	25	50	1479.8	1.1	50	0.44
50	25	50	941.7	0.7	50	0.28
50	25	50	1748.9	1.3	50	0.52
50	25	50	1883.4	1.4	50	0.56
50	25	50	1479.8	1.1	50	0.44
50	25	50	1614.4	1.2	50	0.48
					Is 50	0.425

Point Load Test						
Sample A-8 (3.00)						
Metasandstone						
Tested 4/17/96						
Diametral Tests						
L (mm)	L/2 (mm)	D (mm)	Gage(kPa)	Load (kN)	De (mm)	Is 50
50	25	50	6995.7	5.2	50	2.08
50	25	50	7264.7	5.4	50	2.16
50	25	50	8071.9	6.0	50	2.40
50	25	50	7802.8	5.8	50	2.32
50	25	50	7802.8	5.8	50	2.32
50	25	50	7802.8	5.8	50	2.32
50	25	50	7130.2	5.3	50	2.12
50	25	50	7668.3	5.7	50	2.28
50	25	50	7533.8	5.6	50	2.24
50	25	50	6861.1	5.1	50	2.04
50	25	50	6726.6	5.0	50	2.00
					Is 50	2.2

US19E Point Load Data

Point Load Tests											
US 19E Sevier Shale											
Tested: 8/26/96 MBH											
Test	Type	W (mm)	D (mm)	L (mm)	Gage (kPa)	P (kN)	De (mm^2)	De	Is (un)	F	IS50
1.0	lump para	33.7	29.2	38.4	600.0	0.7	1253.6	35.4	0.5	0.9	0.5
2.0	lump para	22.2	18.4	37.8	500.0	0.6	520.4	22.8	1.1	0.7	0.8
3.0	lump para	24.2	20.8	50.6	1150.0	1.3	641.2	25.3	2.0	0.7	1.5
4.0	lump para	22.0	19.5	33.6	600.0	0.7	546.5	23.4	1.2	0.7	0.9
5.0	lump para	37.5	28.9	50.0	1125.0	1.3	1380.6	37.2	0.9	0.9	0.8
6.0	lump para	25.0	21.4	67.6	920.0	1.0	681.5	26.1	1.5	0.7	1.1
7.0	lump para	31.4	25.2	63.7	1300.0	1.5	1008.0	31.7	1.5	0.8	1.2
8.0	lump para	36.3	27.8	63.7	1500.0	1.7	1285.5	35.9	1.3	0.9	1.1
9.0	lump para	24.2	26.4	58.1	800.0	0.9	813.9	28.5	1.1	0.8	0.9
10.0	lump para	25.9	21.8	73.9	750.0	0.9	719.3	26.8	1.2	0.8	0.9
11.0	lump para	27.3	20.0	73.6	1200.0	1.4	695.5	26.4	2.0	0.7	1.5
12.0	lump para	27.3	19.9	68.7	1050.0	1.2	692.1	26.3	1.7	0.7	1.3
13.0	lump para	24.8	24.3	70.8	1350.0	1.5	767.7	27.7	2.0	0.8	1.5
14.0	lump para	27.9	19.8	73.7	1200.0	1.4	703.7	26.5	1.9	0.8	1.5
15.0	lump para	26.8	17.3	68.7	1350.0	1.5	590.6	24.3	2.6	0.7	1.9
16.0	lump para	29.6	23.8	57.2	800.0	0.9	897.4	30.0	1.0	0.8	0.8
17.0	lump para	30.2	24.4	56.7	1150.0	1.3	938.7	30.6	1.4	0.8	1.1
18.0	lump para	31.2	21.9	58.3	1150.0	1.3	871.3	29.5	1.5	0.8	1.2
19.0	lump para	30.7	17.5	58.6	850.0	1.0	684.4	26.2	1.4	0.7	1.1
20.0	lump para	20.2	16.4	59.3	1300.0	1.5	422.0	20.5	3.5	0.7	2.3
21.0	lump para	21.4	21.5	67.5	500.0	0.6	586.1	24.2	1.0	0.7	0.7
22.0	lump para	21.2	15.6	58.9	900.0	1.0	421.3	20.5	2.4	0.7	1.6
23.0	lump para	20.0	13.3	60.1	1050.0	1.2	338.9	18.4	3.5	0.6	2.2
24.0	lump para	22.5	25.3	68.6	1575.0	1.8	725.2	26.9	2.5	0.8	1.9
25.0	lump para	23.2	24.0	55.5	750.0	0.9	709.3	26.6	1.2	0.8	0.9
26.0	lump para	21.7	20.1	50.1	1350.0	1.5	555.6	23.6	2.8	0.7	2.0
27.0	lump para	22.4	20.2		2000.0	2.3	576.4	24.0	3.9	0.7	2.8
28.0	lump para	23.1	24.2	58.7	2950.0	3.3	712.1	26.7	4.7	0.8	3.5
29.0	lump para	21.6	19.0	60.3	700.0	0.8	522.8	22.9	1.5	0.7	1.1
30.0	lump para	21.4	27.0	59.2	1700.0	1.9	736.1	27.1	2.6	0.8	2.0
31.0	lump para	21.6	17.0	63.9	1350.0	1.5	467.8	21.6	3.3	0.7	2.2

32.0	lump para	21.2	19.3	64.0	1350.0	1.5	521.2	22.8	2.9	0.7	2.1
33.0	lump para	22.0	21.8	59.4	1400.0	1.6	611.0	24.7	2.6	0.7	1.9
34.0	lump para	22.6	20.0	55.6	1000.0	1.1	575.8	24.0	2.0	0.7	1.4
35.0	lump para	28.4	18.9	59.1	1000.0	1.1	683.8	26.1	1.7	0.7	1.2
36.0	lump para	16.3	18.1	57.4	650.0	0.7	375.8	19.4	2.0	0.7	1.3
37.0	lump para	33.2	28.5	35.3	1000.0	1.1	1205.4	34.7	0.9	0.8	0.8
38.0	lump para	29.2	20.4	46.5	1150.0	1.3	758.8	27.5	1.7	0.8	1.3
39.0	lump para	34.9	27.0	63.5	1250.0	1.4	1200.4	34.6	1.2	0.8	1.0
40.0	lump para	24.4	19.5	50.3	650.0	0.7	606.1	24.6	1.2	0.7	0.9
41.0	lump para	31.7	28.4	42.2	2000.0	2.3	1146.9	33.9	2.0	0.8	1.7
42.0	lump para	28.3	16.0	66.4	650.0	0.7	576.8	24.0	1.3	0.7	0.9
43.0	lump para	33.0	31.0	55.1	1900.0	2.2	1303.2	36.1	1.7	0.9	1.4
44.0	lump para	22.7	25.0	54.0	1300.0	1.5	722.9	26.9	2.0	0.8	1.5
45.0	lump para	22.0	22.0	54.5	1850.0	2.1	616.6	24.8	3.4	0.7	2.5
46.0	lump para	21.6	16.4	33.6	450.0	0.5	451.3	21.2	1.1	0.7	0.8
47.0	lump para	26.9	27.2	57.3	1050.0	1.2	932.1	30.5	1.3	0.8	1.0
48.0	lump para	23.3	21.4	54.2	1350.0	1.5	635.2	25.2	2.4	0.7	1.8
49.0	lump para	29.4	27.9	29.8	1050.0	1.2	1044.9	32.3	1.1	0.8	0.9
50.0	lump para	31.6	27.6	44.9	1150.0	1.3	1111.0	33.3	1.2	0.8	1.0
51.0	lump para	33.7	22.6	47.9	1250.0	1.4	970.2	31.1	1.5	0.8	1.2
52.0	lump para	33.0	23.0	61.0	1950.0	2.2	966.9	31.1	2.3	0.8	1.8
53.0	lump para	21.2	19.8	76.5	1800.0	2.0	534.7	23.1	3.8	0.7	2.7
54.0	lump para	32.4	29.7	58.8	1400.0	1.6	1225.8	35.0	1.3	0.9	1.1
55.0	lump para	18.6	18.2	66.5	1000.0	1.1	431.2	20.8	2.6	0.7	1.8
56.0	lump para	20.8	19.7	83.4	1450.0	1.6	522.0	22.8	3.2	0.7	2.2
57.0	lump para	24.3	23.3	56.8	950.0	1.1	721.3	26.9	1.5	0.8	1.1
58.0	lump para	18.9	21.1	56.7	800.0	0.9	508.0	22.5	1.8	0.7	1.2
59.0	lump para	22.3	24.0	58.7	700.0	0.8	681.8	26.1	1.2	0.7	0.9
60.0	lump para	20.4	19.3	59.8	1050.0	1.2	501.6	22.4	2.4	0.7	1.7
61.0	lump para	35.0	31.0	56.7	1700.0	1.9	1382.2	37.2	1.4	0.9	1.2
62.0	lump para	18.5	22.5	85.8	700.0	0.8	530.3	23.0	1.5	0.7	1.1
63.0	lump para	20.3	30.2	84.2	2600.0	3.0	781.0	27.9	3.8	0.8	2.9
64.0	lump para	24.8	24.7	80.1	800.0	0.9	780.3	27.9	1.2	0.8	0.9
65.0	lump para	29.8	25.1	85.8	1550.0	1.8	952.8	30.9	1.8	0.8	1.5
66.0	lump para	35.0	21.7	55.8	1200.0	1.4	967.5	31.1	1.4	0.8	1.1
67.0	lump para	23.9	16.0	28.0	550.0	0.6	487.1	22.1	1.3	0.7	0.9
68.0	lump para	26.1	16.0	66.8	600.0	0.7	532.0	23.1	1.3	0.7	0.9
69.0	lump para	21.7	17.6	35.6	750.0	0.9	486.5	22.1	1.7	0.7	1.2

70.0	lump para	24.0	25.4	50.3	1150.0	1.3	776.6	27.9	1.7	0.8	1.3
71.0	lump para	36.4	37.2	57.2	1550.0	1.8	1724.9	41.5	1.0	0.9	0.9
72.0	lump para	42.0	43.9	65.6	2000.0	2.3	2348.8	48.5	1.0	1.0	1.0
73.0	lump para	30.0	22.9	46.5	550.0	0.6	875.2	29.6	0.7	0.8	0.6
74.0	lump para	30.5	24.1	47.2	1150.0	1.3	936.4	30.6	1.4	0.8	1.1
75.0	lump para	26.6	18.4	66.5	800.0	0.9	623.5	25.0	1.5	0.7	1.1
76.0	lump para	16.5	15.6	75.7	1200.0	1.4	327.9	18.1	4.2	0.6	2.6
77.0	lump para	17.5	17.6	79.5	700.0	0.8	392.4	19.8	2.0	0.7	1.3
78.0	lump para	23.1	21.8	71.3	1850.0	2.1	641.5	25.3	3.3	0.7	2.4
79.0	lump para	25.2	24.9	59.2	1150.0	1.3	799.3	28.3	1.6	0.8	1.3
80.0	lump para	17.4	17.7	77.6	1350.0	1.5	392.3	19.8	3.9	0.7	2.6
81.0	lump para	27.3	21.1	58.4	1100.0	1.2	733.8	27.1	1.7	0.8	1.3
82.0	lump para	21.7	15.8	65.0	650.0	0.7	436.8	20.9	1.7	0.7	1.1
83.0	lump para	17.2	18.0	65.6	550.0	0.6	394.4	19.9	1.6	0.7	1.0
84.0	lump para	17.3	18.3	66.0	950.0	1.1	403.3	20.1	2.7	0.7	1.8
85.0	lump para	24.4	26.1	60.5	1500.0	1.7	811.3	28.5	2.1	0.8	1.6
86.0	lump para	23.2	17.9	65.2	600.0	0.7	529.0	23.0	1.3	0.7	0.9
87.0	lump para	26.3	21.5	73.2	850.0	1.0	720.3	26.8	1.3	0.8	1.0
88.0	lump para	17.5	14.0	71.4	750.0	0.9	312.1	17.7	2.7	0.6	1.7
89.0	lump para	25.0	23.4	72.6	1750.0	2.0	745.2	27.3	2.7	0.8	2.0
90.0	lump para	23.9	16.7	72.4	1650.0	1.9	508.4	22.5	3.7	0.7	2.6
91.0	lump para	18.5	16.0	80.2	550.0	0.6	377.1	19.4	1.7	0.7	1.1
										Is 50	1.4

VITA

Matt Haston was raised in Warren County, Tennessee where he attended both public and private schools. He entered the University of Tennessee at Knoxville in August 1990 and received his Bachelors degree in Civil Engineering in 1994. He then entered graduate school at the University of Tennessee, Knoxville and served as a Graduate Teaching Assistant in the Department of Civil and Environmental Engineering. He was awarded his Master of Science degree for this project in December 1996.